POLITECNICO
MILANO 1863

SCUOLA DI INGEGNERIA INDUSTRIALE
E DELL'INFORMAZIONE

Active Control Design of ESA's 6DoF Micro Vibrations Measurement System

Tesi di Laurea Magistrale in
Space Engineering - Ingegneria Spaziale

Author: **Marina Berto**

Student ID: 944840
Advisor: Prof. Lorenzo Dozio
Co-advisor: Dr. Pietro Nali
Academic Year: 2020-21

Abstract

The present work has the objective of performing some preliminary assessments useful for designing the future control system of ESA's MVMS (Micro Vibrations Measurement System) when operating either in the actuator mode or in the sensor mode.
Firstly, the structural characteristics of the MVMS, the position of the sensors and of the actuators, the normal modes of the facility and the balancing masses arrangement are investigated. Afterwards, it is considered that, since the full FEM model has several Degrees of Freedom (DoFs), it is possible to reduce them thanks to the Craig-Bampton (CB) method. In order to obtain a simpler model of the facility, this latest system is further condensed to fewer physical and modal DoFs. Then, an equivalent model is designed, which accurately describes the behaviour of the MVMS in the longitudinal direction. In order to impose an excitation from the ground, the Large Mass (LM) method is applied both to the equivalent model and to the condensed CB one. Hence, the equivalent system gains one DoF. Eventually, all the models are validated to prove that they are compliant with the full FEM model.
At this point, the control systems are designed on the equivalent model: first the one of the vibration isolation platform (VIBISIO), and then the one of the vibration measurement platform (MPLAT). Regarding the VIBISIO control, it is designed the control system by previously analysing different approaches already employed in literature for controlling Stewart platforms. The most suitable control technique consists of the combination of a feedback (FB) and a feedforward (FF) control, where a skyhook damper with tunable gain is employed in the FB. For the MPLAT control, instead, the H-infinity control strategy is adopted. Subsequently, the controls of the 2DoF model are extended to the condensed CB model. The results confirm that, since all the models had been validated, a control system which is applicable to the 2DoF model is suitable also for the CB system and, eventually, for the full FEM model.

Keywords: micro vibrations measurement platform, Craig-Bampton method, sky-hook damper, H-infinity control

Abstract in lingua italiana

Il presente elaborato ha l'obiettivo di eseguire delle valutazioni preliminari utili per progettare il futuro sistema di controllo dell'MVMS (Sistema di Misura delle Micro Vibrazioni) di ESA quando opera in modalità attuatore oppure in modalità sensore.
In primo luogo, sono investigate le caratteristiche strutturali della piattaforma, la posizione dei sensori e degli attuatori, i modi propri di vibrare della facility e la disposizione delle masse di bilanciamento. Successivamente viene considerato che, siccome il sistema FEM completo possiede parecchi gradi di libertà (gdl), è possibile ridurli grazie al metodo di Craig-Bampton (CB). Per ottenere un modello più semplice della facility, quest'ultimo sistema viene ulteriormente condensato a un numero minore di gdl modali e fisici. In seguito, viene progettato un modello equivalente, il quale descrive accuratamente il comportamento dell'MVMS in direzione longitudinale. Per imporre un'eccitazione dal terreno, viene applicato il metodo della Large Mass (LM) sia al modello equivalente sia al modello Craig-Bampton condensato. Quindi, il sistema equivalente guadagna un gdl. Infine, tutti i modelli vengono validati per dimostrare che sono conformi al modello FEM completo.
A questo punto, vengono progettati i sistemi di controllo sul modello equivalente: prima quello della piattaforma di isolamento delle vibrazioni (VIBISIO), poi quello della piattaforma di misura delle vibrazioni (MPLAT). Riguardo al controllo della VIBISIO, viene progettato il sistema di controllo analizzando prima diversi approcci già impiegati in letteratura per controllare le Stewart platform. La tecnica di controllo più adatta consiste nella combinazione di un controllo in feedback (FB) e di uno in feedforward (FF), dove nel FB viene impiegato uno skyhook damper con guadagno regolabile. Per il controllo della MPLAT, invece, viene adottata la strategia di controllo H-infinito. Successivamente, i controlli del modello a 2 gdl vengono estesi al modello CB condensato. I risultati confermano che, siccome tutti i modelli erano stati validati, un sistema di controllo che è applicabile al modello a 2 gdl risulta idoneo anche per il sistema CB ed, infine, per il modello FEM completo.

Parole chiave: piattaforma di misura delle micro vibrazioni, metodo di Craig-Bampton, sky-hook damper, controllore H-infinito

Contents

Introduction

0.1. Motivation of the Work

This thesis has the aim of performing some preliminary assessments useful for designing the active control system of the MVMS. The focus is made on the actuator mode of the facility, which consists of isolating the Item Under Test (IUT) from vibrations imposed from the ground, and on the sensor mode, which consists of measuring the vibrations imposed by the IUT.
On the MVMS, the isolation from vibrations is both passive and active. The **passive** isolation is performed by two Minus-K, which are made of 6 very soft springs with the task of damping vibrations in the 6 DoFs. Such an isolation acts at high frequencies, guaranteeing a different roll-off rate depending on the damping. The drawback of employing only the passive isolation would be the fact that the resonance peaks would not be attenuated. To obtain this result, it is required to add an **active** isolation, performed by the actuators. Different control strategies have been investigated.
For the VIBISIO control, firstly it has been implemented the FB control under the form of a sky-hook damper, from which it results that the peaks are attenuated. Then, the FB control has been enriched with the FF in order to improve the results: a better attenuation of the peaks is obtained and the high-frequency roll-off gets steeper. On the other hand, for the MPLAT control, the H-infinity control has been adopted to minimize the MPLAT displacement.

0.2. Literature Review

Some articles have been analysed to study whether in the past some research on an active control system of a multi-DoF platform was carried out. It results that the most similar facility to the one of interest is the Stewart platform, which is a facility consisting of two rigid bodies (the base and the platform) connected through six extensible legs. [11] The MVMS presents two Minus-K, providing a passive control, and 12 voice-coil actuators, responsible for the active control.

Concerning the **control of the VIBISIO**, the concepts and the effects of passive and active isolation are explained in the article by Preumont et al. [28]:

- **Passive isolation** generally consists of one or several stages of mass–spring–damper systems introduced in the propagation path, whose parameters are adjusted to achieve the desired corner frequency and a reasonable compromise between the amplification at resonance and the high-frequency attenuation. Passive damping is necessary to limit the amplification at resonance, but it tends to reduce the high-frequency attenuation of the isolation system.
- **Active isolation** has been introduced to resolve this conflict, allowing to achieve simultaneously a low amplification at resonance and a large attenuation at high frequency.

In the present application, the active control provides isolation, not damping. The concepts of active isolation and damping are described in the PhD thesis by Ahmed Abu Hanieh [17]. It provides an insight into several single-axis isolation techniques: a comparison between the sky-hook damper, integral force FB, inertial velocity FB and Lag-Lead control techniques is conducted using some practical examples.

It is made a distinction between **active isolation** and **active damping**:

Table 1: Active isolation vs. active damping [17]

Control type	Purpose	Structure	Control techniques
Active isolation	Active vibration isolation of sensitive payloads in space applications.	Soft six-axis hexapod designed according to the cubic configuration. It consists of two triangular parallel plates connected to each other by six active legs orthogonal to each other.	Two techniques based on force FB are applied in a decentralized manner: • Integral force FB; • Lag-Lead compensator.
Active damping	Addressed to space applications, where it aims at controlling the vibrations of space structures while connecting them rigidly.	Rigid hexapod consisting of two parallel plates connected to each other by six active legs configured according to the cubic architecture.	Decentralized integral force FB.

For the MVMS, **active isolation** can be considered since it is desired to isolate from vibrations a sensitive payload, especially in the case in which the facility is operated in actuator mode. From table 3.2 it can be highlighted that active isolation is provided by **soft** Stewart platforms, which have the following characteristics:

- They can be used efficiently for vibration isolation purposes.
- The corner frequency of the soft hexapod should be as low as possible and the modal spread should be minimized.
- The design of the flexible joints has a great effect on the control authority and the isolation performance.
- The lateral dynamics of the legs deteriorate the high frequency isolation performance of the isolator.

An equivalent model of the soft isolator with acceleration FB is the **sky-hook damper**. It is based on using a simple integration of the measured force signals and feeding the signal back to the voice coil actuator. A high pass filter can be added at low frequency to avoid the low frequency signals from propagating into the system and to prevent the integration of the static component coming from the offset of the electronics. By recalling the article by Preumont et al. [28], the sky-hook damper is a single-axis interface which, if inserted between two rigid bodies, provides a $-40\ dB/decade$ attenuation rate at high frequency and a controllable overshoot at resonance. When inserted between rigid bodies, the sky-hook damper may be implemented with acceleration (or velocity) FB, or equivalently with force FB. However, when inserted between two flexible structures it turns out that the force FB implementation enjoys guaranteed stability properties that acceleration FB lacks.

To fully isolate two rigid bodies with respect to each other, six judiciously placed single-axis isolators are needed. They can be controlled in a centralized or decentralized manner. Here the **decentralized** FB control approach is considered since it has attractive robustness properties and is shown to produce impressive performance. By referring to the PhD thesis by Ahmed Abu Hanieh [17], the decentralized integral force FB succeeds in removing the overshoots at low frequency while having guaranteed stability. Indeed, it is vital to guarantee stability since, when the payload is flexible, the behaviour of the acceleration and force FB are no longer the same. The integral force FB proved to be more efficient than the Lag-Lead controller especially at high frequency where it could even contribute at damping the local modes. The integral force FB technique proved better than the Lag-Lead compensator in terms of damping of the low frequency modes, and even the high frequency lateral modes are influenced and reduced, even though this does not change the fact that the high frequency lateral modes are still problematic.

In the article by Jie Tang et al. [32], the decentralized control theory is employed to design the controller for the linearized system. The results indicate that the platform with the proposed controller is efficient between 5 and 100 Hz, with a great attenuation at the resonance peaks in both longitudinal and lateral direction.

If the disturbance can be measured somewhere along its propagation path, the addition of a **feedforward control** can be considered. In the article by Z. Zhou et al. [35], it is stated that the skyhook FB control can only attenuate vibration near the resonant frequency. To enhance control performance of an isolation system, a FF compensation control strategy is required. In the article by M. Yasuda et al. [34], it is reported that the FF control works very well to improve the response to the direct disturbances, also from the floor, and hence to decrease the transient response. The online page *Feed forwards augment PID control* [1] states that in closed-loop motion control applications, it is com-

mon to multiply the target speed and target acceleration by the velocity and acceleration feed forwards to generate the feed forward's contribution to the control output. In this way, the FF control assumes the form of a PID algorithm. One particular consideration is described both in the article by C. Qingsong et al. [29] and in the article by M. A. Beijen [7]. Both these documents state that FF, differently from FB, works for any frequency and attempts to cancel the disturbance completely by generating a secondary signal of opposite phase. The disturbance FF control applies a control force that mimics the disturbance transmitted by the isolator but with an opposite sign. This type of control has two main advantages:

1. it does not affect the stability properties of the system because no control loop is closed. This enables disturbance suppression also at high frequencies.
2. it uses a direct measurement of the disturbance, which generally improves the signal-to-noise ratio.

As far as the active **control of the MPLAT** is concerned, the H-infinity control strategy is chosen. The document by A. Megretski [25] explains how the algorithm embedded in the MATLAB® *hinfsyn* command works. Since the MVMS has similar characteristics to a Stewart platform, the article by R. Breganon [9] has been analysed. It reports a theoretical description of the H-infinity control strategy and it shows a control scheme with weighting functions placed between the output from the plant and the performance signal. It is also reported that such weights represent the design specifications. The article by S. Jung [19] deals with a 2DoF spring-mass-damper system and shows how to minimise vibrations with H-infinity control (non-robust controller) and μ-synthesis (robust controller). The previous documents also deal with the selection of the weighting functions to obtain the desired performances, however the article by R. Beaven et al. [6] is entirely dedicated to this. However, although simple rules exist for the selection of weighting functions, the process is still subjective in nature. Also some MATLAB® documents are useful for the MPLAT control: *Robust Control of an Active Suspension* [23] and *H-Infinity Performance* [24]. The first one computes an H-infinity controller for the nominal system (two masses and a disturbance imposed from the ground) using the *hinfsyn* command. On the other hand, the second one is a tracking problem, with disturbance rejection, and control input signal limitations, which is strictly close to the problem of the MPLAT control.

0.3. Organization of the Thesis

In chapter 1, a general description of the facility is carried out, where its main features are highlighted, such as its measurement and excitation ranges, and the sensor and actuator

modes. In the same chapter, the architecture of the MVMS is described: it is composed of the VIBISIO and the MPLAT. Eventually, it is shown a geometrical model to describe the location of sensors and actuators.

In chapter 2, the dynamic models describing the MVMS physical system are studied. Furthermore, it is checked whether any lateral dynamics coupled to the longitudinal excitation are present. Eventually, the modal analysis is performed and the normal modes are displayed.

In chapter 3, the control designs for the VIBISIO (FB and FF) and for the MPLAT (H-infinity) are carried out. For both of them, the control strategies are described. Then, the results of their application to the 2DoF model first, and eventually to the condensed CB model are displayed.

In chapter 4, the conclusions of the work and the future possible developments are described.

1 | General Description of the MVMS

1.1. Main Features of the MVMS

The 6DoF MVMS testing facility, displayed in fig. 1.1, represents a very challenging project since it aims at operating on 6 DoFs: 3 translational and 3 rotational.

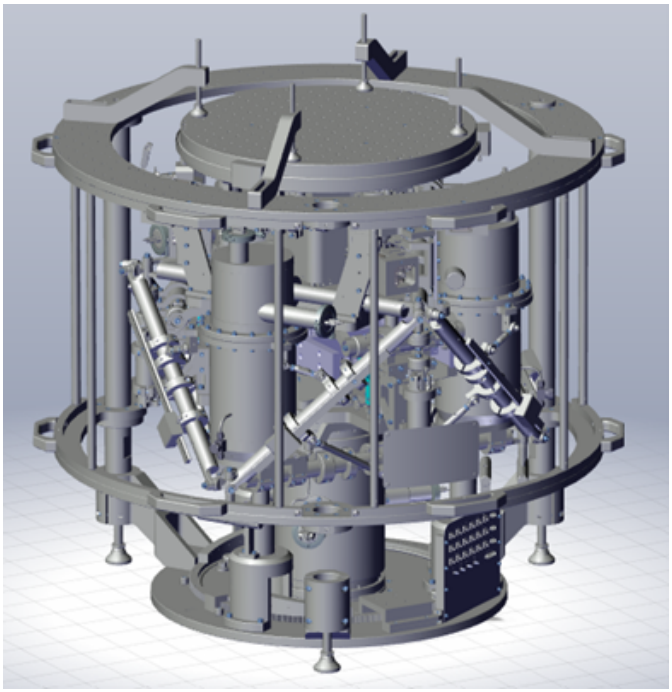

Figure 1.1: 6DoF MVMS facility
(*Image courtesy of ESA*)

The MVMS is 1.1 m high and the total weight is 650 kg. It has an industrial application and, in particular, is well suited for space industry to test the rotating components of satellites. It can work both in air and in vacuum, because its sealings are approved also for working in vacuum (vacuum compatibility), but it will be probably employed in air.

The facility can work according to two different modes; as a sensor or as an actuator.

- **Sensor/measurement mode**: the Item Under Test (IUT) fixed on the top plate starts to move, typically with a harmonic motion, generating some micro vibrations. The force generated by the actuators aims to compensate the force introduced by the IUT in such a way that the final MPLAT displacement is close to zero.
- **Actuator/excitation mode**: the objective is to isolate the IUT placed on the top plate from the micro vibrations generated by an excitation imposed from the ground.

The isolation from vibrations is performed both with an **active** system and a **passive** one. The active part consists of voice coil actuators, while the passive one involves two Minus-K. To allow an optimal attenuation, the 6 elastic constants of the springs of the Minus-K shall be tuned. This procedure would work as a passive mechanical low-pass filter, where the resonance would be so low that no vibration would arrive at the facility. The actuators present on the facility are reactive voice-coil, hence they are characterized by both a mechanical and an electrical dynamics. The mechanical dynamics concerns the lower frequencies, while the electrical dynamics regards the higher ones. An active control can therefore improve the damping of the resonance peaks and can help the passive control provided by the two Minus-K in increasing the roll-off at higher frequencies. Moreover, the active control can go beyond the mere increase in the damping, by causing the response to have transmissibility smaller than 1, which means 0 dB.

The MVMS is designed to perform the measurements and excitations of the test specimens with the following specifications:

- total weight: between 0.2 and 25 kg;
- static Centre of Gravity (CoG): from 10 cm to 30 cm;
- dynamic CoG shift: 10 cm;
- total dimensions: $50 \times 50 \times 50$ cm.

The facility is designed to measure and execute micro vibration forces, moments and accelerations in the frequency range from 0.03 Hz to 100 Hz. [14] As a matter of fact, the MVMS is also able to measure very low-frequency vibrations.
The minimum frequency of vibration that can be detected is obtained through the following formulas, where a is either the measured or the imposed acceleration and x is the actuator's displacement.

Being:

$$a = \ddot{x} \tag{1.1}$$

In the Laplace domain, it results that:

$$a = s^2 x \tag{1.2}$$

Since $s = j\omega$,

$$a = -\omega^2 x \tag{1.3}$$

By inverting eq. (1.3):

$$\omega = \sqrt{-\frac{a}{x}} \tag{1.4}$$

Being the maximum actuator's displacement x_{max} the constraint, the minimum circular frequency is:

$$\omega_{min} = \sqrt{-\frac{a}{x_{max}}} \tag{1.5}$$

Hence, the minimum frequency results to be:

$$f_{min} = \frac{\omega_{min}}{2\pi} = \frac{1}{2\pi}\sqrt{-\frac{a}{x_{max}}} \tag{1.6}$$

Since a negative sign is present under the square root, it is rigorous to specify that the computations are made considering the amplitudes of the acceleration and of the actuator's displacement, with their signs. Being X the maximum actuator's half-stroke, the relations are:

$$x = Xe^{j\omega t} \rightarrow x_{max} = X \tag{1.7}$$

and

$$a = \ddot{x} = -X\omega^2 e^{j\omega t} = Ae^{j\omega t} \tag{1.8}$$

where $A = -X\omega^2$ is the amplitude of the acceleration. It is evident that when the maxi-

mum actuator's stroke X is positive, A is negative and viceversa, therefore the radicand in eq. (1.6) is always positive. Thus, eq. (1.6) becomes:

$$f_{min} = \frac{\omega_{min}}{2\pi} = \frac{1}{2\pi}\sqrt{-\frac{A}{X}} \tag{1.9}$$

The following tables (table 1.1 and table 1.2) summarize the measurement and excitation ranges which characterize the facility, considering that the maximum actuator's half-stroke is approximately $\pm 2.5\ mm$. In particular, they respectively relate the accelerations induced by the specimen and the translational accelerations to be generated with the frequencies of vibration of the facility.

Table 1.1: 6DoF MVMS measurement ranges

Frequency Range	**Force induced by the specimen in all directions**	**Moments induced by specimen around its 3 main axes**	**Accelerations induced by specimen in all directions**
0.01 Hz to 0.32 Hz	$10^{-5}\ N$ to 0.1 N	$10^{-5}\ Nm$ to 0.1 Nm	$10^{-5}\ m/s^2$ to $10^{-2}\ m/s^2$; $10^{-5}\ rad/s^2$ to $10^{-2}\ rad/s^2$

Table 1.2: 6DoF MVMS excitation ranges

Frequency Range	**Translational accelerations to be generated**	**Rotational accelerations to be generated**
0.01 Hz to 0.32 Hz	$10^{-5}\ m/s^2$ to $10^{-2}\ m/s^2$	$10^{-5}\ rad/s^2$ to $10^{-2}\ rad/s^2$

1.2. Architecture of the MVMS

The 6DoF MVMS consists of two main subsystems:

- **VIBISIO**: vibration isolation platform, which is the lower subsystem.
- **MPLAT**: vibration measurement platform, which is the upper subsystem.

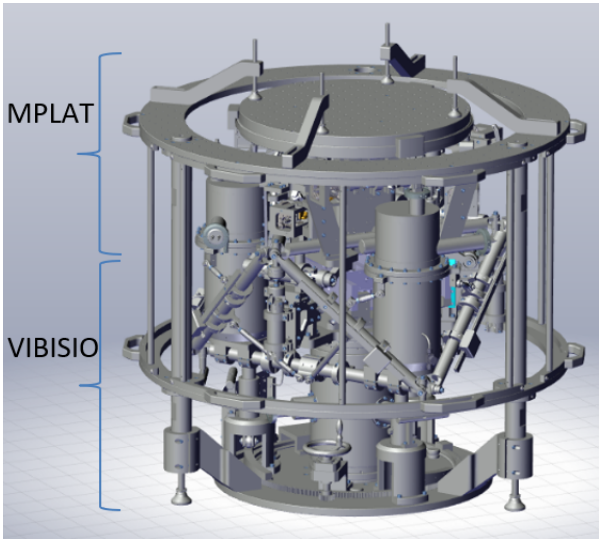

Figure 1.2: MPLAT and VIBISO of 6DoF MVMS
(*Image courtesy of ESA*)

1.2.1. The Vibration Isolation Platform (VIBISIO): Description

The function of the VIBISIO is to isolate the MPLAT from ground vibrations. It is an active isolation system, in which the background vibrations are measured by seismometers and the attenuation is performed actively via voice coil actuators. [14] The VIBISIO is a reticular structure which is already passively isolated by the first Minus-K, which lies on the interface with the ground and holds all the upper structure (VIBISIO and MPLAT), allowing its isolation from ground vibrations.
The actuators are necessary in the VIBISIO since the passive isolation alone cannot isolate from low-frequency oscillations, that are the ones of the Minus-K. Thus, 6 actuators push the VIBISIO such that they cancel the residual vibrations downstream of the Minus-K. Since the Minus-K is suspended from ground, also the actuators are suspended.

The vibration isolation platform (fig. 1.3) consists of the following elements:

1. ground base assembly with central seismometer;

2. passive Minus-K;
3. tetrahedral frame;
4. 3 upper seismometers;
5. balancing masses;
6. force actuator assemblies.

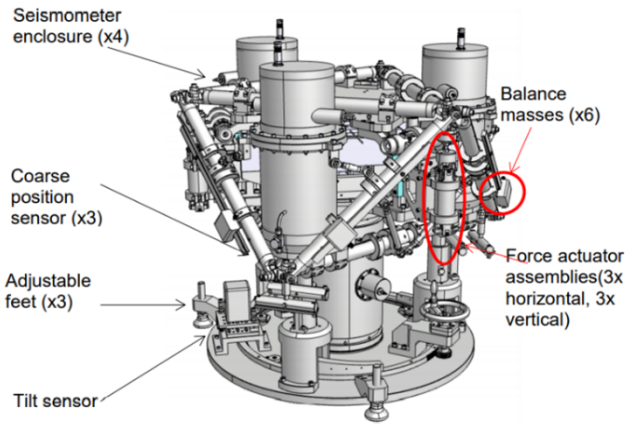

Figure 1.3: 6DoF MVMS VIBISIO
(*Image courtesy of ESA* [14])

The **ground base** (fig. 1.4) provides the facility interface to external environment via three adjustable feet. The **ground seismometer**, which is mounted in the central location of the ground base, measures the background vibrations in 6 DoFs. Moreover, the hand crank is used to lock and unlock the isolation platform and the ball joints are used to stabilise the platform while in the lock position.

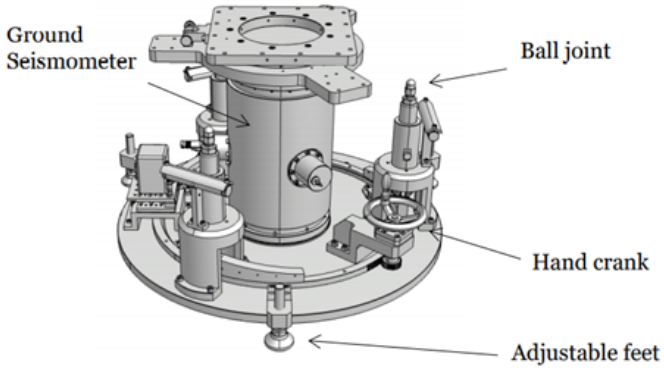

Figure 1.4: VIBISIO ground base
(*Image courtesy of ESA* [14])

The **passive Minus-K** model BM-1 (fig. 1.5) sits on top of the ground base and holds up the weight of both the isolation and measurement platforms. It enables the platform to move freely in 6 degrees of freedom.

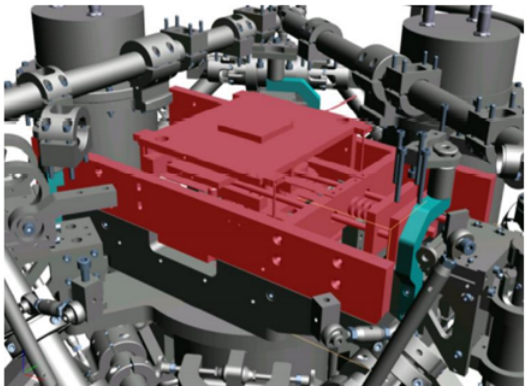

Figure 1.5: VIBISIO ground base
(*Image courtesy of ESA* [14])

The **tetrahedral frame** (fig. 1.6), which floats on the Minus-K, interconnects the **3 upper seismometers**, **balancing masses** and **6 force actuators assemblies** (fig. 1.7). The seismometers are used to measure the quality of VIBISIO damping by measuring the residual ground vibrations. The measured variables are the 3 upper seismometer's velocities in each DoF and the objective of the controller is to reduce them. The seismometers are placed inside sealed enclosures (fig. 1.8) in order to achieve the vacuum compatibility. The 6 force actuators assemblies actively damp the ground vibrations in 6 DoFs. [14] These actuators are reactive voice-coil: they are composed of a cylindrical body and a coil connected to the structure at their ends.

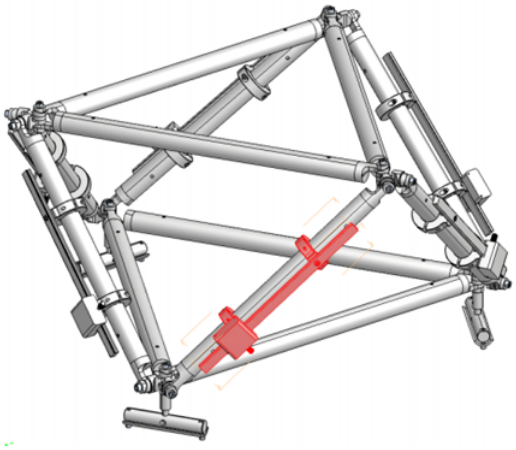

Figure 1.6: Tetrahedral Frame
(*Image courtesy of ESA* [14])

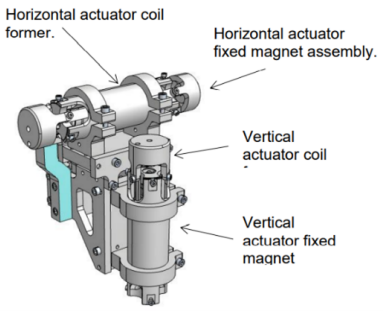

Figure 1.7: Voice coil force actuator assembly (*Image courtesy of ESA* [14])

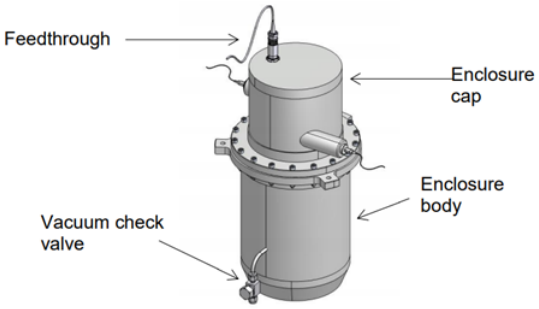

Figure 1.8: Seismometer enclosure (*Image courtesy of ESA* [14])

The VIBISIO has the same objective as a shaker placed on a seismic mass isolated from ground, which vibrates at an extremely low (negligible) frequency because the inertia is very large. Anyway, since the facility needs to be transportable, it has been preferred to use the VIBISIO rather than the seismic mass.

1.2.2. The Vibration Measurement Platform (MPLAT): Description

The function of the MPLAT is to perform the excitation of the test specimen and to measure its micro vibrations. The measurements are performed based on the zero-displacement principle. The idea is to keep the top interface plate in a zero-displacement position by active compensation of the forces induced by the test specimen via voice coil actuators. The zero displacement of the measurement platform is measured via Michelson type interferometers, while the total force generated by the test specimen is derived from the total force executed by the compensating voice coil actuators.

The vibration measurement platform (fig. 1.9) consists of the following elements:

1. specimen mounting plate;
2. interferometer assembly;
3. voice coil force actuator assembly;
4. balancing masses;
5. motion stops;
6. Minus-K model CM.

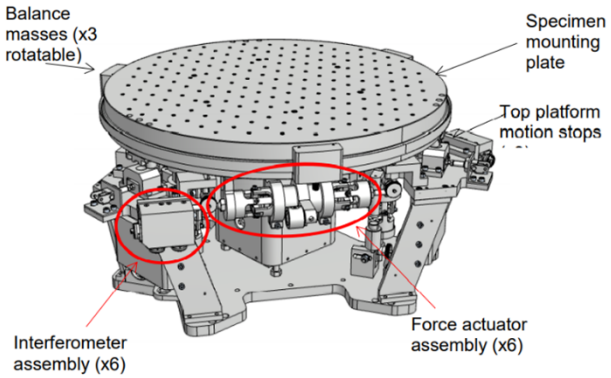

Figure 1.9: MPLAT
(*Image courtesy of ESA* [14])

The **specimen mounting plate** has a M6 threaded pattern (fig. 1.9), the spacing of which is 20 mm by 20 mm, in order to mount the test specimen on top of it. The reaction wheel, enclosed in its box, has flanges and screws (M6) which need to be screwed to the drilled top plate. The problem is that it is very rare that the drilling of the top plate corresponds to the position of the screws in the reaction wheel box. In this case, it is necessary to place one further intermediate plate which has drills compatible with the MPLAT in the lower part, while the upper part is drilled so as to be compatible with the reaction wheel box.

The **interferometer assembly** (fig. 1.10) measures the displacement between specimen mounting plate and frame holding the MPLAT Minus-K. There are six interferometer assemblies, each of which is measuring in one DoF. Hence, in total all 6 DoFs are measured. [14]

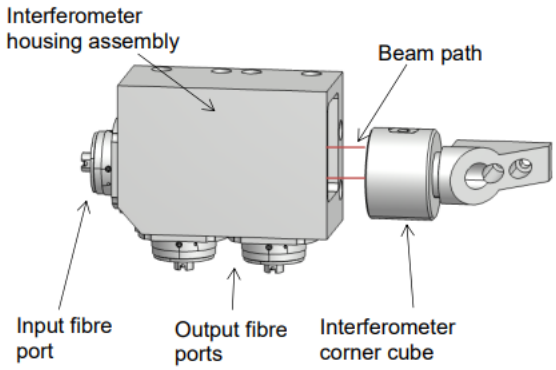

Figure 1.10: Interferometer assembly (*Image courtesy of ESA* [14])

The interferometer is designed based on the **Michelson** type, which is a common configuration for optical interferometry. Using a beam splitter, a light source is split into two arms. Each of those light beams is reflected back toward the beamsplitter which then combines their amplitudes using the superposition principle. [5] For the facility, a **homodyne** interferometer was chosen to ease measurement traceability, because of the fact that it uses a single-frequency HeNe laser source. A Michelson interferometer can be designed to give two output signals in-quadrature, allowing an absolute displacement measurement. The typical quadrature interferometer design introduces the 90^o phase difference between the outputs with a waveplate by utilising the polarisation properties of the input beam. As the polarisation state of the light in the fibre was found to vary significantly with any fibre strain, it was decided that a polarisation insensitive design was necessary to reduce measurement drift. This is achieved using an absorbing beam splitter, with a metallic coating tuned to ensure a quadrature output signals without the need for additional optics. [31]

The **Minus-K model CM** (fig. 1.11) is placed on top of the VIBISIO and allows the MPLAT to float in 6 DoFs, allowing to passively isolate the MPLAT from the VIBISIO.

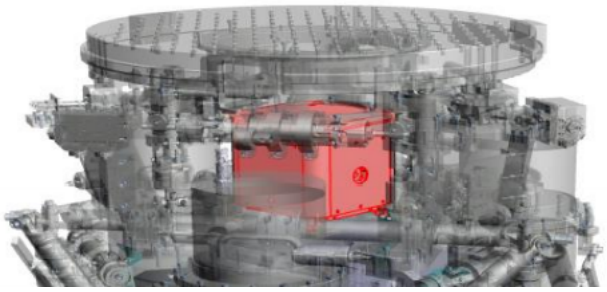

Figure 1.11: Minus-K of the MPLAT
(*Image courtesy of ESA* [14])

The Minus-K is made of 6 springs, above which the top plate of the MPLAT is mounted. On this top plate, six **voice coil force actuator assemblies** (fig. 1.12) are mounted, 3 of which are horizontal and the other 3 are longitudinal, which are identical in each DoF.

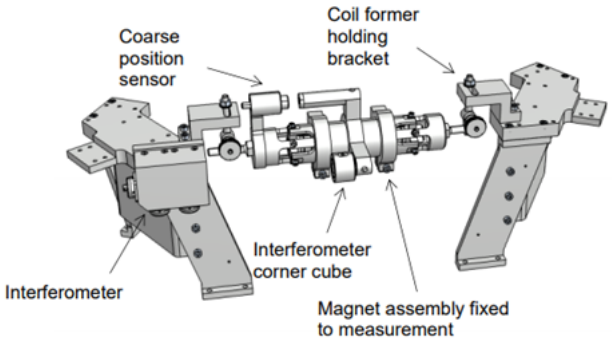

Figure 1.12: Voice coil force actuator assembly
(*Image courtesy of ESA* [14])

The function of the voice coil force actuators is to move the measurement platform during measurement and excitation modes.

- During **actuator mode**, these actuators are needed to impose vibrations: they move the MPLAT, so the facility behaves like a mechanical shaker. The Minus-K is mounted to isolate the MPLAT from the VIBISIO, allowing a double passive isolation, while the 6 actuators on the MPLAT are used to impose vibrations to the IUT.
- During **sensor mode**, the force generated by the actuators aims at compensating the force introduced by the IUT in such a way that the final MPLAT displacement is close to zero. The test specimen's force is derived based on the force produced by the actuators, which have the task of cancelling the displacement by keeping the MPLAT fixed. Knowing how much energy is necessary for the actuators to keep the MPLAT fixed, the energy generated by the IUT is also known. According to the action and reaction principle, the force is equal and opposite to the one that the test specimen is imposing from the top plate. Knowing the reaction of the actuator, it is possible to reconstruct forces and moments produced by the IUT placed above, basing on which it is then possible to define whether the test specimen is too noisy or not. This depends on whether the force or moment is under the threshold given by the mission requirement: if it is lower than the threshold, then the attitude sensor is acceptable and can be commercialized, while if it is higher, a surface superfinish is needed.

Three **balancing masses** (fig. 1.9) are attached to the edge of the specimen mounting table and are used to balance the CoG of the test equipment. In fact, depending on the shape and on the density distribution of the test specimen, the center of mass of the

MVMS is altered. To avoid this, 6 inertia masses can be moved to assume a configuration that aims at keeping the overall CoG always in the same position. 3 of these 6 masses are placed on the reticular structure of the VIBISIO, while the other 3 are disposed on a circumference on the MPLAT. More than one configuration is possible and is found by computing the static moment.

The **motion stops** (fig. 1.9) prevent the MPLAT form excessive movement, and are also used to lock the platform during transportation and initialisation procedure. [14]

1.3. Location of Sensors and Actuators

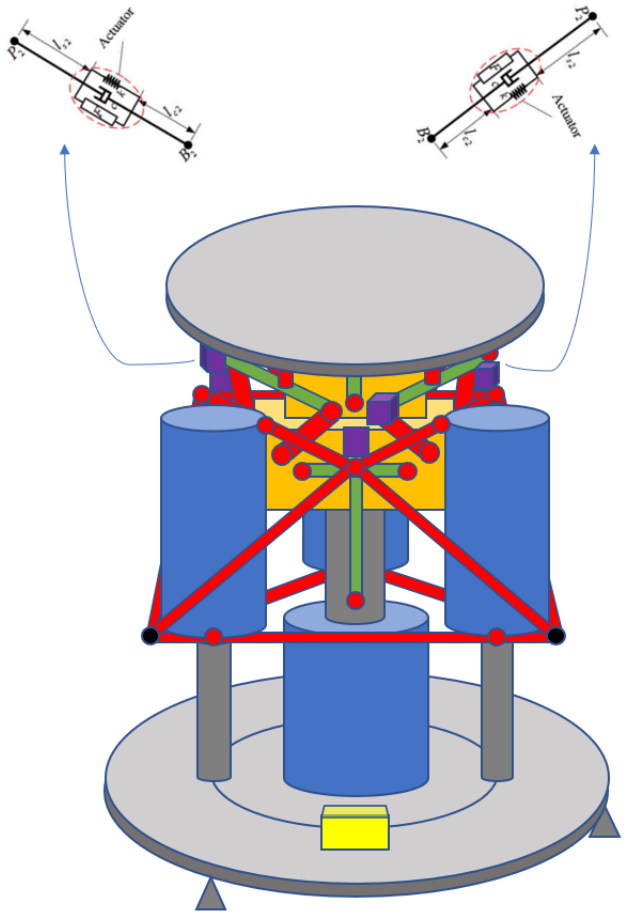

Figure 1.13: Geometric model

The geometric model of the facility is represented in fig. 1.13, where each colour in the drawing represents a different element:

- Red: trusses;
- Grey: generic structural elements.

Actuators:

- Green: voice-coil actuators (3×horizontal and 3×vertical in VIBISIO, 3×horizontal and 3×vertical in MPLAT);

Sensors:

- Blue: seismometers (×4);
- Violet: interferometers (×6);

- Yellow : tilt sensor (×1);
- Black: coarse position sensor (×3);
- Orange: VIBISIO Minus-K and MPLAT Minus-K.

2 | Dynamic Models and Modal Analysis

This chapter describes the dynamic models which represent the MVMS. They are designed in order to represent the full FEM model with simpler dynamical models. It is a step-by-step procedure of progressive reduction of the DoFs. These models are:

- full FEM model (section 2.1): 106,900 DoFs;
- CB model (section 2.2): 141 DoFs;
- Condensed CB model (section 2.3): 14 DoFs;
- 3DoF model (section 2.4): 3 DoFs;
- 2DoF model (section 2.4): 2 DoFs.

The CB models and the equivalent systems are validated. On the other hand, the full model still has to be validated with experiments. For describing the 141DoF CB model, it will also be checked whether any lateral dynamics coupled to the longitudinal excitation are present. Eventually, the modal analysis is performed and the normal modes are displayed.

2.1. 6DoF MVMS FEM

A finite element model of the MVMS facility was available before the beginning of the thesis. It had been developed using the technique of **super elements**, leading to a small size model which can be integrated in a global model.

2.1.1. Description of the 6DoF MVMS FEM

The 6DoF MVMS FEM is based on the CAD model and it is shown in fig. 2.1.

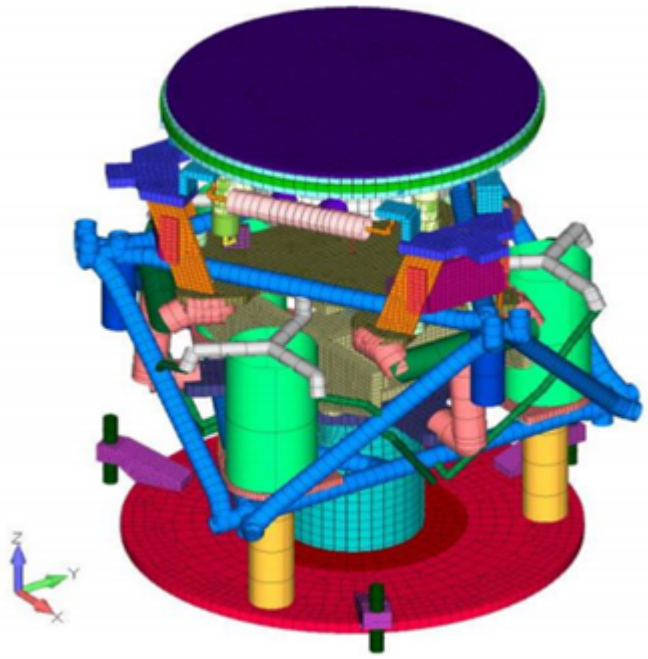

Figure 2.1: 6DoF MVMS FEM
(*Image courtesy of ESA* [14])

This model has been created based on several constraints:

- Mesh for 1D solid elements (rods, solid beams):
  - Type: Solid disc elements;
  - Density: At least 10 nodes per beam, roughly of 1 *cm* length.
- Fixed boundary conditions:
  - Location/surface: Bottom surface of three mounting feet,
    Constraint type: Fixed in 6DoFs;

  - Location/surface: Bottom surface of baseplate,
    Constraint type: Fixed in z-direction.

- Mass/material properties:
  - Material: AISI 316 stainless steel (blue colour in tetrahedral model);
  - Density: 8000 kg/m^3;
  - Young's modulus: 193 GPa;
  - Yield strength: 205 MPa.
- Loading/force conditions:
  - Self-weight on all components evenly distributed;
  - Point masses used at centre of geometry for seismometer of 15 kg;
  - Distributed mass of 50 kg used for top plate for specimen.
- Analysis:
  - Frequency range: 0 Hz to 2000 Hz;
  - Analysis program: NX Nastran™;
  - Analysis type: Normal Modes/Eigenvalue;
  - Real solution method: Lanczos.

The summary of the modes revealed by modal analysis is shown in fig. 2.2:

Description	Lowest resonance/ Hz
Minus-K	0.18
Bearing plate	120.78
Isolation platform top plate	132.69
isolation platform base plate	161.68
Isolation platform frame	178.36

Figure 2.2: Summary of the FEM modes
(*Image courtesy of ESA* [14])

In the following, the first 32 modes are described ascending order and are collected according to the part of the MVMS which they concern.

- **Minus-K modes**: The twelve lowest modes of the system are the resonant frequencies of the two Minus-K platforms. Each platform has one mode in each of the 6 DoFs, and these modes are necessary for the operation of the vibration isolation and measurement system. These frequencies are all in the order of 1 Hz.

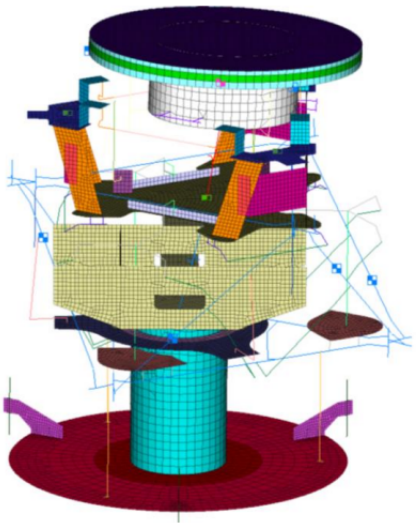

Minus-K Mode	Value / Hz
1	0.18
2	0.45
3	0.45
4	0.45
5	0.64
6	0.65
7	0.68
8	0.93
9	1.06
10	1.06
11	1.74
12	1.83

Figure 2.3: Minus-K modes
(*Image courtesy of ESA* [14])

- **Base bearing modes**: The lowest frequency structural resonant modes of the system occur on the bearing plate, which sits on top of the base of the isolation platform below the isolation Minus-K. These three "bearing plate" modes have an eigenfrequency at approximately 120 Hz.

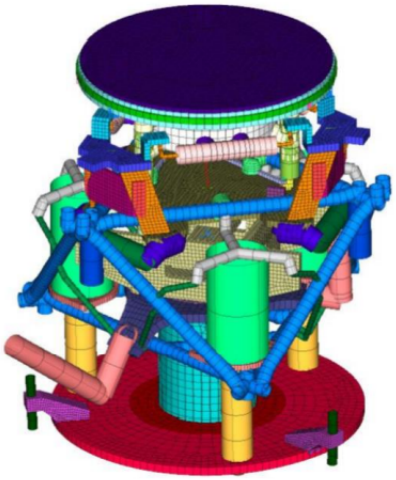

Bearing plate

Mode	Value / Hz
13	120.78
14	120.92
15	121.93

Figure 2.4: Base bearing modes
(*Image courtesy of ESA* [14])

- **Isolation platform top plate modes**: A set of modes occur at 130 Hz to 160 Hz on the top plate of the isolation platform. The FE model assumes that all balancing masses are present at their central point on the tetrahedral frame. This assumption is a worst-case scenario in this mode; removing or moving these masses is expected to raise the frequency of the isolation platform top plate modes.
  Furthermore, the measurement platform Minus-K is assumed to have no physical size. The actual Minus-K, when mounted on the top plate, will act to stiffen these modes.

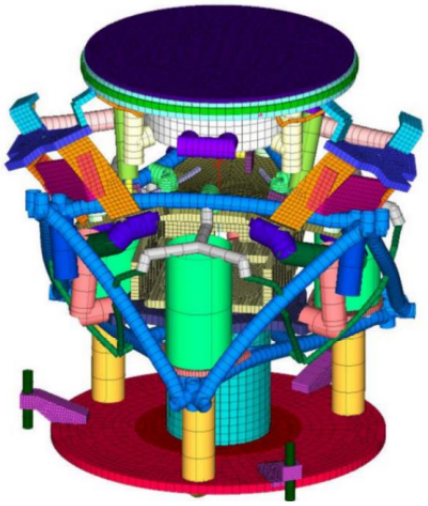

Isolation platform top plate

Mode	Value / Hz
16	132.69
17	133.46
18	147.09
19	148.08
20	152.10
21	153.01
22	154.15
23	159.07

Figure 2.5: Isolation platform top plate modes
(*Image courtesy of ESA* [14])

- **Base plate modes**: A set of drum head type modes can be seen between 160 Hz and 190 Hz on the base plate of the system base.

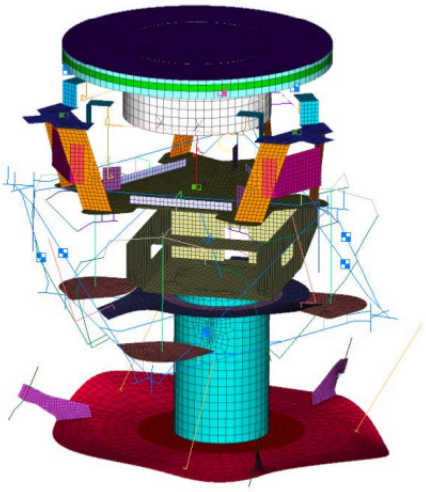

Isolation platform base plate

Mode	Value / Hz
24	161.68
25	161.74
28	185.02
30	187.70
31	187.87

Figure 2.6: Base plate modes
(*Image courtesy of ESA* [14])

- **Isolation platform tetrahedral frame modes**: The tetrahedral frame on the isolation platform has resonances between 170 Hz and 200 Hz.

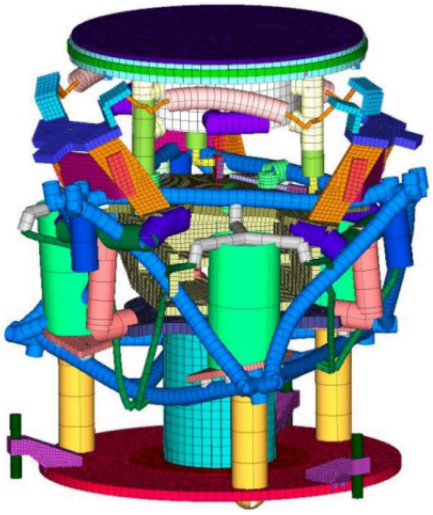

Isolation platform frame

Mode	Value / Hz
26	178.36
27	183.71
29	186.60
32	191.65

Figure 2.7: Isolation platform tetrahedral frame modes
(*Image courtesy of ESA* [14])

2.1.2. Overview of the Computational Methodology

Figure 2.8 provides a high-level all-inclusive overview of the computational methodology put in place to complete the Virtual Testing of MVMS system.

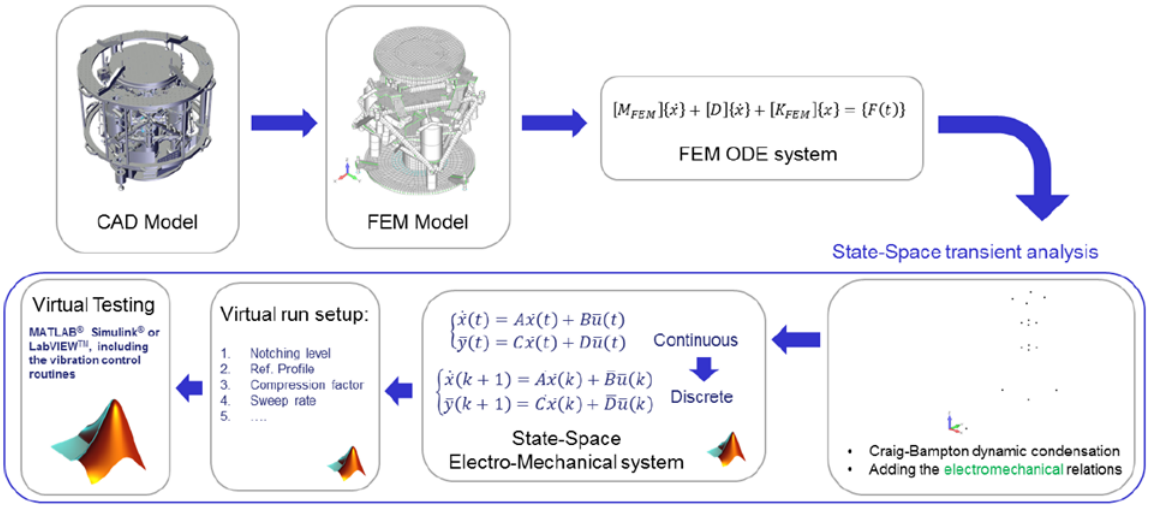

Figure 2.8: Overview of the computational methodology of MVMS Virtual Testing

Here is a step-by-step description of various blocks, in a consistent sequence.

- Starting from MVMS CAD model, the FE model is obtained and correlated after a test-campaign.
- The CB condensation is obtained after having selected the relevant interface (I/F) DoFs:
  - DoFs where electrical loading can act: for each actuator, a coil and a body DoF, appropriately oriented along the direction of actuation.
  - DoFs where constraints are applied (MVMS feet translational DoFs).
  - DoFs of I/F with other structures: 6 DoFs of the central node of the top MVMS plate and other eventual I/F nodes of interest, when merging possible models of IUTs.
  - Additional DoFs may be useful to observe for different reasons (e.g. for checks).
- The electrical and electromechanical submatrices are added to the CB mass and stiffness matrices.
- The damping matrix **D** can be obtained by assuming modal damping.

- The continuous State-Space (SS) matrices can be thus obtained from the so-obtained electromechanical **M** and **K** matrices.
- The discrete SS matrices can be now calculated from the continuous ones.
- Finally, the control parameter of the virtual run can be chosen (virtual run setup) and the virtual testing simulation can be run in MATLAB® Simulink® environment or LabVIEW™.

2.2. Craig-Bampton Model

The high number of DoFs of the full FEM model can be reduced by means of the CB condensation. In the following, it is first described how a CB condensation works, and then it is applied to the particular case of the MVMS facility. Subsequently, the CB matrices are extended to include the electromechanical coupled interactions and hence the state-space system is derived from FEM matrices. Eventually, it is checked the presence of any coupled dynamics following a longitudinal excitation.

2.2.1. Craig-Bampton Condensation: Definition

The CB method is a substructuring technique that reduces the number of internal DoFs of substructures by approximations, using a set of truncated normal modes. Thus, it is useful for structural analysis involving a high number of DoFs. [16]
This method is based on a re-formulation of the equations of motion for a structure from the set of physical coordinates to a set of coordinates consisting of **physical coordinates** at some subset of boundary points and **modal or generalized coordinates** at the non-boundary points. Once transformed to modal coordinates, mode shapes representing higher frequency responses may be truncated without loss of information.
The transformation is successful because the modes become uncoupled from each other, greatly reducing the manipulation required to solve the equations. Typically, **modal displacements and accelerations** are computed by numerical integration for a given set of initial conditions and forcing function time histories. **Physical accelerations and displacements** follow from the CB transformation matrix. [12]
In order to take a system of equations from the physical domain into a CB form, a few steps are involved. Firstly, the DoFs are partitioned into two sets: the **boundary set** (the b-set), where this substructure will eventually be interfaced with another piece, and the **interior set** (the i-set) which are the remaining DoFs. [30]

The equation of motion ignoring the damping is:

$$\mathbf{M\ddot{u}} + \mathbf{Ku} = \mathbf{F} \tag{2.1}$$

where:

$$\mathbf{u} = \begin{Bmatrix} \mathbf{u}_b \\ \mathbf{u}_i \end{Bmatrix} \tag{2.2}$$

$$\mathbf{M} = \begin{bmatrix} \mathbf{M}_{bb} & \mathbf{M}_{bi} \\ \mathbf{M}_{ib} & \mathbf{M}_{ii} \end{bmatrix} \tag{2.3}$$

$$\mathbf{K} = \begin{bmatrix} \mathbf{K}_{bb} & \mathbf{K}_{bi} \\ \mathbf{K}_{ib} & \mathbf{K}_{ii} \end{bmatrix} \tag{2.4}$$

The physical coordinates can then be transformed into CB coordinates using the transformation:

$$\mathbf{u} = \begin{Bmatrix} \mathbf{u}_b \\ \mathbf{u}_i \end{Bmatrix} = \begin{bmatrix} \mathbf{I}_{bb} & \mathbf{0}_{bk} \\ \boldsymbol{\psi}_{ib} & \boldsymbol{\phi}_{ik} \end{bmatrix} \begin{Bmatrix} \mathbf{u}_b \\ \mathbf{q}_k \end{Bmatrix} = \mathbf{T}_{CB} \begin{Bmatrix} \mathbf{u}_b \\ \mathbf{q}_k \end{Bmatrix} \tag{2.5}$$

where:

- $\mathbf{u}_b$: boundary DoFs;
- $\mathbf{u}_i$: internal (leftover) DOFs;
- $\boldsymbol{\psi}_{ib}$: rigid body vector;
- $\boldsymbol{\phi}_{ik}$: fixed base mode shapes;
- $\boldsymbol{q}_k$: modal DoFs.

The $\mathbf{T}_{CB}$ matrix in eq. (2.5) is the CB transformation matrix. [15] In the transformation matrix, the first column partition are the **fixed-interface modes**. These can be described as the interior DoF motion when the interface is fixed (or constrained in all I/F DoFs). [30] The number of kept fixed I/F modes can be reduced to k in order to decrease the total number of DoFs.
The second column partition represents the **constraint modes**. These describe the motion of the system when each boundary DoF is given a unit displacement while holding the other boundary DoFs fixed. [30]
$\mathbf{q}_k$ is a set of displacements corresponding to the **fixed-interface motion** and $\mathbf{u}_b$ is preserved from the original equation of motion as the **boundary physical DoFs**. [30]
Combining eq. (2.1) and eq. (2.5) and pre-multiplying by $\mathbf{T}_{CB}^T$:

$$\mathbf{T}_{CB}^T \mathbf{M} \mathbf{T}_{CB} \begin{Bmatrix} \ddot{\mathbf{u}}_b \\ \ddot{\mathbf{q}}_k \end{Bmatrix} + \mathbf{T}_{CB}^T \mathbf{K} \mathbf{T}_{CB} \begin{Bmatrix} \mathbf{u}_b \\ \mathbf{q}_k \end{Bmatrix} = \mathbf{T}_{CB}^T \begin{Bmatrix} \mathbf{F}_b \\ \mathbf{F}_k \end{Bmatrix} \tag{2.6}$$

By means of the transformation matrix, the subcomponent mass and stiffness matrices

are transformed into their CB formulations:

$$\mathbf{M}_{CB} = \mathbf{T}_{CB}^T \mathbf{M} \mathbf{T}_{CB} = \begin{bmatrix} \mathbf{M}_{bb} & \mathbf{M}_{bk} \\ \mathbf{M}_{kb} & \mathbf{M}_{kk} \end{bmatrix} \tag{2.7}$$

$$\mathbf{K}_{CB} = \mathbf{T}_{CB}^T \mathbf{K} \mathbf{T}_{CB} = \begin{bmatrix} \mathbf{K}_{bb} & \mathbf{0} \\ \mathbf{0} & \mathbf{K}_{kk} \end{bmatrix} \tag{2.8}$$

By writing eq. (2.6) using eq. (2.7) and eq. (2.8):

$$\begin{bmatrix} \mathbf{M}_{bb} & \mathbf{M}_{bk} \\ \mathbf{M}_{kb} & \mathbf{M}_{kk} \end{bmatrix} \begin{Bmatrix} \ddot{\mathbf{u}}_b \\ \ddot{\mathbf{q}}_k \end{Bmatrix} + \begin{bmatrix} \mathbf{K}_{bb} & \mathbf{0} \\ \mathbf{0} & \mathbf{K}_{kk} \end{bmatrix} \begin{Bmatrix} \mathbf{u}_b \\ \mathbf{q}_k \end{Bmatrix} = \begin{Bmatrix} \mathbf{F}_b \\ \mathbf{0} \end{Bmatrix} \tag{2.9}$$

where input forces are applied at the boundary only ($\mathbf{F}_k = \mathbf{0}$).
Important properties of the CB mass and stiffness matrices are:

- $\mathbf{M}_{bb}$: the boundary mass matrix represents the total mass properties translated to the boundary points.
- $\mathbf{K}_{bb}$: the I/F stiffness matrix represents the stiffness associated with displacing one boundary DoF while the others are held fixed. If the boundary point is a single grid, then $\mathbf{K}_{bb} = \mathbf{0}$.
- If the mode shapes have been mass normalized (typically they are), then:

$$\mathbf{M}_{kk} = \begin{bmatrix} \backslash & & 0 \\ & 1 & \\ 0 & & \backslash \end{bmatrix} = \mathbf{I} \tag{2.10}$$

$$\mathbf{K}_{kk} = \begin{bmatrix} \backslash & & 0 \\ & \lambda_i & \\ 0 & & \backslash \end{bmatrix} = \boldsymbol{\omega}^2 \tag{2.11}$$

  where $\lambda_i = k_i/m_i = \omega_i^2$.

Finally, the dynamic equation of motion (including damping) can be written using the CB transformation as:

$$\underbrace{\begin{bmatrix} \mathbf{M}_{bb} & \mathbf{M}_{bk} \\ \mathbf{M}_{kb} & \mathbf{I} \end{bmatrix}}_{\mathbf{M}_{CB}} \underbrace{\begin{Bmatrix} \ddot{\mathbf{u}}_b \\ \ddot{\mathbf{q}}_k \end{Bmatrix}}_{\ddot{\mathbf{u}}_{CB}} + \underbrace{\begin{bmatrix} \mathbf{0} & \mathbf{0} \\ \mathbf{0} & 2\xi\boldsymbol{\omega} \end{bmatrix}}_{\mathbf{Damp}_{CB}} \underbrace{\begin{Bmatrix} \dot{\mathbf{u}}_b \\ \dot{\mathbf{q}}_k \end{Bmatrix}}_{\dot{\mathbf{u}}_{CB}} + \underbrace{\begin{bmatrix} \mathbf{K}_{bb} & \mathbf{0} \\ \mathbf{0} & \boldsymbol{\omega}^2 \end{bmatrix}}_{\mathbf{K}_{CB}} \underbrace{\begin{Bmatrix} \mathbf{u}_b \\ \mathbf{q}_k \end{Bmatrix}}_{\mathbf{u}_{CB}} = \underbrace{\begin{Bmatrix} \mathbf{F}_b \\ \mathbf{0} \end{Bmatrix}}_{\mathbf{F}_{CB}} \tag{2.12}$$

where $2\xi\boldsymbol{\omega}$ is the modal damping. ξ is the damping ratio and it is defined as $\frac{c}{c_{critical}}$, where $c_{critical} = 2\sqrt{km}$. [15]

2.2.2. MVMS Craig-Bampton Condensation: Computation

The list of CB I/F DoFs of MVMS FE model can start from the actuator DoFs. Actuators are labelled and numbered as it follows:

```
ACT_VB_L_+X__  (n. 5)
ACT_VB_H_+X__  (n. 6)

ACT_VB_L_-X+Y  (n. 3)
ACT_VB_H_-X+Y  (n. 4)

ACT_VB_L_-X-Y  (n. 1)
ACT_VB_H_-X-Y  (n. 2)

ACT_MP_L_+X__  (n. 7)
ACT_MP_H_-X__  (n. 10)

ACT_MP_H_+X+Y  (n. 12)
ACT_MP_H_+X-Y  (n. 11)

ACT_MP_L_-X+Y  (n. 9)
ACT_MP_L_-X-Y  (n. 8)
```

Where:

- ACT = Actuator;
- VB = VIBISO;
- MP = MPLAT;
- L = Longitudinal;
- H = Horizontal;

- X and Y are the MVMS global axis with signs, identifying the location of the actuator.

For the sake of simplicity, dedicated local coordinates are considered for the actuators, as a convention:

- DoF1 = longitudinal actuation;
- DoF2 = horizontal actuation.

Figure 2.9 provides a view of the dedicated local analysis coordinates purposely defined for the FE nodes of the various actuators.

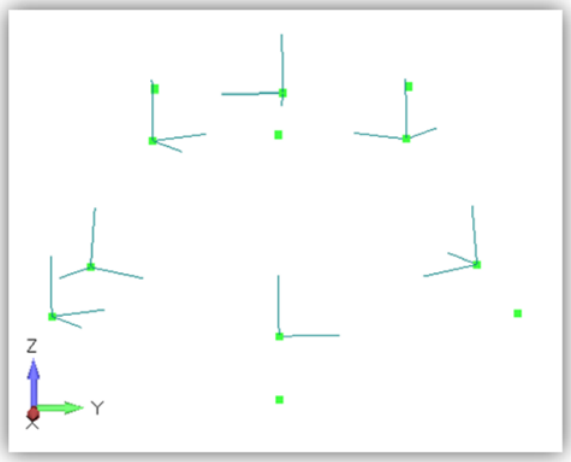

Figure 2.9: Image of the dedicated local analysis coordinates purposely defined for the FE nodes of the actuators
(*Image courtesy of ESA*)

Figure 2.10 provides, for each actuator, some details like the Upper and Lower nodes, respectively indicating the actuator Coil and Body nodes. Moreover, the CB matrices index associated to each one of those nodes is reported. Such index is driven by the fact that MSC Nastran™ orders the DoFs from lower to higher node numbers and, for each node, the DoFs existing (and retained as I/Fs in the CB condensation) are listed from 1 to 6.

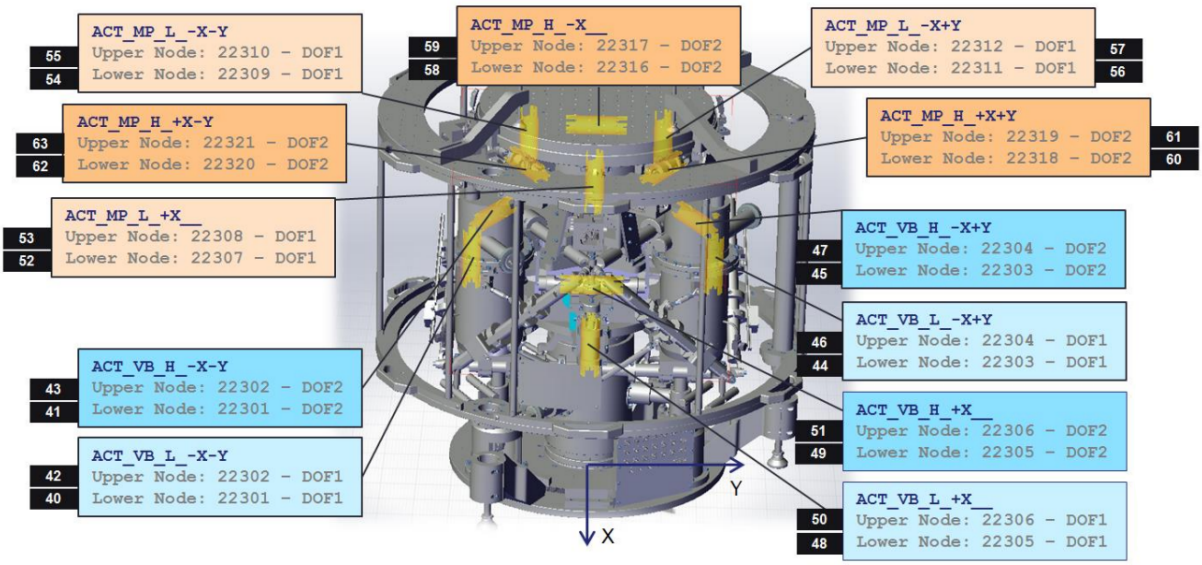

Figure 2.10: Image of dedicated local analysis coordinates purposely defined for FE nodes of the actuators
(*Image courtesy of ESA*)

Additional CB I/F nodes of interest are given in the fig. 2.11. Matrices indices are here provided for the relevant node involved in the possible rigid merge with an IUT.

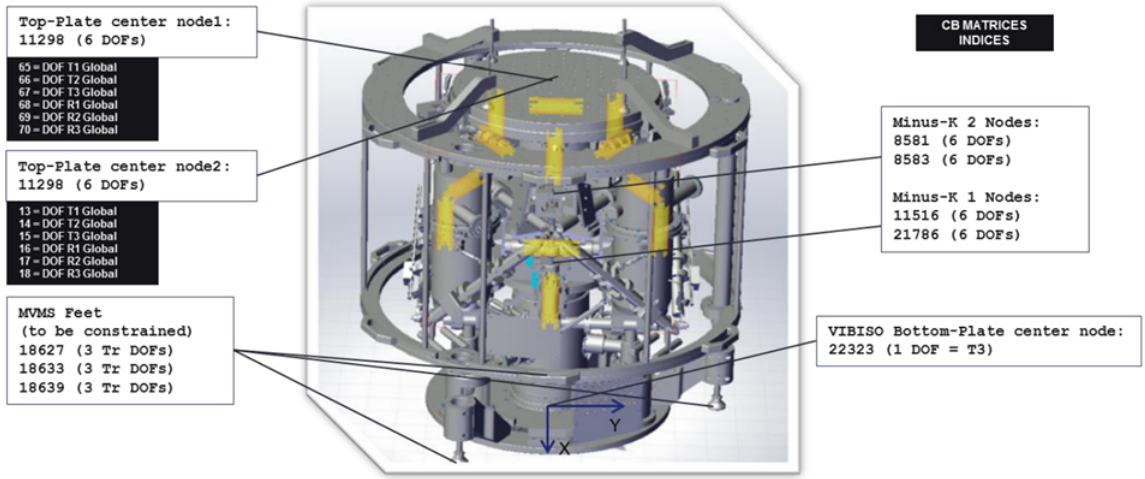

Figure 2.11: Additional CB I/F nodes of interest
(*Image courtesy of ESA*)

Figure 2.12 provides the spy view of MVMS FE CB condensed mass and stiffness matrices in empty configuration, together with the corresponding modal damping matrix. Their structure complies with the one of $\mathbf{M}_{CB}$, $\mathbf{Damp}_{CB}$ and $\mathbf{K}_{CB}$ in eq. (2.12).

CB matrices details:

- Number of I/F DoFs: 70;
- Selected modal base: $[0, 500]\ Hz$, leading to 56 modes;
- Subsequent dimension of CB matrices: 141×141;
- The damping matrix $\mathbf{Damp}_{CB}$ is the diagonal matrix having the modal damping $2\xi\omega_n$ at the (n, n) position for the n^{th} mode (modal damping assumption). In this sense the $\mathbf{Damp}_{CB}$ matrix is not a direct result of the CB condensation.

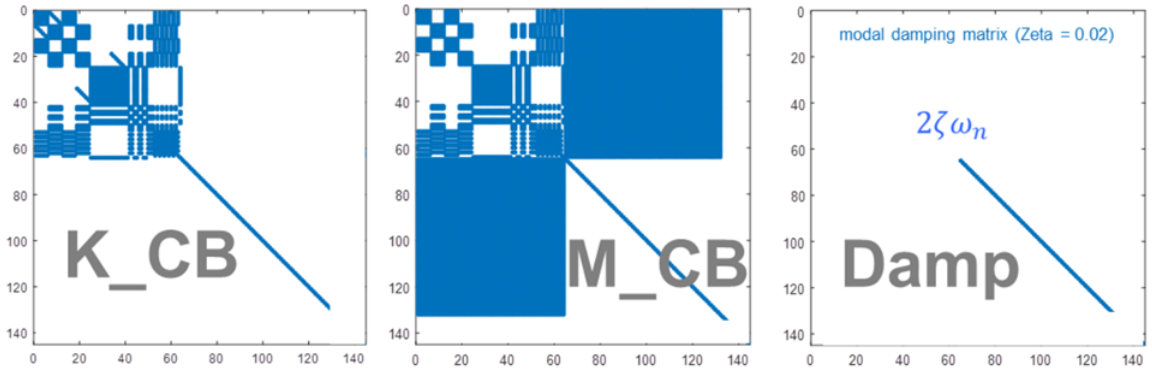

Figure 2.12: Some details about MVMS CB stiffness and mass matrices and the Damping matrix

2.2.3. Electromechanical Model of the 6DoF MVMS

In the following, a simplified model of the facility is retrieved. This is the basis on which the control system is designed. Firstly, the electromechanical model of the classical single-axis shaker is shown, and then the the electromechanical modeling will be extended to MVMS multishaker.

Electromechanical Model of the Classical Single-Axis Shaker

The fundamental electromechanical interactions of a classical lumped single-axis shaker system are recalled hereafter, on the basis of document [22] (see fig. 2.13 and fig. 2.14). This represents the starting point of the multifield description of a generic multiaxial shaker, that is the case of MVMS facility.

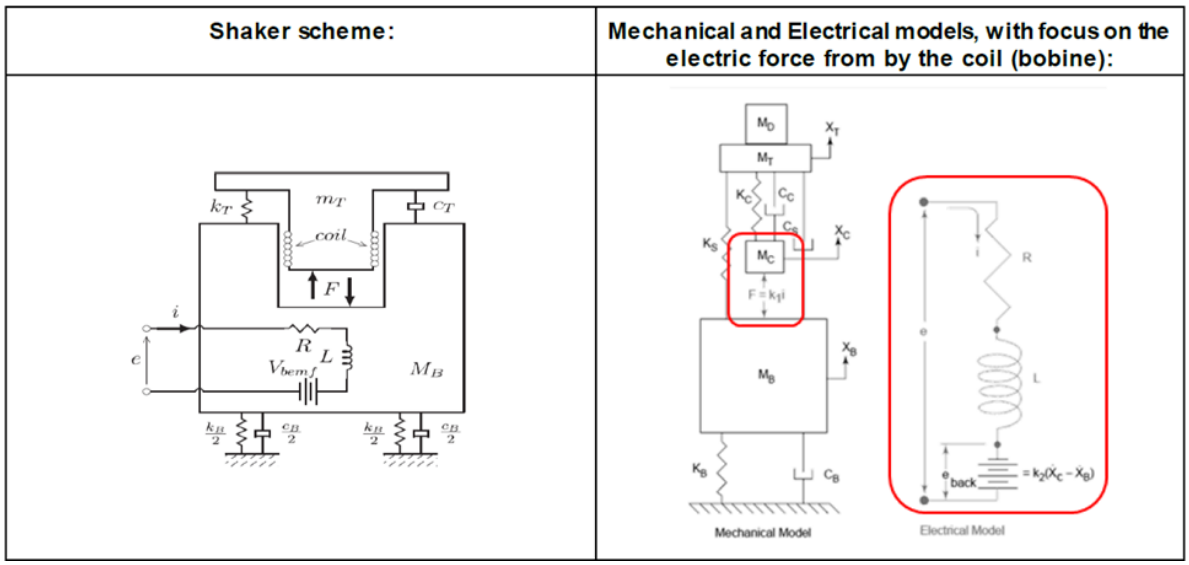

Figure 2.13: Single-axis electromechanical shaker lumped model [22]

By indicating in blue the purely mechanical interactions and in green the electrical and electromechanical coupling interactions, the following algebraic relations can be written (fig. 2.14).

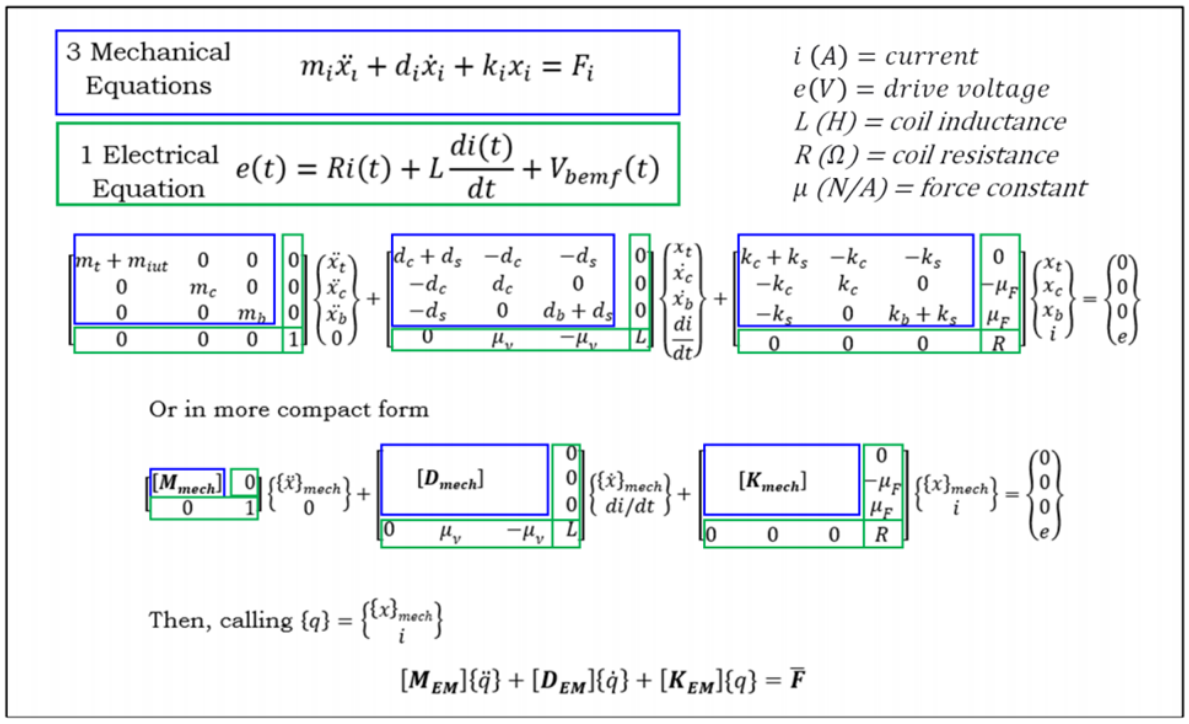

Figure 2.14: Electromechanical algebraic relations of a classical single-axis shaker. (*For additional details, see [22]*)

Extension of the Electromechanical Modeling to MVMS Multi-shaker

The model description given above for a single-axis electromechanical shaker is now extended to consider electromechanical multishakers, like the MVMS. The most significant differences of MVMS with respect to the classical single-axis case of 3 mechanical DoFs illustrated before are the following:

- The MVMS mechanical model is a FE model and thus it involves a significantly high number of DoFs (fig. 2.15). Therefore, a dynamic reduction by means of the CB method is included into the computational loop.
- The number of actuators in MVMS is equal to 12, and not just one, as for the classical single-axis shaker case (fig. 2.16). This implies to grow of 11 indices the matrices (or the vectors) expressing the electrical and electromechanical relations in fig. 2.14.

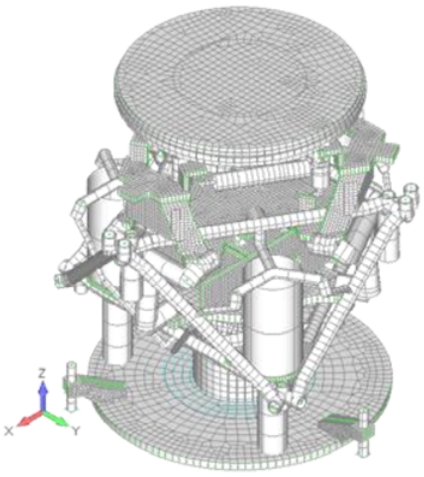

Figure 2.15: MVMS FE model (*Image courtesy of ESA*)

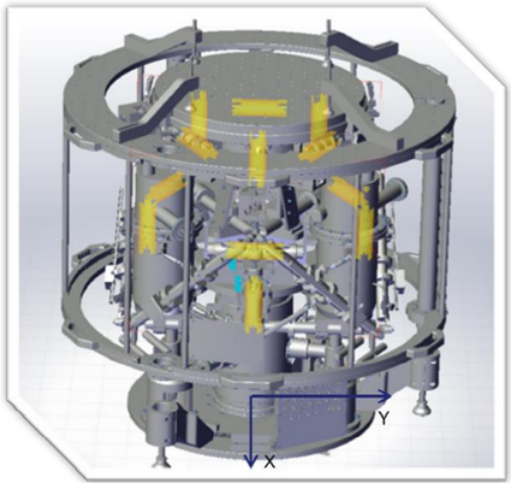

Figure 2.16: MVMS 12 actuators (*Image courtesy of ESA*)

Extension of Mechanical CB Matrices to include the Electromechanical Coupled Interactions

The mechanical CB matrices have been extended to include the electromechanical coupled interactions by following the same technique illustrated in fig. 2.14 for the case of a classical single-axis shaker. With MVMS, the difference is that 12 actuators are now present instead of just one. The convenient submatrixing naming convention shown in fig. 2.17 is used in the following.

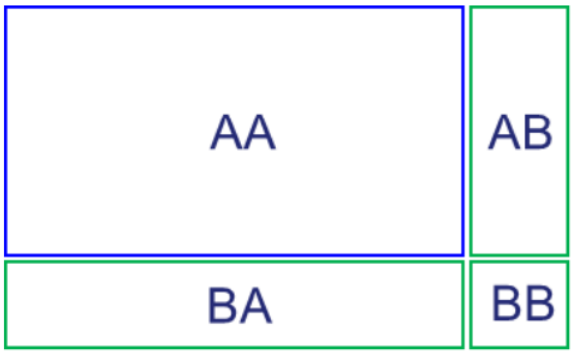

Figure 2.17: Submatrixing naming convention

It is necessary to populate the electrical and electromechanical submatrices **AB**, **BA** and **BB**, which have to be merged to the mechanical submatrix **AA** in order to obtain the electromechanical complete matrices. Figure 2.18 provides the information about electromechanical coefficients of **AB**, **BA** and **BB** submatrices, together with the respective matrix position of the electrical and electromechanical coefficients.
The parameters values which are relevant for the following passages are reported hereafter:

L (H) = 0.006 H
R = 6
μ = 2.5 N/A

The "1s" (ones) along the diagonal of **BB** mass submatrix are placed just in order to allow the matrix inversion and they have no impact on the system unknowns, as it is algebraically evident from the classical system in fig. 2.14. The matrices resulting from the inclusion of electrical and electromechanical coupling coefficients besides the mechanical ones is illustrated in fig. 2.19.

Parameter	Typical value	
Force constant	2.5	N/A
Resistance	6	Ω
Inductance	0.6	mH
Time constant	0.1	ms
Peak force	1.2	N
B field at 100 mm	< 0.1	mT

Figure 2.18: Actuator relevant electromechanical parameters

Figure 2.19 represents the spy view of MVMS FE CB condensed mass and stiffness matrices, together with the corresponding modal damping matrix, when they include the electromechanical coupled interactions.

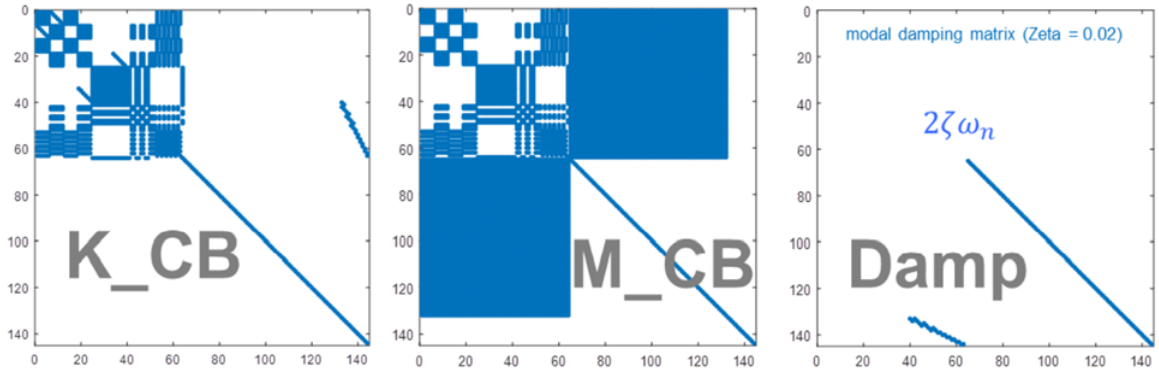

Figure 2.19: Matlab Multiphysics Model MVMS matrices: same matrices in fig. 2.12, now augmented with electrical and electromechanical coupling coefficients

2.2.4. Obtaining State-Space System from CB Matrices

The algebraic passages to obtain the electromechanical SS system are illustrated hereafter. The electromechanical coupled equations are the following:

$$\mathbf{M}_{CB}\,\ddot{\mathbf{u}}_{CB} + \mathbf{Damp}_{CB}\,\dot{\mathbf{u}}_{CB} + \mathbf{K}_{CB}\,\mathbf{u}_{CB} = \mathbf{F}_{CB} \tag{2.13}$$

where $\mathbf{u}_{CB}$ is the unknown vector and $\mathbf{F}_{CB}$ is the vector of multifield external loading, which can be mechanical or electrical, depending on the index considered.

By defining the extended vector of unknowns as:

$$\mathbf{x} = \begin{Bmatrix} \mathbf{u}_{CB} \\ \dot{\mathbf{u}}_{CB} \end{Bmatrix} \tag{2.14}$$

the system can be rewritten as:

$$\begin{bmatrix} -\mathbf{I} & \mathbf{0} \\ \mathbf{0} & \mathbf{M}_{CB} \end{bmatrix} \begin{Bmatrix} \dot{\mathbf{u}}_{CB} \\ \ddot{\mathbf{u}}_{CB} \end{Bmatrix} + \begin{bmatrix} \mathbf{0} & \mathbf{I} \\ \mathbf{K}_{CB} & \mathbf{Damp}_{CB} \end{bmatrix} \begin{Bmatrix} \mathbf{u}_{CB} \\ \dot{\mathbf{u}}_{CB} \end{Bmatrix} = \begin{Bmatrix} \mathbf{0} \\ \mathbf{F}_{CB} \end{Bmatrix} \tag{2.15}$$

It follows that:

$$\underbrace{\begin{Bmatrix} \dot{\mathbf{u}}_{CB} \\ \ddot{\mathbf{u}}_{CB} \end{Bmatrix}}_{\dot{\mathbf{x}}(t)} = \underbrace{\begin{bmatrix} \mathbf{0} & \mathbf{I} \\ -\mathbf{M}_{CB}^{-1}\mathbf{K}_{CB} & -\mathbf{M}_{CB}^{-1}\mathbf{Damp}_{CB} \end{bmatrix}}_{\mathbf{A}} \underbrace{\begin{Bmatrix} \mathbf{u}_{CB} \\ \dot{\mathbf{u}}_{CB} \end{Bmatrix}}_{\mathbf{x}(t)} + \underbrace{\begin{bmatrix} -\mathbf{I} & \mathbf{0} \\ \mathbf{0} & \mathbf{M}_{CB}^{-1} \end{bmatrix}}_{\tilde{\mathbf{B}}} \underbrace{\begin{Bmatrix} \mathbf{0} \\ \mathbf{F}_{CB} \end{Bmatrix}}_{\mathbf{u}(t)} \tag{2.16}$$

These equations can be rewritten in a more compact way by deleting the first column of the $\tilde{\mathbf{B}}$ matrix:

$$\underbrace{\begin{Bmatrix} \dot{\mathbf{u}}_{CB} \\ \ddot{\mathbf{u}}_{CB} \end{Bmatrix}}_{\dot{\mathbf{x}}(t)} = \underbrace{\begin{bmatrix} \mathbf{0} & \mathbf{I} \\ -\mathbf{M}_{CB}^{-1}\mathbf{K}_{CB} & -\mathbf{M}_{CB}^{-1}\mathbf{Damp}_{CB} \end{bmatrix}}_{\mathbf{A}} \underbrace{\begin{Bmatrix} \mathbf{u}_{CB} \\ \dot{\mathbf{u}}_{CB} \end{Bmatrix}}_{\mathbf{x}(t)} + \underbrace{\begin{bmatrix} \mathbf{0} \\ \mathbf{M}_{CB}^{-1} \end{bmatrix}}_{\mathbf{B}} \underbrace{\begin{Bmatrix} \mathbf{0} \\ \mathbf{F}_{CB} \end{Bmatrix}}_{\mathbf{u}(t)} \tag{2.17}$$

The SS continuous formalism is thus obtained:

$$\begin{cases} \dot{\mathbf{x}}(t) = \mathbf{A}\mathbf{x}(t) + \mathbf{B}\mathbf{u}(t) \\ \mathbf{y}(t) = \mathbf{C}\mathbf{x}(t) + \mathbf{D}\mathbf{u}(y) \end{cases} \tag{2.18}$$

We consider to receive velocities and accelerations as outputs, hence $\mathbf{y}(t) = \dot{\mathbf{x}}(t)$. Thus, it results that:

$$\mathbf{A} = \mathbf{C} = \begin{bmatrix} \mathbf{0} & \mathbf{I} \\ -\mathbf{M}_{CB}^{-1}\mathbf{K}_{CB} & -\mathbf{M}_{CB}^{-1}\mathbf{Damp}_{CB} \end{bmatrix} \tag{2.19}$$

$$\mathbf{B} = \mathbf{D} = \begin{bmatrix} \mathbf{0} \\ \mathbf{M}_{CB}^{-1} \end{bmatrix} \tag{2.20}$$

The above SS continuous system is a set of differential equations and it can be converted into a finite difference equation, leading to the discrete SS model:

$$\begin{cases} \mathbf{x}_{k+1} = \mathbf{A}\mathbf{x}_k + \mathbf{B}\mathbf{u}_k \\ \mathbf{y}_k = \mathbf{C}\mathbf{x}_k + \mathbf{D}\mathbf{u}_k \end{cases} \tag{2.21}$$

where the k index indicates the k^{th} time sample (to be set to 0.0001 according to fig. 2.18).

2.2.5. Solution with Inversion of the Dynamics Matrix

The procedure to obtain the response by means of the inversion of the dynamics matrix is explained in the following.

$$\mathbf{M}_{CB}\, \ddot{\mathbf{u}}_{CB} + \mathbf{Damp}_{CB}\, \dot{\mathbf{u}}_{CB} + \mathbf{K}_{CB}\, \mathbf{u}_{CB} = \mathbf{F}_{CB} \tag{2.22}$$

We can now identify with $\mathbf{a}_{CB}$ and $\mathbf{v}_{CB}$ the CB accelerations and velocities in the Laplace domain, respectively. Since $\mathbf{a}_{CB} = s^2\ \mathbf{u}_{CB}$ and $\mathbf{v}_{CB} = s\ \mathbf{u}_{CB}$, where $s = j\omega$, it results that $\mathbf{a}_{CB} = -\omega^2 \mathbf{u}_{CB}$ and $\mathbf{v}_{CB} = j\omega\ \mathbf{u}_{CB}$. Hence:

$$\mathbf{u}_{CB} = (-\omega^2\ \mathbf{M}_{CB} + j\omega\ \mathbf{Damp}_{CB}\ + \mathbf{K}_{CB})^{-1} \mathbf{F}_{CB} \tag{2.23}$$

The formula to obtain the magnitude of the acceleration values is:

$$\ddot{u}_{CB_i} = \omega^2 \mid u_{CB_i} \mid \tag{2.24}$$

2.3. Condensed Craig-Bampton Model

The reasons for the introduction of this model regard both the control of the VIBISIO and the control of the MPLAT:

1. For the VIBISIO control, in order to impose the excitation of a random load to the system, it is necessary to run simulations in the time domain. The FRFs retrieved from the Simulink® simulation with the full CB model are too noisy. These results have not improved even by increasing the simulation time (a singularity stops the simulation before 100 s of simulation time), by decreasing the fixed-time step nor by modifying the relative tolerance.
2. For the MPLAT control, simulations are run in the frequency domain, which best suits the application of the command *hinfsyn*. Since the **A** matrix of the 141DoF model is not full rank, the command *hinfsyn* returns an empty variable for the controller. For this reason, it has been necessary to employ a simpler model with a full-rank **A** matrix.

For these reasons, it has been necessary to introduce a condensed model of the CB one, with 14 DoFs: 3 physical and 11 modal DoFs. The condensation has been realised by considering only 3 nodes, as if they were the mass of the MPLAT, the mass of the VIBISIO and the large mass of the equivalent model. The DoFs of the physical part are 3 since we have:

- 1 DoF of vertical translation for the base mass to be constrained by means of a very large penalty parameter PE (10^{14});
- 2 DoFs of vertical translation for the remaining 2 nodes, corresponding to the VIBISIO and the MPLAT.

In table 2.1 is reported the correspondence between the DoFs of the nodes and the IDs of the cells of the mass and stiffness matrices.

Table 2.1: Correspondence between the DoFs and the IDs of the cells of $\mathbf{M}_{cond}$ and $\mathbf{K}_{cond}$

Node ID	Node description	CB condensation nodal DoFs	Node ID on the CB matrices
8581	MPLAT	vertical translation	1
11516	VIBISIO	vertical translation	2
21786	BASE	vertical translation	3

2.4. Equivalent Models: 2DoFs and 3DoFs

The 2DoF equivalent model consists of 2 masses, one above the other, connected to the ground and the one to the other through a spring and a damper, like in fig. 2.20. This system has 2 DoFs in the longitudinal direction, since the acceleration $\ddot{u}_0$ is imposed.

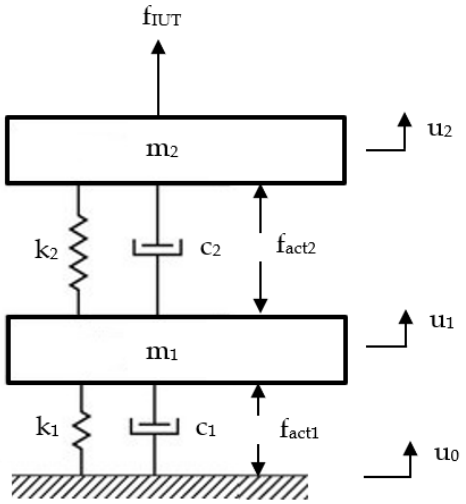

Figure 2.20: 2DoF model

The values of m_1, m_2, k_1 and k_2 have been retrieved in the following way. The FEM model is divided in Femap into these groups: MPLAT, VIBISIO, MVMS support, Minus-K of the MPLAT, Minus-K of the VIBISIO. The mass and stiffness properties are then extracted by selecting the elements of the interested group.
In order to calculate the structural dynamic response to base excitation, it is possible to employ the **Large Mass (LM) method** (see appendix A for a more detailed description). It consists of modelling the vibrating ground with a large mass m_0 and to connect it to a fixed ground with a low-stiffness spring k_0, as in fig. 2.21. This spring is necessary to help the numeric response by avoiding that the system becomes singular. In fact, if the system was not constrained, the determinant of the stiffness matrix would be zero. Instead, by adding k_0, the stiffness matrix is not singular and hence a solution can be computed.

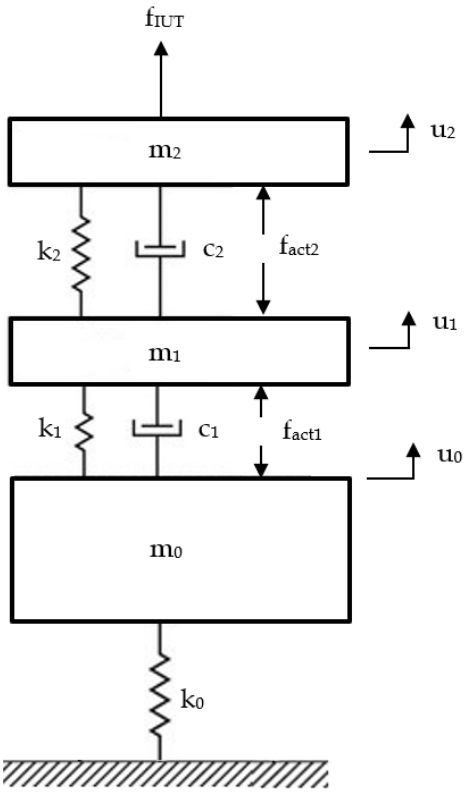

Figure 2.21: 3DoF model, with large mass

Considering that $f_{act1} = \mu i_1$ and $f_{act2} = \mu i_2$, and employing for the moment a viscous damping, the equations of motion of this model become:

$$\begin{bmatrix} m_1 & 0 & 0 \\ 0 & m_2 & 0 \\ 0 & 0 & m_0 \end{bmatrix} \begin{Bmatrix} \ddot{u}_1 \\ \ddot{u}_2 \\ \ddot{u}_0 \end{Bmatrix} + \begin{bmatrix} c_1 + c_2 & -c_2 & -c_1 \\ -c_2 & c_2 & 0 \\ -c_1 & 0 & c_1 \end{bmatrix} \begin{Bmatrix} \dot{u}_1 \\ \dot{u}_2 \\ \dot{u}_0 \end{Bmatrix} + \begin{bmatrix} k_1 + k_2 & -k_2 & -k_1 \\ -k_2 & k_2 & 0 \\ -k_1 & 0 & k_1 + k_0 \end{bmatrix} \begin{Bmatrix} u_1 \\ u_2 \\ u_0 \end{Bmatrix} = \begin{Bmatrix} \mu i_1 - \mu i_2 \\ \mu i_2 + f_{IUT} \\ -\mu i_1 + a m_0 \end{Bmatrix} \tag{2.25}$$

The addition of the LM causes the system to increase its number of DoFs from 2 to 3. The advantage of the LM method is that it allows to impose an arbitrary acceleration from ground by means of a force, while its drawback is that the results get numerically unstable.

The damping matrix can be modelled in three different ways:

- **Viscous damping**, with coefficients c_1 and c_2, computed as $c_i = 2\xi_i\sqrt{k_i m_i}$. The initial requirement was to tune the damping ratio according to an extinguishment of

the oscillations after 3 cycles. Anyway, other options have been explored in order to reproduce a similar behaviour to the one given by the other two types of damping.

- **Rayleigh damping**, where $\mathbf{C} = \alpha\mathbf{M} + \beta\mathbf{K}$, with α and β which are the Rayleigh coefficients. Here follows the theoretical procedure to derive such coefficients. Pre and post multiplying by the normal modes eigenvectors U_n gives:

$$U_n^T\mathbf{C}U_n = \alpha U_n^T\mathbf{M}U_n + \beta U_n^T\mathbf{K}U_n \tag{2.26}$$

The eigenvectors are used to diagonalize the mass and stiffness matrices such that for any mode using mass normalized eigenvectors:

$$U_n^T\mathbf{M}U_n = 1 \tag{2.27}$$

$$U_n^T\mathbf{K}U_n = \omega_n^2 \tag{2.28}$$

Although normal modes are not generally orthogonal to the damping matrix, a damping matrix which satisfies the condition $U_m^T\mathbf{C}U_n = 0$ ($m \neq$ n) is generated for a modal damping specification, i.e.:

$$U_n^T\mathbf{C}U_n = 2\xi_n\omega_n \tag{2.29}$$

So, from eq. (2.26) it results that:

$$2\xi_n\omega_n = \alpha + \beta\omega_n^2 \tag{2.30}$$

From which the damping terms are retrieved:

$$\xi_n = \frac{\alpha}{2\omega_n} + \frac{\beta\omega_n}{2} \tag{2.31}$$

That is to say the damping ratio is inversely proportional to the frequency for the mass contribution and directly proportional to the frequency for the stiffness contribution. This means Rayleigh damping is inappropriate outside the two frequencies which are typically used to calculate the factors α and β. The scale factors α and β can be calculated by a pair of simultaneous equations if ξ_m and ξ_n are known

for a pair of normal mode frequencies ω_m and ω_n. Typically ω_m will be chosen as one of the first fundamental frequencies of the system while ω_n is chosen somewhere among the higher frequencies of the modes that have significant contribution to the response. The damping ratio for these two modes is correct with somewhat lower damping between these two modes and considerably higher damping ratios outside the band covered by these two frequencies. Rayleigh damping therefore artificially damps the frequencies of the higher modes effectively eliminating their contribution to the response.

$$\begin{cases} \xi_m = \frac{\alpha}{2\omega_m} + \frac{\beta\omega_m}{2} \\ \xi_n = \frac{\alpha}{2\omega_n} + \frac{\beta\omega_n}{2} \end{cases} \tag{2.32}$$

By simultaneously solving eq. (2.32), the factors α and β are obtained:

$$\alpha = \frac{2\omega_m\omega_n}{(\omega_n^2 - \omega_m^2)}(\omega_n\xi_m - \omega_m\xi_n) \tag{2.33}$$

$$\beta = \frac{2\omega_m\omega_n}{(\omega_n^2 - \omega_m^2)}\left(\frac{\xi_n}{\omega_m} - \frac{\xi_m}{\omega_n}\right) \tag{2.34}$$

The variation of damping ratio with frequency is not often available, so typically a constant value of ξ is assumed. This sets $\xi_m = \xi_n = \xi$ reducing the factors to eq. (2.35) and eq. (2.36). [3]

$$\alpha = \frac{2\xi\omega_m\omega_n}{\omega_m + \omega_n} \tag{2.35}$$

$$\beta = \frac{2\xi}{\omega_m + \omega_n} \tag{2.36}$$

The input values are the eigenfrequencies ω_m and ω_n, and the damping ratio ξ. They are chosen with the aim of minimising the under-damp typical of the Rayleigh damping in the interval between the two selected frequencies f_m and f_n. In fact, due to its nature, the Rayleigh damping will naturally over-damp modes outside the frequency range used to calculate the damping values and under-damp the modes inside this frequency range; the correct damping is calculated at the two values of frequency chosen to calculate the values of α and β. [3] The chosen frequencies for this analysis are $f_m = 0.4\ Hz$, $f_n = 0.9\ Hz$, from which it results that $\omega_m = 2\pi f_m$ and $\omega_n = 2\pi f_n$. The adimensional damping ξ has been assumed equal to 0.05.

The resulting values of the Rayleigh coefficients are $\alpha = 1.7400 \cdot 10^{-1}$ and $\beta = 1.2243 \cdot 10^{-2}$. It is useful to illustrate the typical variation of the viscous damping coefficient ξ with the frequency f. It results that:

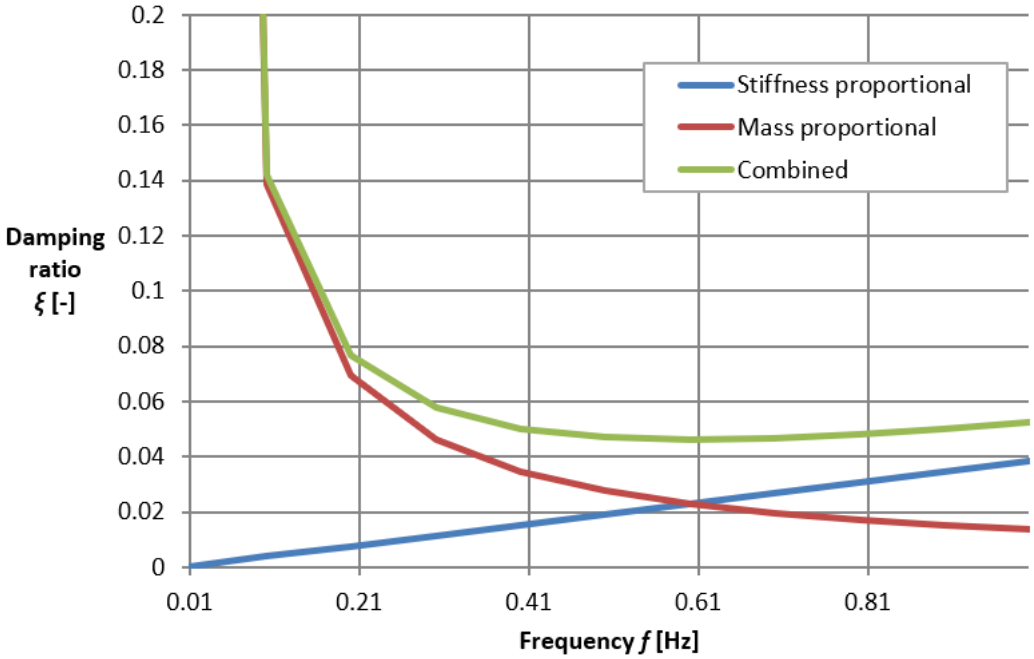

Figure 2.22: Rayleigh damping

From fig. 2.22 it can be noted that the damping ratio is sufficiently high in the frequency range of interest of the facility, which goes from 0.01 Hz to 0.2 Hz, since the two main resonance peaks of the frequency response functions are comprised within this interval. Moreover, from the same graph it results that the damping ratio in correspondence of f_m and f_n is equal to the chosen ξ, which in this case is 0.05.

Figure 2.23 and fig. 2.24 compare the frequency responses of the open-loop transmissibilities in the case of viscous and modal damping.

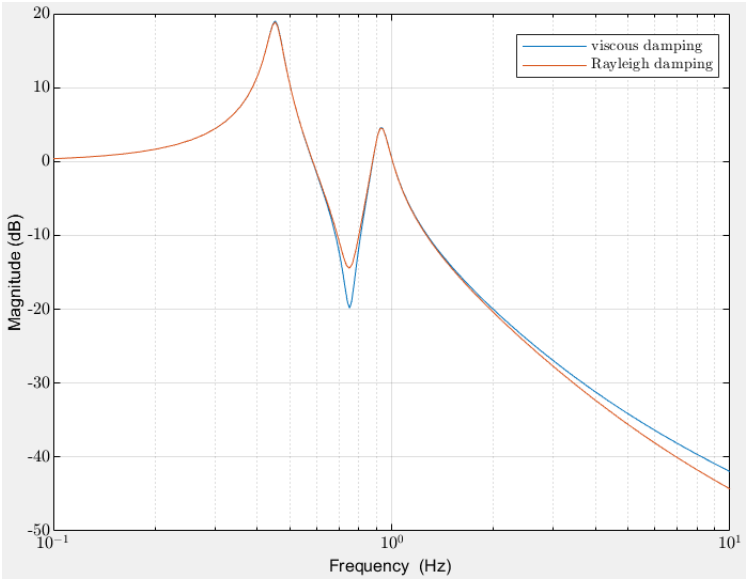

Figure 2.23: Open-loop transmissibility from a_0 to a_1: comparison between viscous and Rayleigh damping

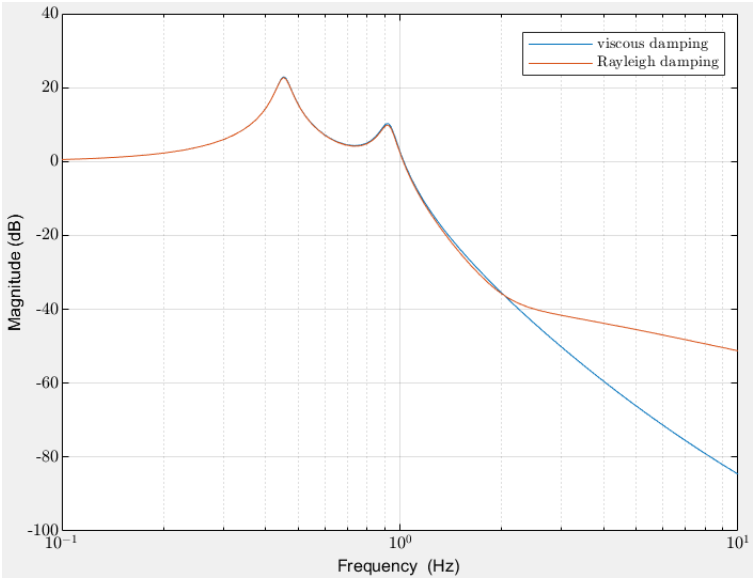

Figure 2.24: Open-loop transmissibility from a_0 to a_2: comparison between viscous and Rayleigh damping

From fig. 2.23 and fig. 2.24 it can be noted that the two frequency responses thoroughly overlap at lower frequencies, except for the anti-resonance in the transmissibility from a_0 to a_1, while they show a diverging behaviour at higher frequencies. Such a divergence is not relevant for the present study, since the significant frequencies are the lower ones, where the two resonance peaks are present. For this reason,

both a modal damping or a Rayleigh one can be employed.

- **Structural damping** with coefficient η=0.04, where an equivalent stiffness matrix is defined as: $\mathbf{K}' = \mathbf{K} + j\eta\mathbf{K}$.
  Structural damping assumes that the damping forces are proportional to the forces caused by stressing of the structure and are opposed to the velocity. Therefore, this form of damping can be used only when the displacement and velocity are exactly 90° out of phase. [26] When the equations of motion are transformed into the frequency domain by the Fourier transform, the damping force is seen to have a near 90° phase difference with respect to both the spring and inertial forces. [20] In the case of structural damping, the elastic force is given by the displacement multiplied by a real matrix, while the damping force is given by the displacement multiplied by a complex matrix. Performing the product $j\mathbf{K}$ means rotating the stiffness matrix by 90°. Hence, it is obtained a force in phase quadrature, which is the damping force.
  In a case different from structural damping, the damping force is obtained as the product of the damping matrix by the velocity. It still represents a damping, even though no multiplication by the imaginary unit is present. The reason stands in the definition of the velocity in the Laplace domain:

$$\mathbf{v} = s\mathbf{u} = j\omega\mathbf{u} \tag{2.37}$$

  where $\mathbf{v}$ is the velocity vector, u is the displacement vector and $s = j\omega$ is the Laplace variable, in which ω is the circular frequency. The product by the imaginary unit j gives a result in phase quadrature, which is a similarity with the structural damping. However, a difference between the two types of damping is given by the fact that, while in the case of damping force defined as $\mathbf{Cv}$, ω is variable with the frequency, the structural damping is instead constant with respect to the frequency.

For the present analysis, the chosen type of damping is the Rayleigh (proportional) one, in order to avoid the use of complex numbers and simplify computations. Only for the FF in the VIBISIO control it has been necessary to consider the viscous damping.

2.5. Frequency Response Functions

2.5.1. Validation of the Models

The considered values of the Rayleigh coefficients for the validation are $\alpha = 3.1338 \cdot 10^{-1}$ and $\beta = 7.9379 \cdot 10^{-5}$. They have been obtained with $\xi = 0.05$, $f_m = 0.5\ Hz$ and $f_n = 200\ Hz$. It emerges that the Rayleigh coefficients used in the validation are different with respect to the ones characterising the model to which the control will be applied (see section 2.4). In fact, in the latter case, those coefficients were tuned in a way to obtain the largest possible damping of the modes inside the frequency range of interest. This difference in the Rayleigh coefficients is not relevant since the validation of the models must be independent of the damping value.

The two main peaks of the frequency response function of the equivalent model correspond to the following resonance frequencies:

- $f_1 = 0.454\ Hz$
- $f_2 = 0.928\ Hz$

They match with the resonance frequencies of the CB model and of the condensed one. Moreover, for all these models it has been verified that the longitudinal modes have their correspondence also in the eigenvalue solution.

The validation of the CB model, the condensed CB model and the equivalent model has been made both by considering and not considering the LM method. The curves of all the frequency response functions (FRFs) overlap, as it can be noted from the following graphs. The results are displayed both dividing and not dividing by $\ddot{u}_0$, which means dividing or not by the average of the accelerations of the three feet of the facility. This distinction is done except for the case without LM, which is meaningful only if the acceleration is divided by $\ddot{u}_0$.

- With LM method, dividing by $\ddot{u}_0$:

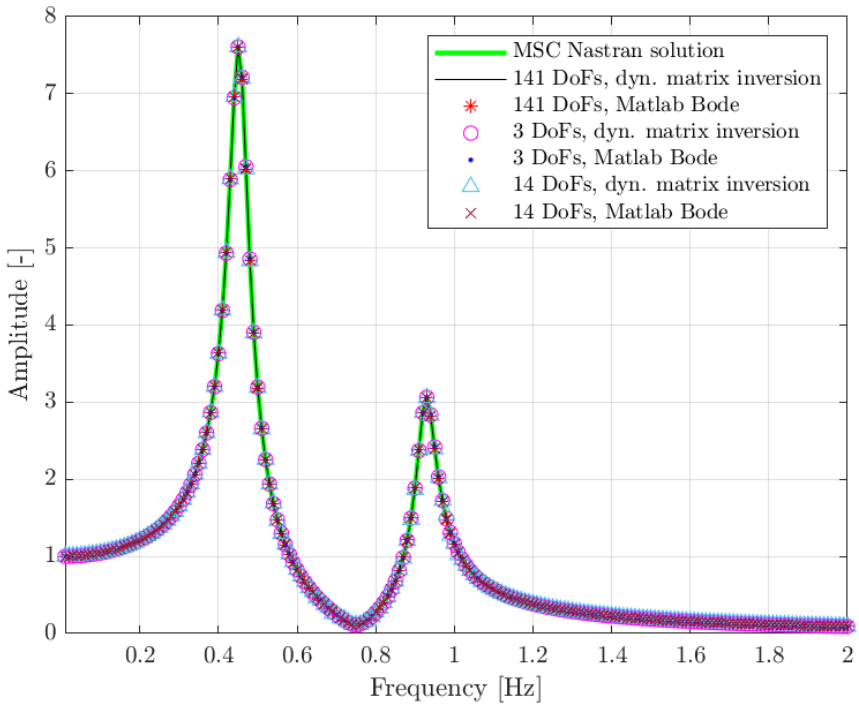

Figure 2.25: $\ddot{u}_{1_z}$, with LM, divided by $\ddot{u}_0$

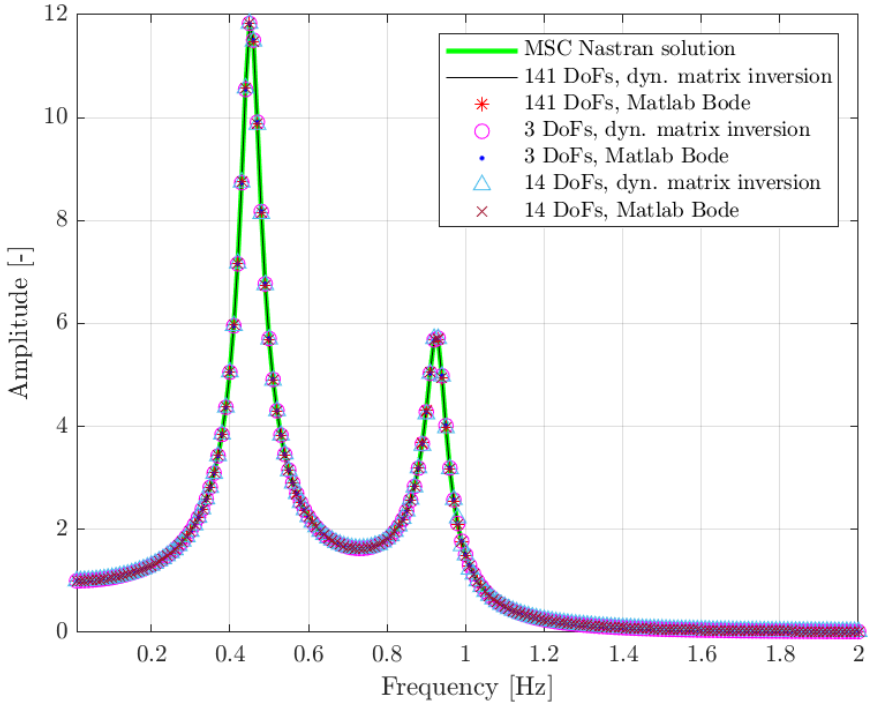

Figure 2.26: $\ddot{u}_{2_z}$, with LM, divided by $\ddot{u}_0$

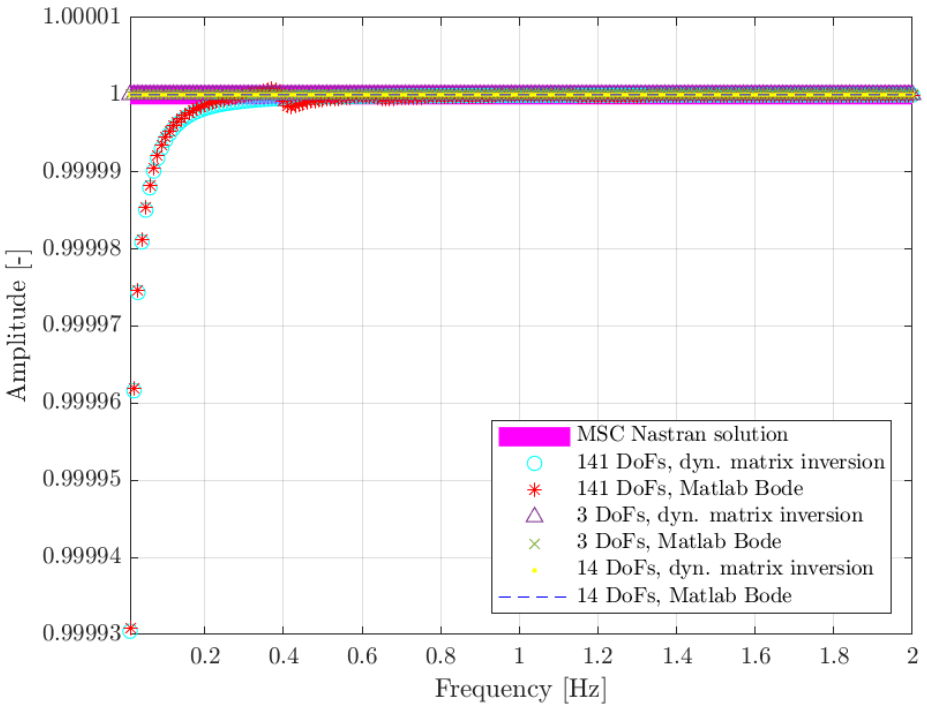

Figure 2.27: $\ddot{u}_{0_z}$, with LM, divided by $\ddot{u}_0$

- With LM method, not dividing by $\ddot{u}_0$:

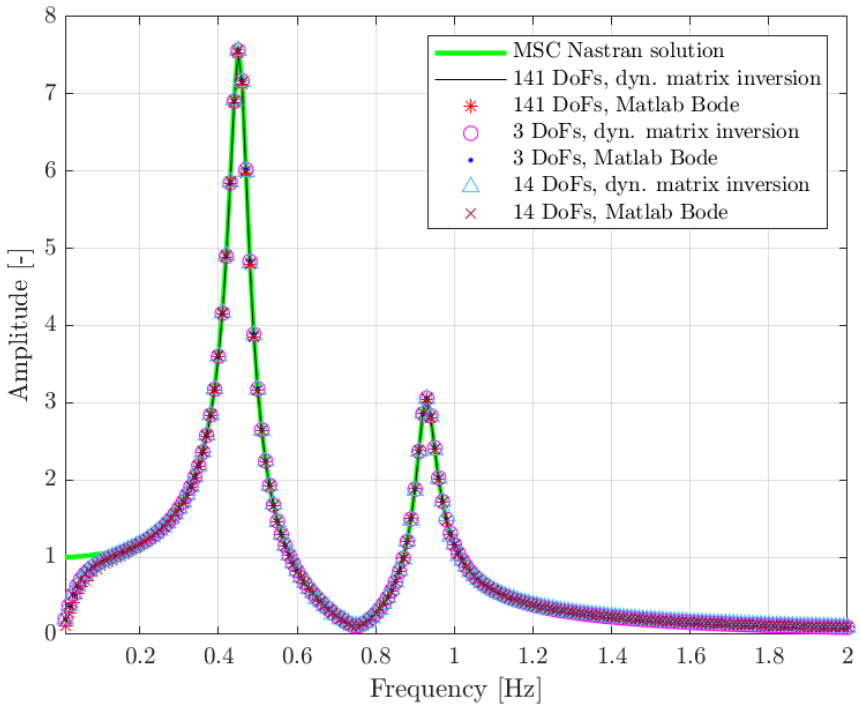

Figure 2.28: $\ddot{u}_{1_z}$, with LM, not divided by $\ddot{u}_0$

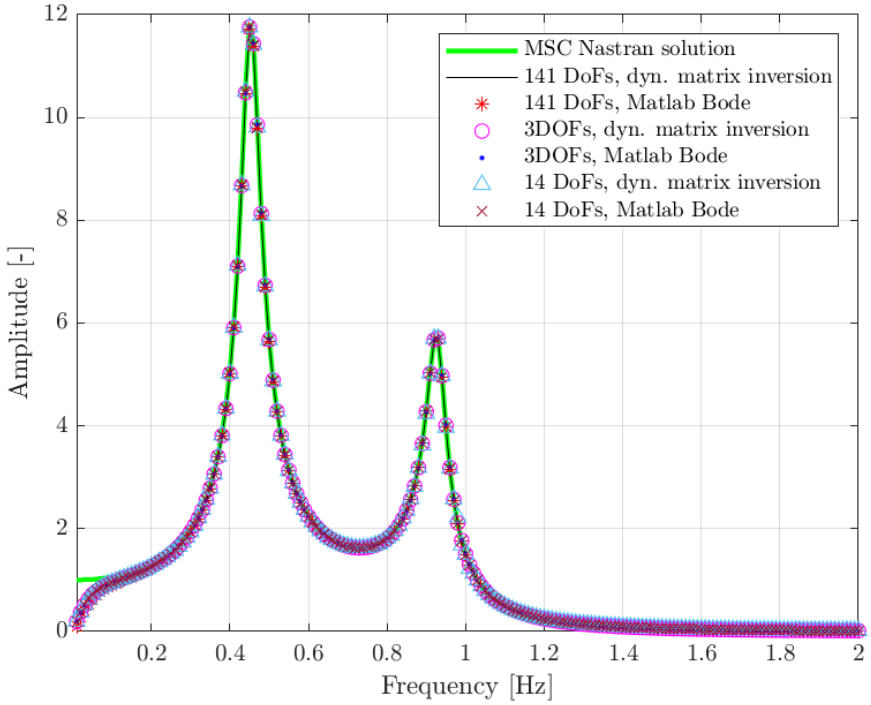

Figure 2.29: $\ddot{u}_{2_z}$, with LM, not divided by $\ddot{u}_0$

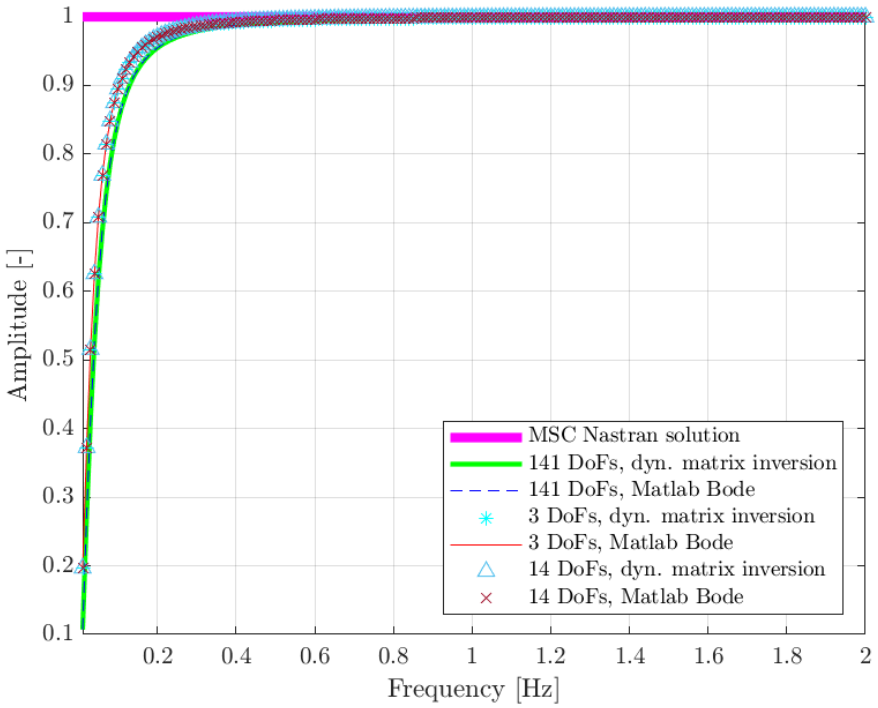

Figure 2.30: $\ddot{u}_{0_z}$, with LM, not divided by $\ddot{u}_0$

- Without LM method, dividing by $\ddot{u}_0$:

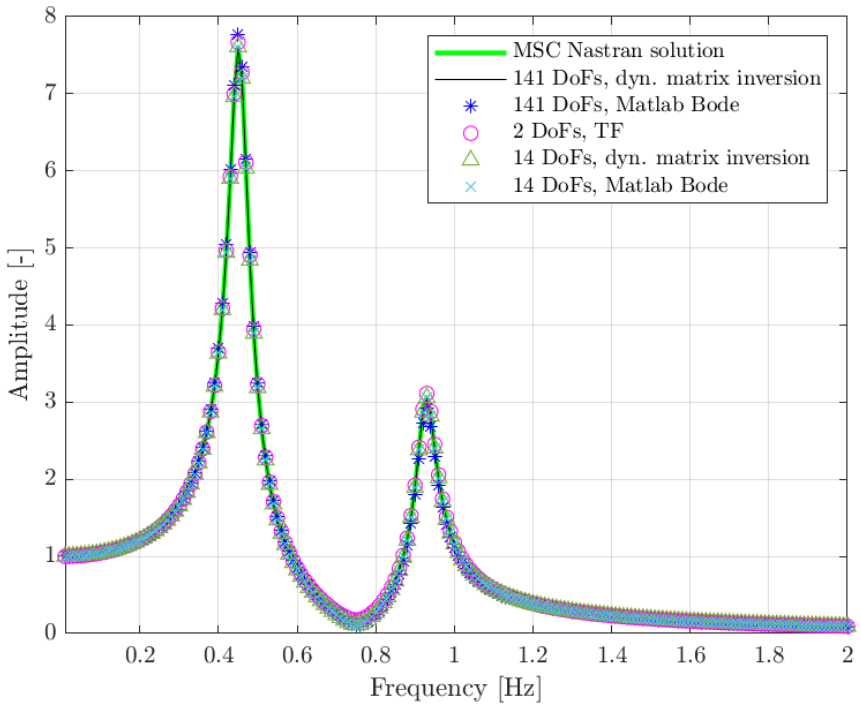

Figure 2.31: $\ddot{u}_{1_z}$, without LM, divided by $\ddot{u}_0$

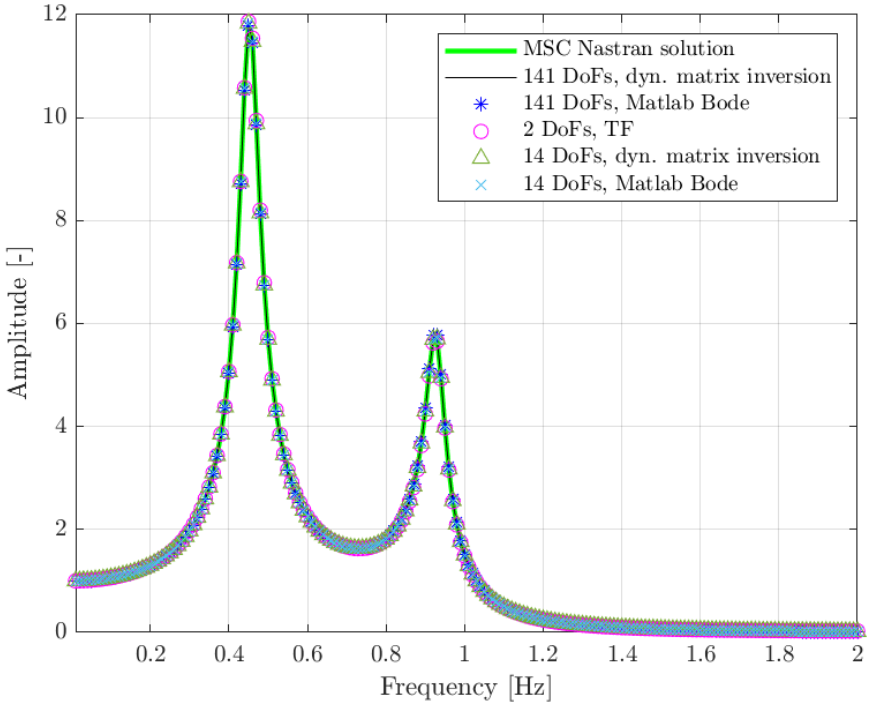

Figure 2.32: $\ddot{u}_{2_z}$, without LM, divided by $\ddot{u}_0$

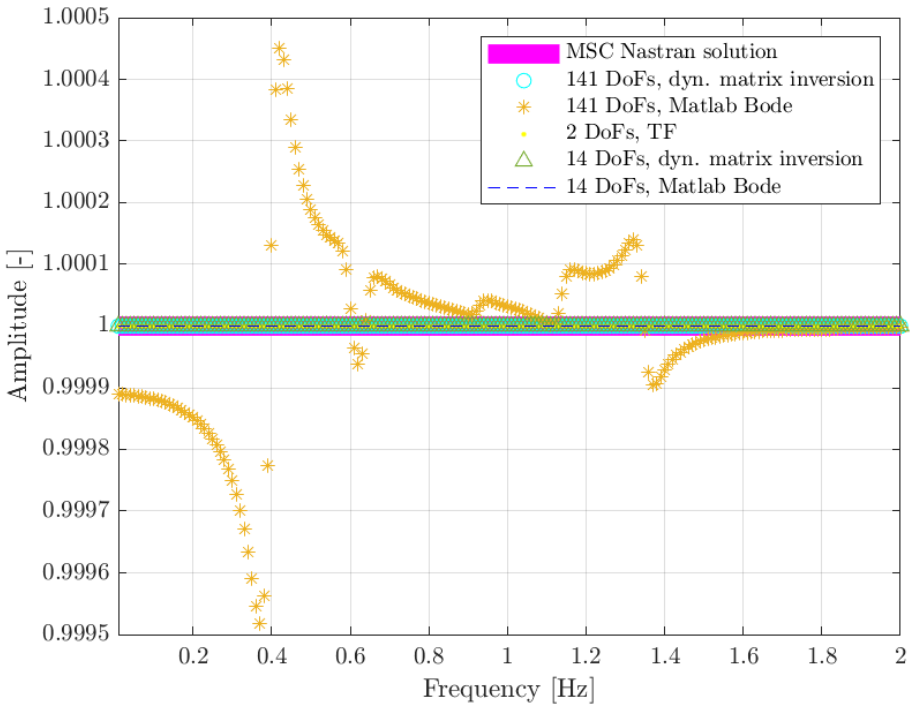

Figure 2.33: $\ddot{u}_{0_z}$, without LM, divided by $\ddot{u}_0$

Eventually, some graphs which collect all the FRF curves with the LM method regarding the acceleration of the VIBISIO, of the MPLAT and of the base have been realized.

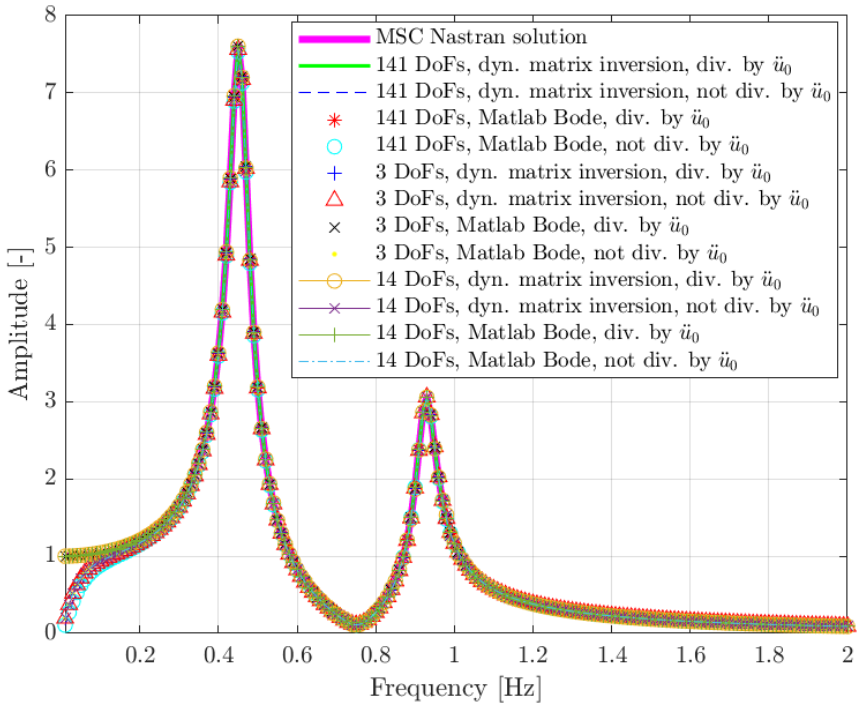

Figure 2.34: $\ddot{u}_{1_z}$, with LM

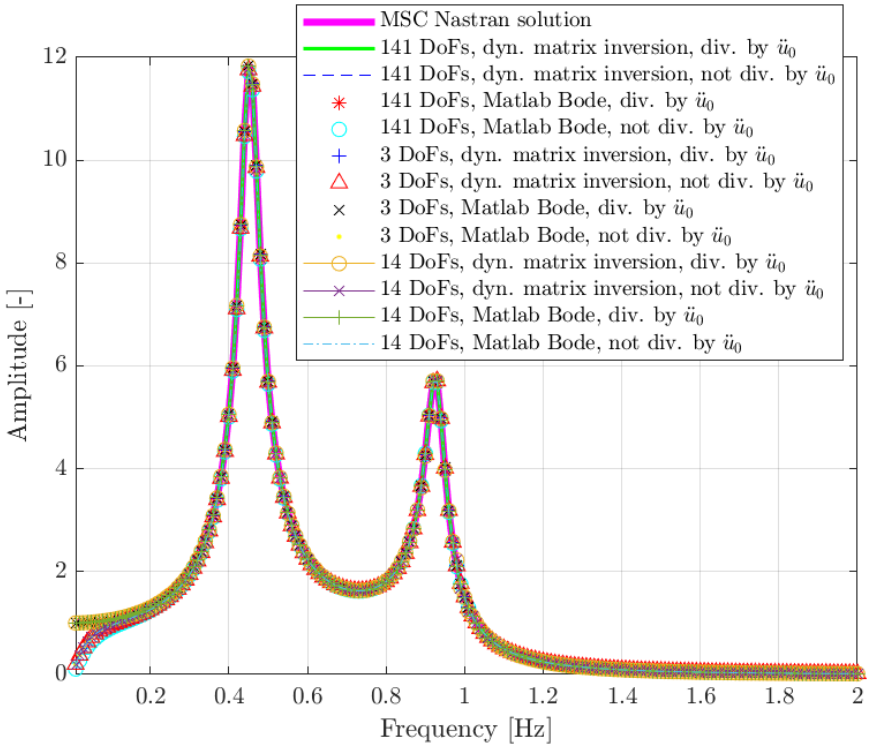

Figure 2.35: $\ddot{u}_{2_z}$, with LM

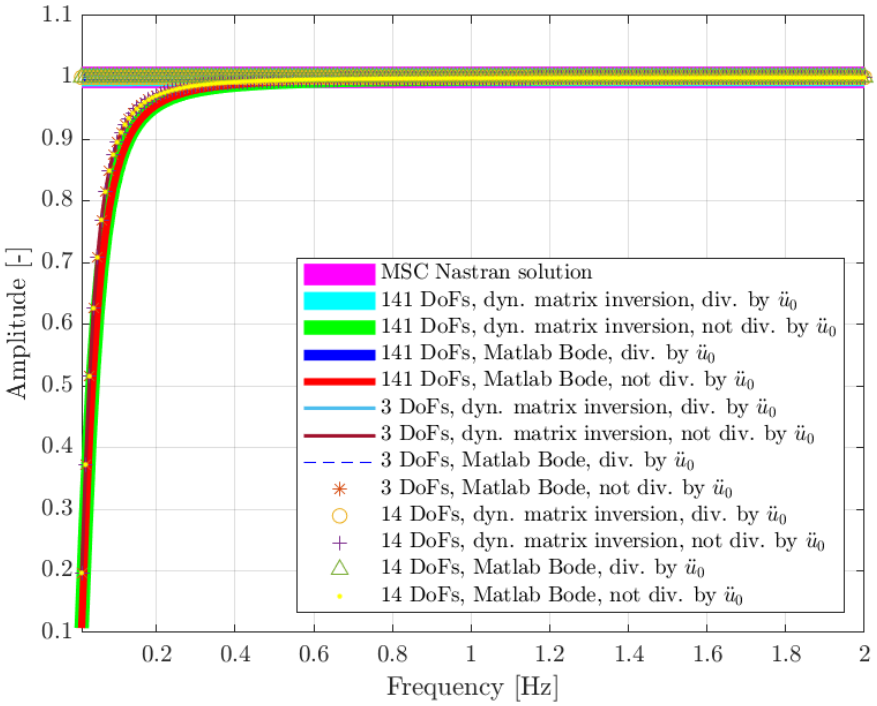

Figure 2.36: $\ddot{u}_{0_z}$, with LM

From all the graphs above, it can be appreciated that the curves overlap precisely in the

entire frequency range, except for the lowest frequencies until roughly 0.2 Hz, when the division by $\ddot{u}_0$ is not present. This phenomenon occurs not only in the curves computed with *bode*, which is particularly sensitive to numerical problems, but also in the ones computed with the dynamics matrix inversion. Such a lack of overlap is due to numerical issues in the computation, but it does not affect the goodness of the work, since the resonance frequencies are present from 0.454 Hz on. However, this particular behaviour at lower frequencies is a topic which should be deepened in the future.

2.5.2. Check Coupled Dynamics

In order to check whether any coupled dynamics are present in the model, it is necessary to impose a longitudinal base excitation and study the frequency responses in the transverse direction. This study can be carried out only on the CB model and not on the 2DoF one, since on the 2DoF the transverse responses do not appear. The following responses compare the cases with and without the LM method (described in section 2.4), and the cases of the response obtained with the dynamics matrix inversion and with the MATLAB® *bode* command. The frequency responses of the three accelerations, $\ddot{u}_1$, $\ddot{u}_2$ and $\ddot{u}_0$, in the three directions, are shown both divided and not divided by $\ddot{u}_0$, except for the case without LM, for which the frequency responses must always be divided by $\ddot{u}_0$.

- First transverse response, divided by $\ddot{u}_0$:

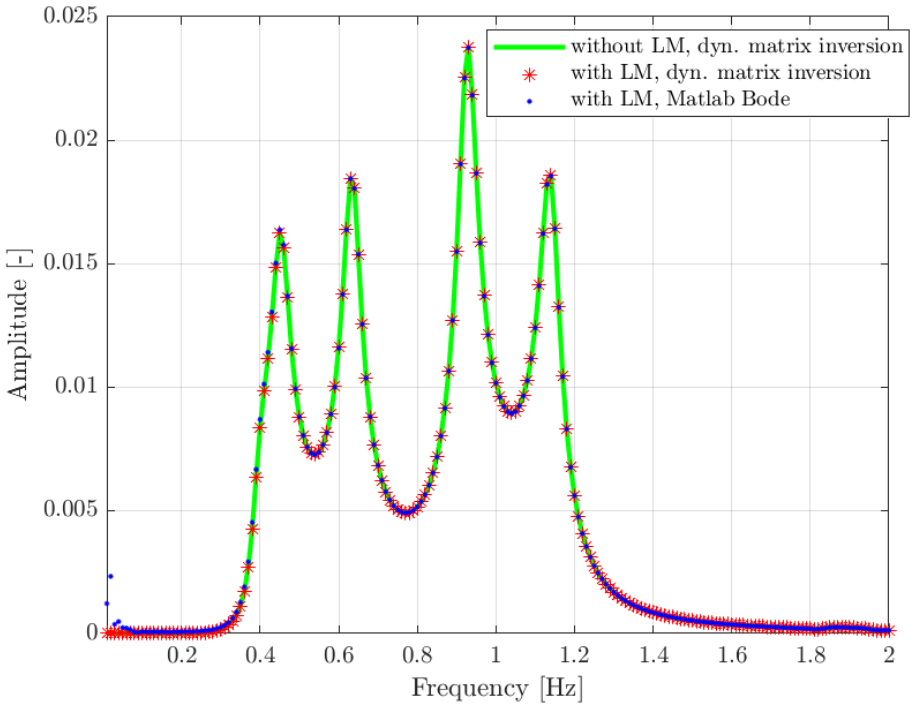

Figure 2.37: $\ddot{u}_{1_x}$, 141 DoFs, divided by $\ddot{u}_0$

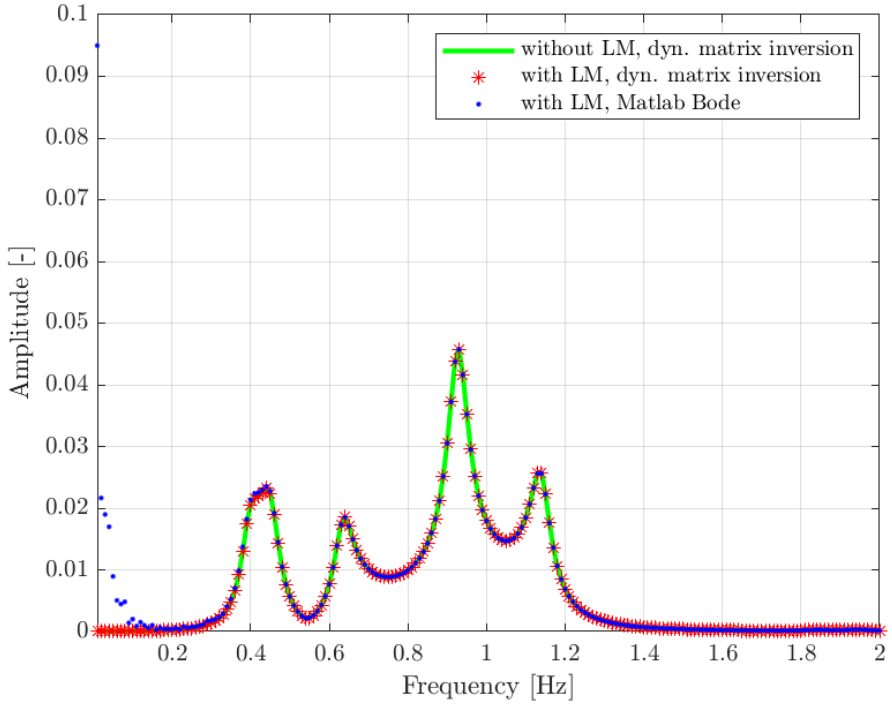

Figure 2.38: $\ddot{u}_{2_x}$, 141 DoFs, divided by $\ddot{u}_0$

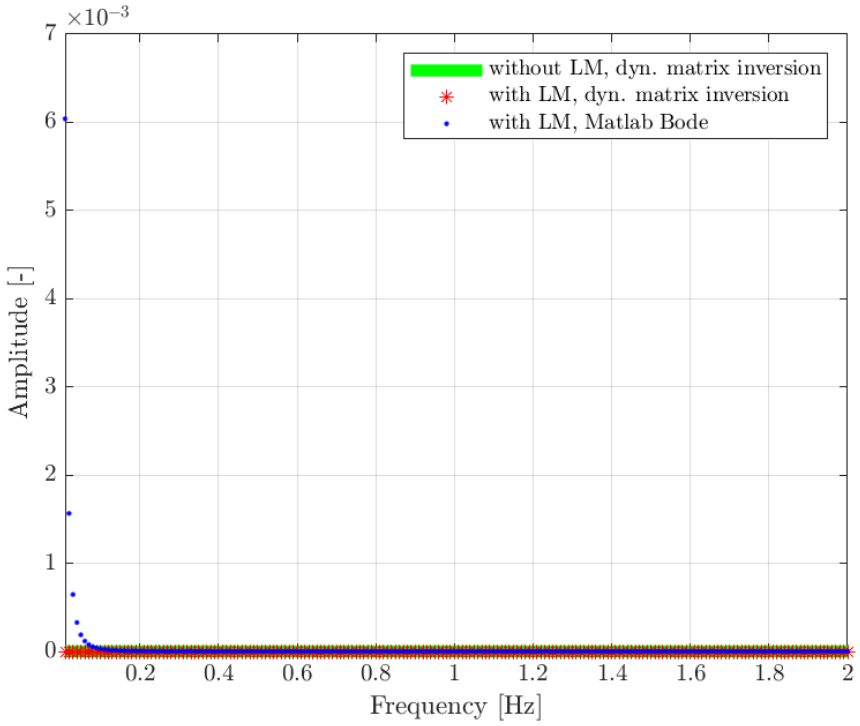

Figure 2.39: $\ddot{u}_{0_x}$, 141 DoFs, divided by $\ddot{u}_0$

- First transverse response, not divided by $\ddot{u}_0$:

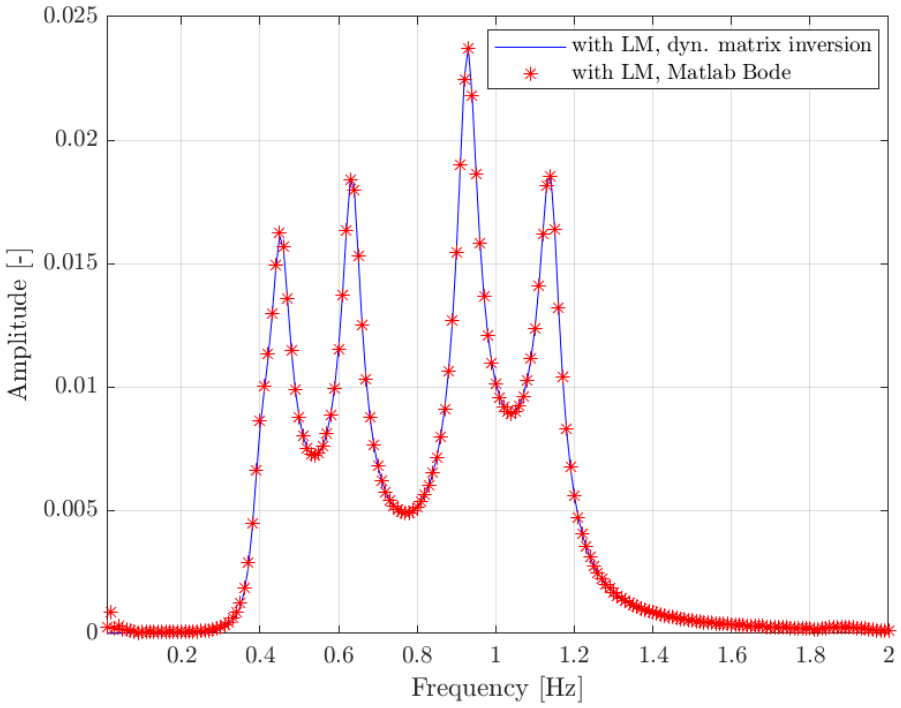

Figure 2.40: $\ddot{u}_{1_x}$, 141 DoFs, not divided by $\ddot{u}_0$

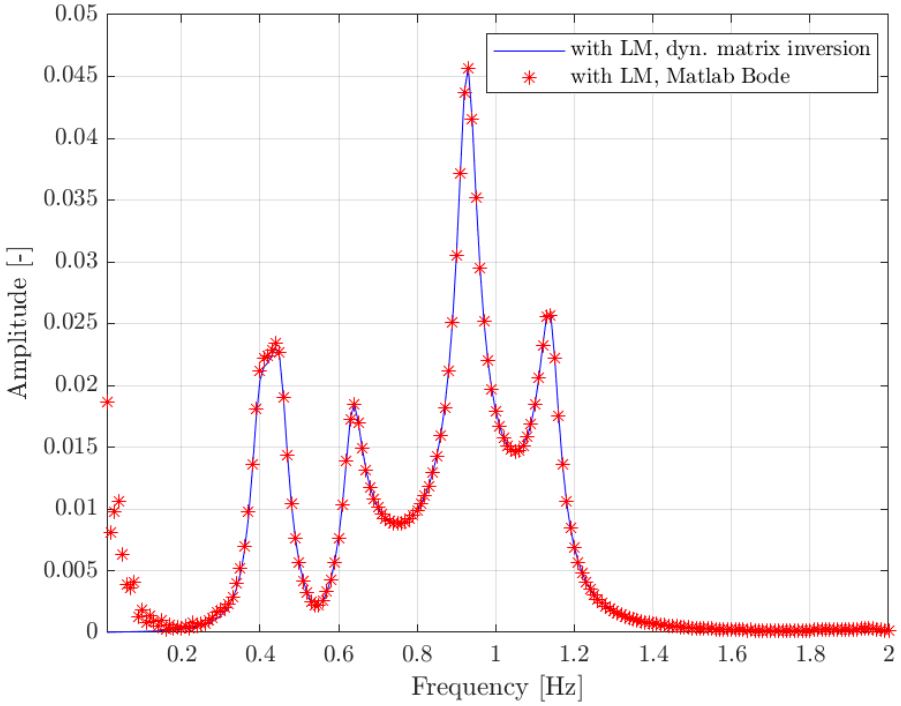

Figure 2.41: $\ddot{u}_{2_x}$, 141 DoFs, not divided by $\ddot{u}_0$

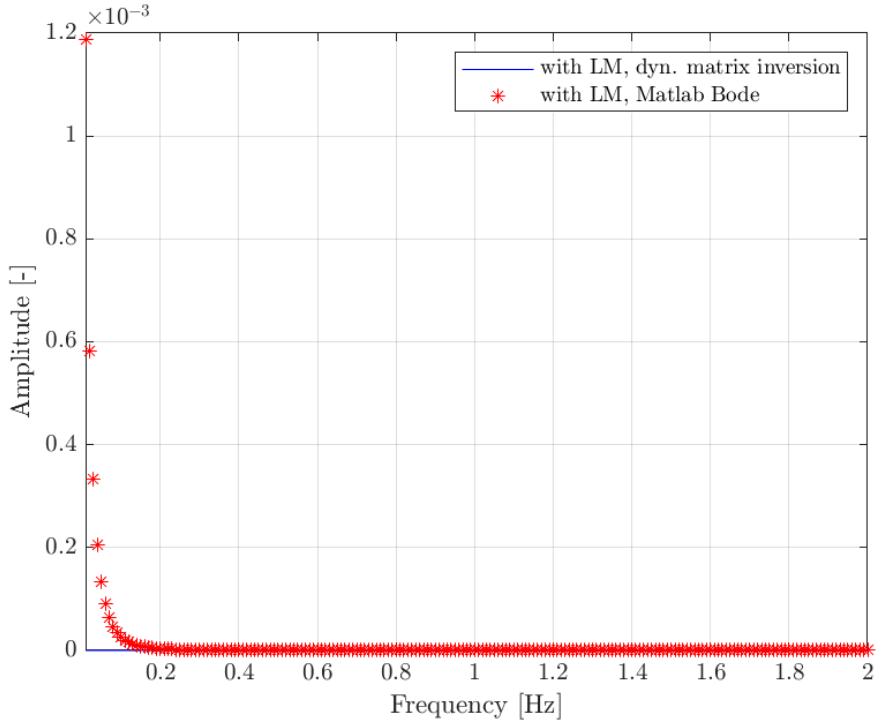

Figure 2.42: $\ddot{u}_{0_x}$, 141 DoFs, not divided by $\ddot{u}_0$

- Second transverse response, divided by $\ddot{u}_0$:

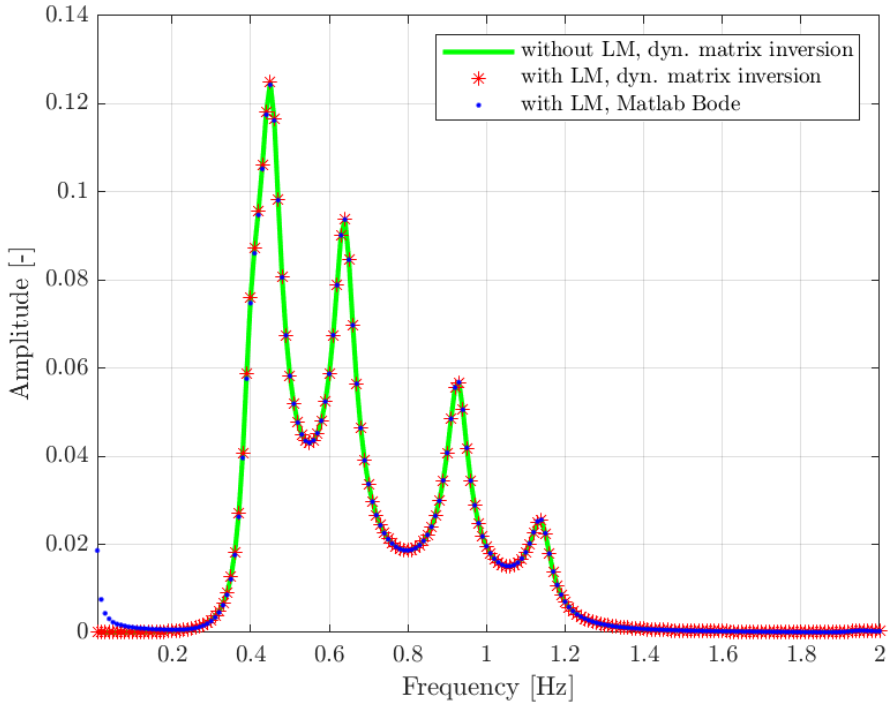

Figure 2.43: $\ddot{u}_{1_y}$, 141 DoFs, divided by $\ddot{u}_0$

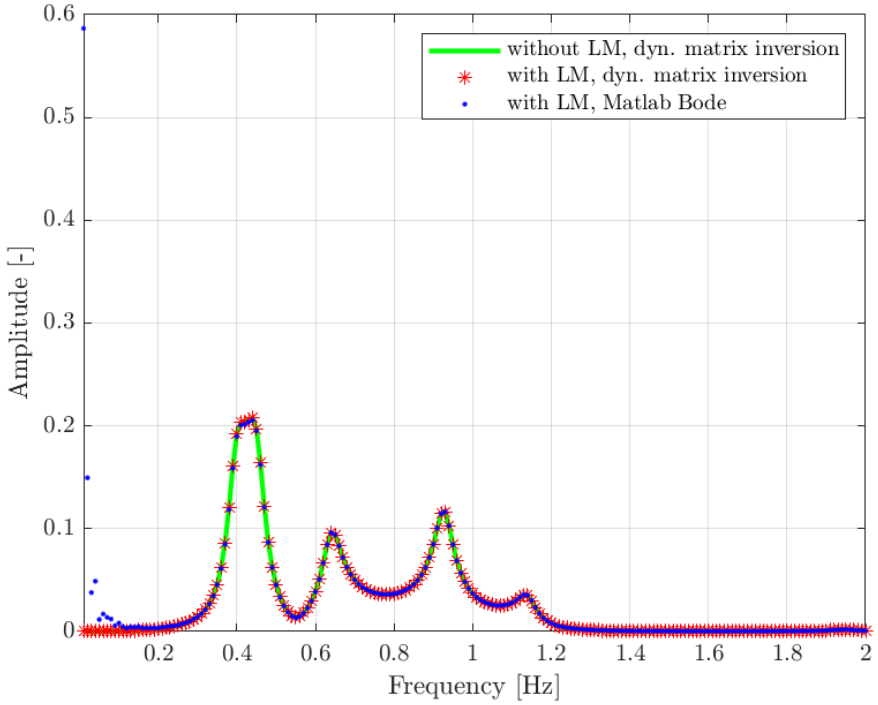

Figure 2.44: $\ddot{u}_{2_y}$, 141 DoFs, divided by $\ddot{u}_0$

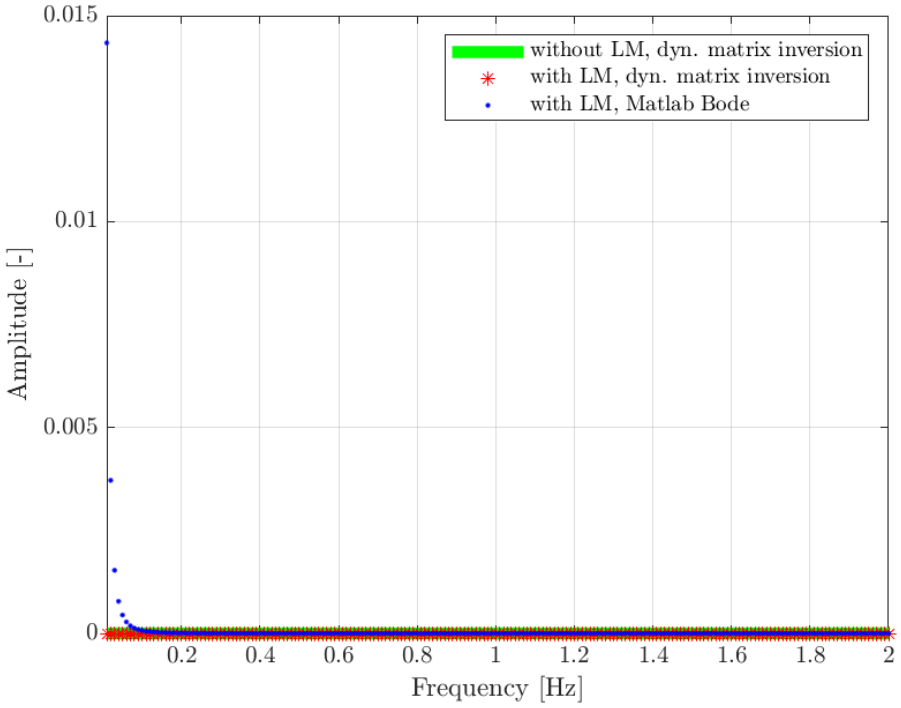

Figure 2.45: $\ddot{u}_{0_y}$, 141 DoFs, divided by $\ddot{u}_0$

- Second transverse response, not divided by $\ddot{u}_0$:

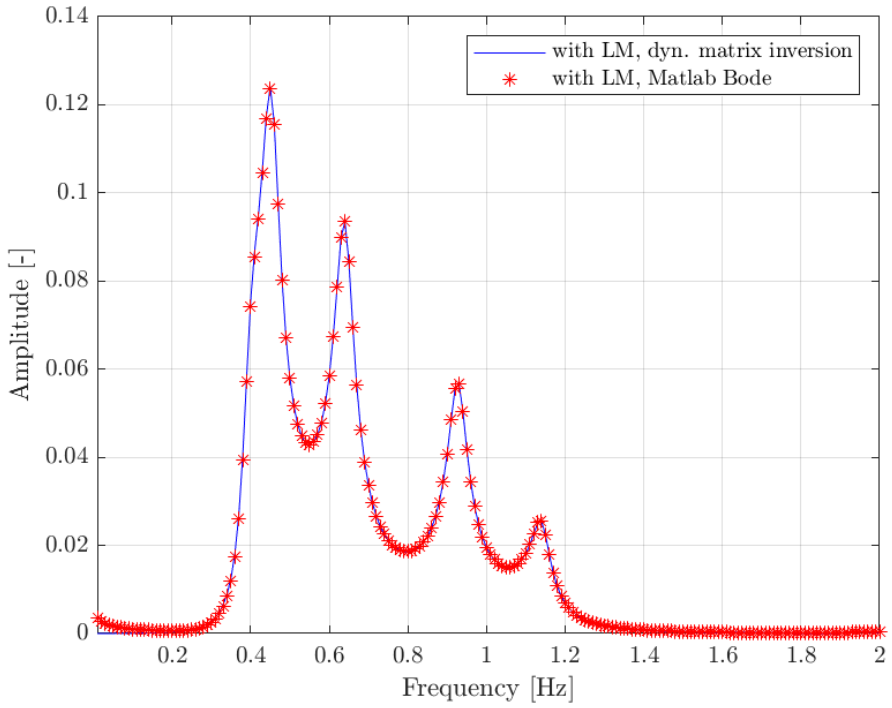

Figure 2.46: $\ddot{u}_{1_y}$, 141 DoFs, not divided by $\ddot{u}_0$

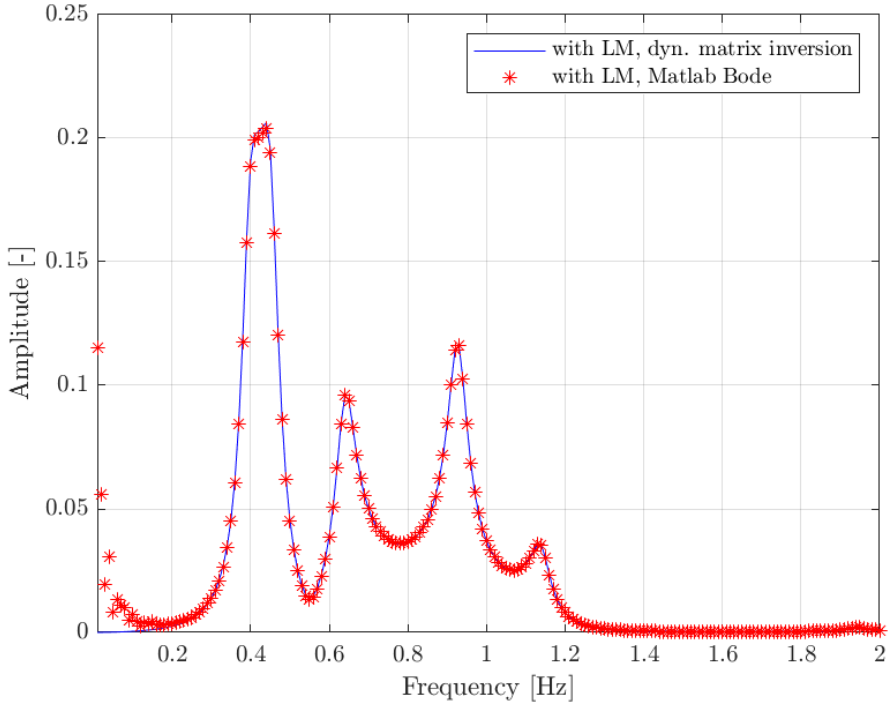

Figure 2.47: $\ddot{u}_{2_y}$, 141 DoFs, not divided by $\ddot{u}_0$

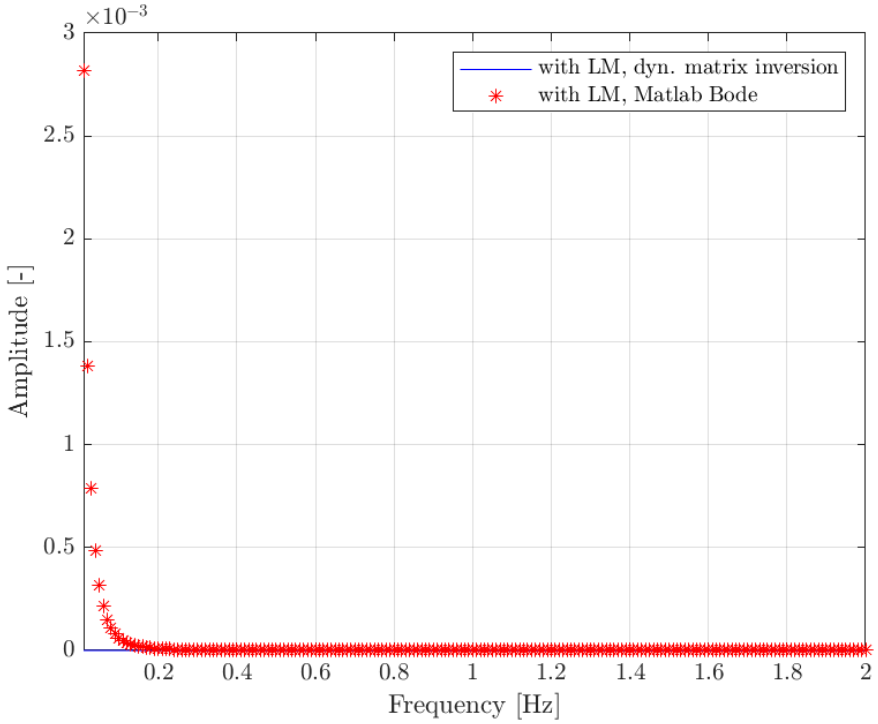

Figure 2.48: $\ddot{u}_{0_y}$, 141 DoFs, not divided by $\ddot{u}_0$

The presence of some peaks in the above FRFs could be attributed to:

- the CoG offset, due to the shape and density of the IUT;
- the fact that the facility is not perfectly symmetric, for example due to the presence of the tilt sensor.

Moreover, from the graphs it emerges that the solution with the *bode* command detaches itself from the other curves at low frequencies. This is due to the fact that *bode* is particularly sensitive to numerical problems. However, the lack of overlap at low frequencies does not affect the quality of the work, since the lower frequencies are not of interest. On the contrary, what is of interest are the resonant frequencies, which are present from 0.454 Hz on.

2.6. Modal Analysis

The modal analysis is performed by considering the effective modal masses.

2.6.1. Modal Effective Mass: Definition

The modal effective mass is a modal dynamic property of a structure associated with the modal characteristics: natural frequencies, mode shapes, generalised masses, and participation factors. It is a measure to classify the importance of a mode shape when a structure is excited by base acceleration (enforced acceleration). A high effective mass will lead to a high reaction force at the base, while mode shapes with low associated modal effective mass are barely excited by base acceleration and will give low reaction forces at the base. The effect of local modes is not well described with modal effective masses. [33]

Consider a modal transient or frequency response function analysis via the finite element method. Also consider that the system is a multi-degree-of-freedom system. For brevity, only a limited number of modes should be included in the analysis. The number should be enough so that the total effective modal mass of the model is at least 90% of the actual mass.

Consider a discrete dynamic system governed by the following equation:

$$\mathbf{M\ddot{u}} + \mathbf{Ku} = \mathbf{F} \tag{2.38}$$

A solution to the homogeneous form of equation (2.38) can be found in terms of eigenvalues and eigenvectors. The eigenvectors represent normal modes.

Let $\boldsymbol{\phi}$ be the eigenvector matrix. The system's generalized mass matrix $\hat{\mathbf{M}}$ is given by:

$$\hat{\mathbf{M}} = \boldsymbol{\phi}^T \mathbf{M} \boldsymbol{\phi} \tag{2.39}$$

Let $\mathbf{r}$ be the influence vector which represents the displacements of the masses resulting from static application of a unit ground displacement. The influence vector induces a rigid body motion in all modes.

Define a coefficient vector $\mathbf{L}$ as:

$$\mathbf{L} = \boldsymbol{\phi}^T \mathbf{M} \mathbf{r} \tag{2.40}$$

The modal participation factor for mode i, Γ_i, is:

$$\Gamma_i = \frac{L_i}{\hat{M}_{ii}} \tag{2.41}$$

The effective modal mass for mode i, $m_{eff,i}$, is:

$$m_{eff,i} = \frac{{L_i}^2}{\hat{M}_{ii}} \tag{2.42}$$

Note that $\hat{M}_{ii}$= 1 for each index if the eigenvectors have been normalized with respect to the mass matrix. Furthermore, the off-diagonal modal mass terms ($\hat{M}_{ij}$, $i \neq j$) are zero regardless of the normalization and even if the physical mass matrix **M** has distributed mass. This is due to the orthogonality of the eigenvectors. However, the off-diagonal modal mass terms do not appear in equation (2.42). [18]

2.6.2. Modal Effective Masses: Computation

The effective modal masses have been computed by means of MSC Nastran™ both for the full FEM model and for the CB one. Table 2.2 and table 2.3 show the modes, the modal frequencies and the modal masses for the three translations and for the three rotations. The largest values of the modal masses are highlighted in red.
The effective modal masses of the full FEM model are:

Table 2.2: Effective modal masses of the full FEM model

Mode	**Frequency [Hz]**	T_1 **[kg]**	T_2 **[kg]**	T_3 **[kg]**	R_1 $[kg \cdot m]$	R_2 $[kg \cdot m]$	R_3 $[kg \cdot m]$
1	0.396	4.49E-01	1.10E-02	8.12E-06	2.01E-02	8.17E-01	2.10E-04
2	0.397	1.11E-02	4.53E-01	1.29E-04	8.18E-01	2.01E-02	2.56E-05
3	0.454	2.32E-06	1.91E-04	6.25E-01	1.66E-04	2.94E-06	6.66E-11
4	0.601	1.13E-03	2.36E-04	3.15E-08	2.45E-05	2.64E-04	7.53E-01
5	0.637	1.86E-01	5.64E-03	8.56E-06	3.14E-04	1.01E-02	1.91E-03
6	0.640	5.38E-03	1.82E-01	6.14E-05	9.54E-03	2.70E-04	1.10E-03
7	0.928	1.91E-06	1.44E-05	2.93E-02	2.93E-06	1.23E-06	1.82E-10
8	1.139	2.42E-03	2.23E-04	3.04E-07	2.68E-03	2.81E-02	4.72E-05
9	1.141	2.29E-04	2.35E-03	2.54E-06	2.82E-02	2.65E-03	1.97E-07
10	1.347	8.33E-07	9.52E-09	5.28E-11	8.67E-07	1.19E-05	1.08E-02

The effective modal masses of the CB model are:

Table 2.3: Effective modal masses of the CB model

Mode	Frequency [Hz]	T_1 [kg]	T_2 [kg]	T_3 [kg]	R_1 $[kg \cdot m]$	R_2 $[kg \cdot m]$	R_3 $[kg \cdot m]$
1	0.396	4.52E-01	7.46E-03	7.30E-06	1.36E-02	8.24E-01	2.10E-04
2	0.397	7.54E-03	4.56E-01	1.30E-04	8.24E-01	1.36E-02	2.15E-05
3	0.454	2.87E-06	1.90E-04	6.25E-01	1.65E-04	3.46E-06	6.92E-11
4	0.601	1.12E-03	2.36E-04	2.85E-08	2.60E-05	2.58E-04	7.52E-01
5	0.637	1.86E-01	5.40E-03	8.63E-06	3.04E-04	1.02E-02	1.89E-03
6	0.640	5.14E-03	1.83E-01	6.09E-05	9.59E-03	2.57E-04	1.06E-03
7	0.928	1.92E-06	1.44E-05	2.93E-02	2.96E-06	1.17E-06	1.49E-10
8	1.139	2.43E-03	2.19E-04	3.15E-07	2.64E-03	2.82E-02	4.64E-05
9	1.141	2.26E-04	2.35E-03	2.56E-06	2.82E-02	2.61E-03	1.82E-07
10	1.347	8.82E-07	1.13E-08	5.61E-11	8.85E-07	1.20E-05	1.08E-02

The effective modal masses from the 11^{th} mode on, both for the full FEM model and for the CB one, are represented in Appendix B.
Both in the full FEM model and in the CB model, the largest effective modal masses belong to the first 6 modes. It is interesting to represent them in a histogram to highlight the entity of the modal participation factor both in the three translations and in the three rotations. Figure 2.49 shows the effective modal masses of the full FEM model and of the CB one. The largest values of the modal effective masses are displayed.

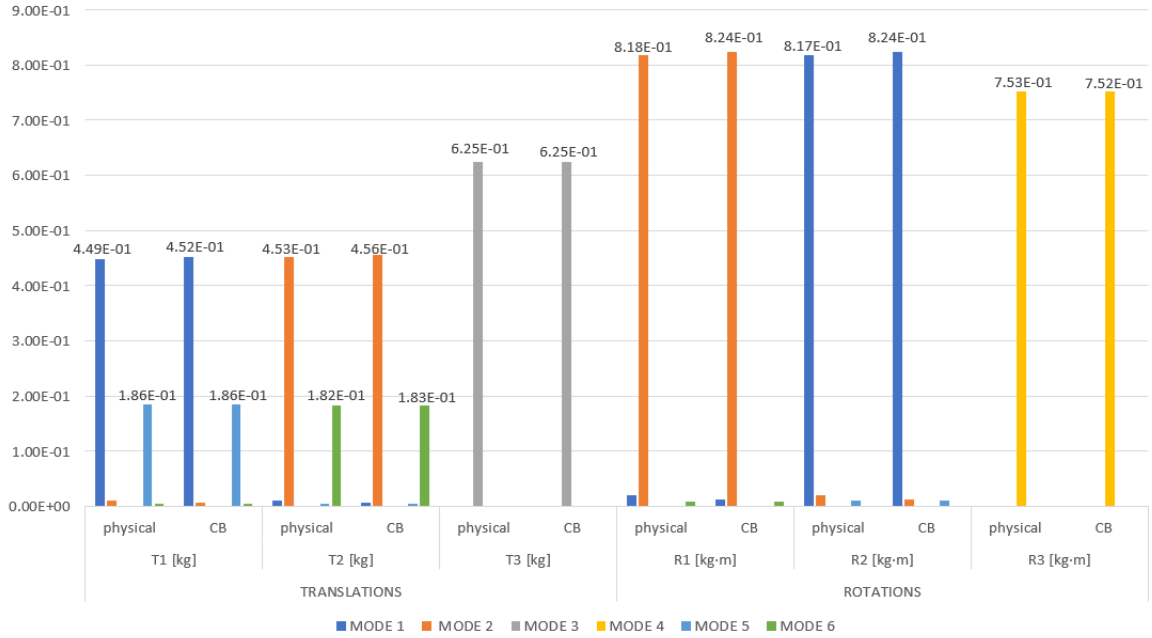

Figure 2.49: Modal effective masses of the full FEM model and of the CB model

From fig. 2.49 it can be noted that the values of the corresponding modal effective masses in the full FEM model and in the CB one are close to each other. In fig. 2.50 are displayed the mode numbers against the modal frequencies.

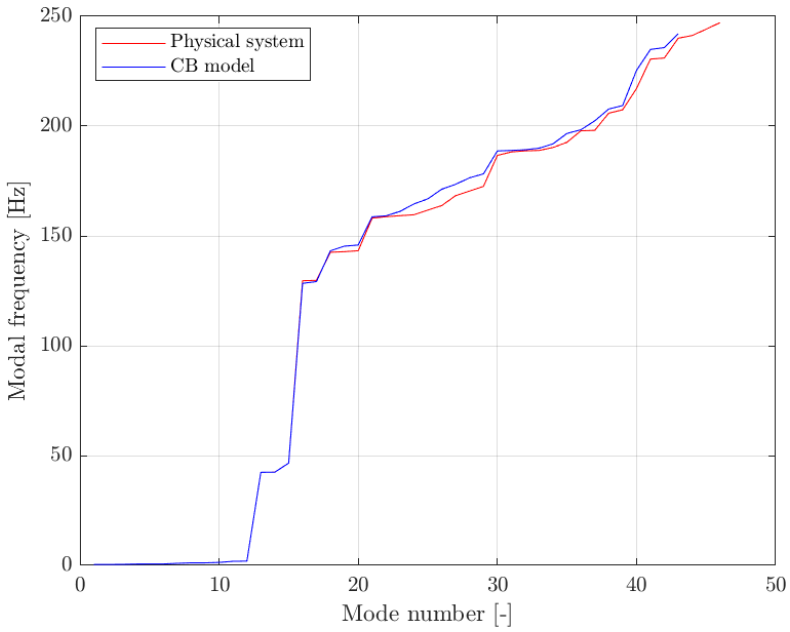

Figure 2.50: Modal Frequencies

It can be highlighted that, starting from mode 16, mode number and modal frequency start not to perfectly coincide anymore.
The next figures show the effective modal mass corresponding to every frequency until 250 Hz, both for the full FEM model and for the CB model, for the three translations and for the three rotations.

- The effective modal masses associated to the translational modes in the three directions are represented in fig. 2.51, fig. 2.52 and fig. 2.53.

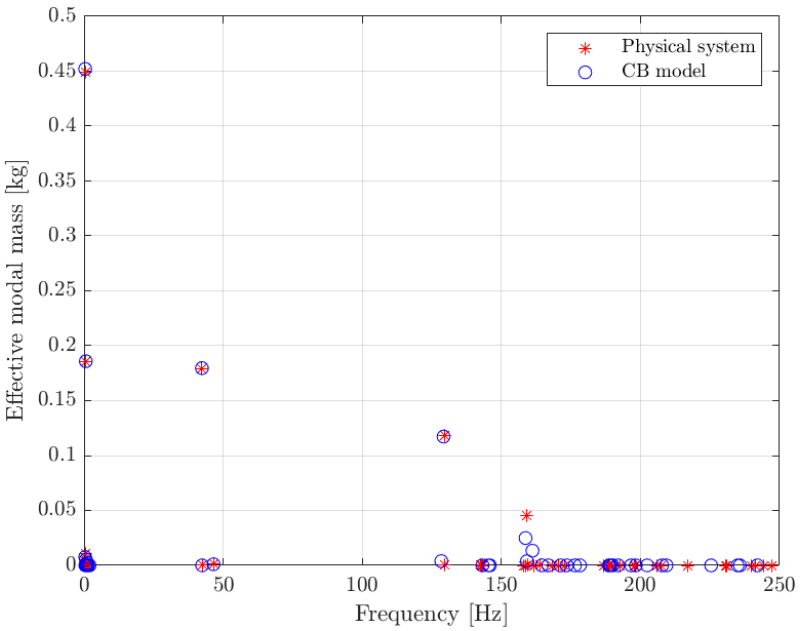

Figure 2.51: T_1

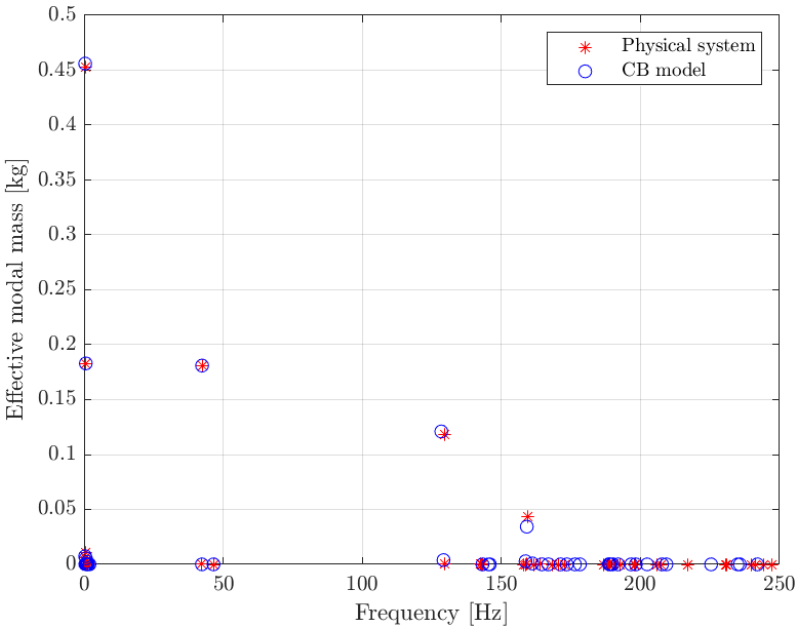

Figure 2.52: T_2

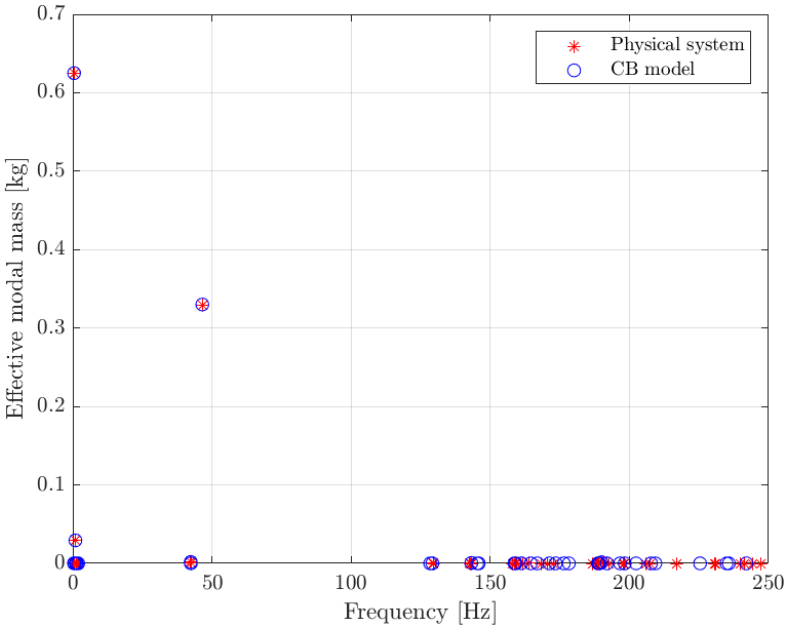

Figure 2.53: T_3

- The effective modal masses associated to the rotational modes around the three axes are represented in fig. 2.54, fig. 2.55 and fig. 2.56.

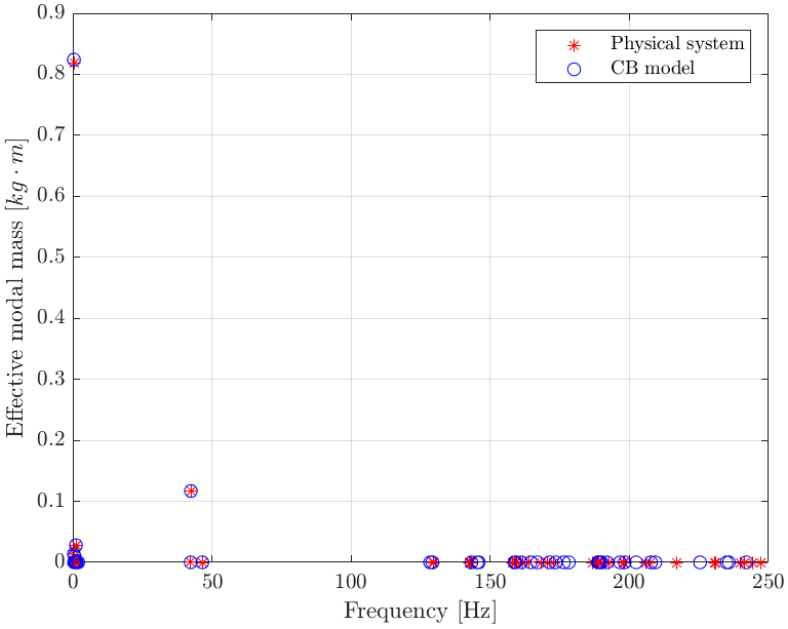

Figure 2.54: R_1

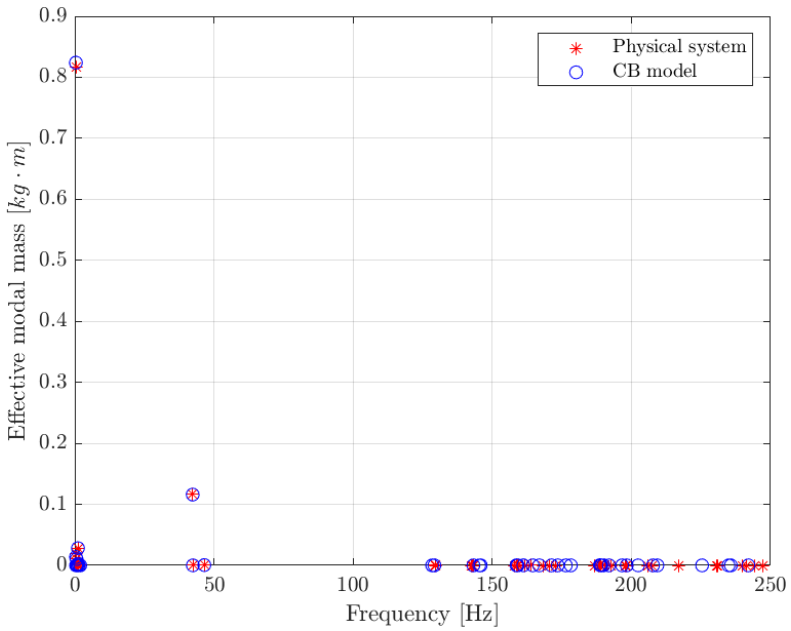

Figure 2.55: R_2

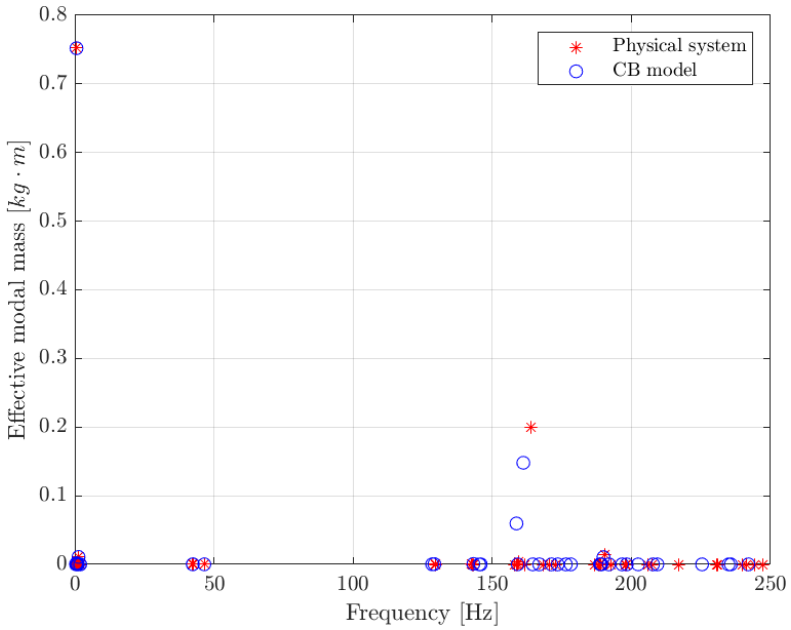

Figure 2.56: R_3

From the above figures it can be noted that at low frequencies the correspondence between effective modal masses of the full FEM model and of the CB model is utterly precise. However, as for the correspondence between mode numbers and modal frequencies, the more the frequency increases, the merrier the effective modal masses start to be different between the full FEM model and the CB one.

2.6.3. Normal Modes

As it can be appreciated from the frequency response functions present in section 2.5.1, the two main vertical normal modes are at frequencies 0.453484 Hz and 0.927579 Hz. They respectively represent the 4^{th} and the 8^{th} normal modes, which are graphically displayed in the following.

- **Mode 4**: $f_4 = 0.453$ Hz

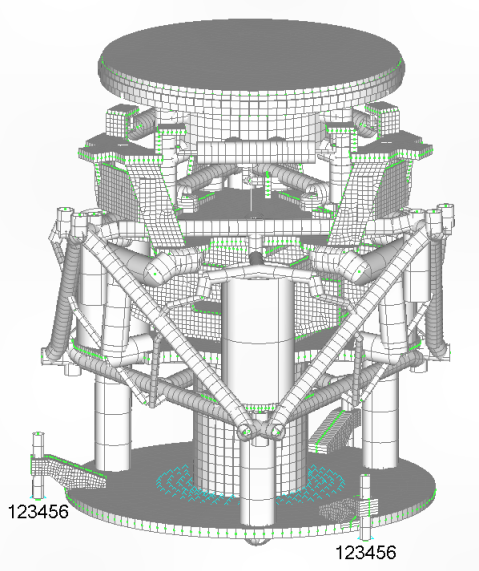

Figure 2.57: Undeformed structure (*Image courtesy of ESA*)

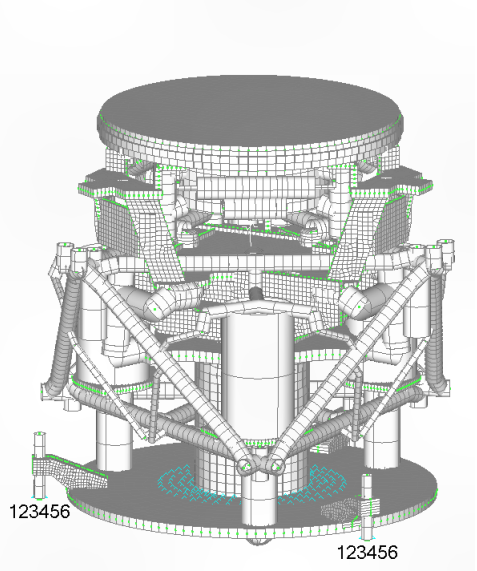

Figure 2.58: Mode 4 (*Image courtesy of ESA*)

- **Mode 8**: $f_8 = 0.928$ Hz

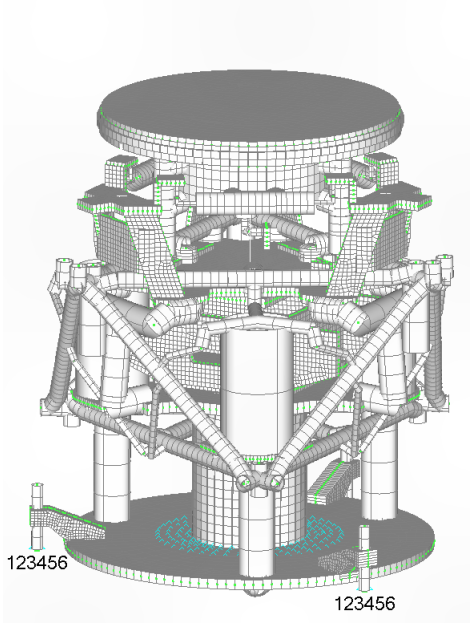

Figure 2.59: Undeformed structure (*Image courtesy of ESA*)

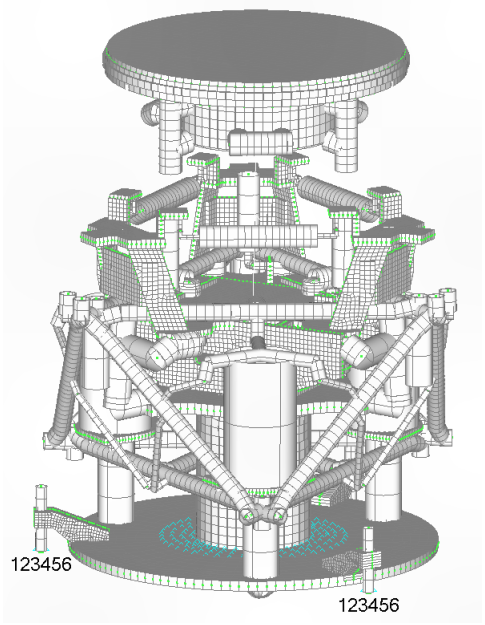

Figure 2.60: Mode 8 (*Image courtesy of ESA*)

On the other hand, the main transverse normal modes correspond to the following frequencies and can thus be represented.

- **Mode 2**: $f_2 = 0.450$ Hz

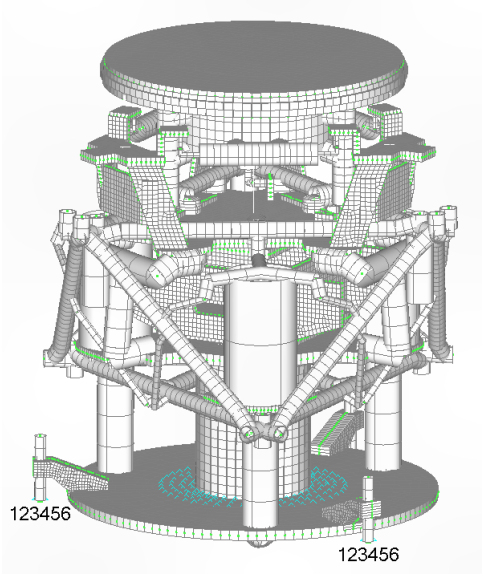

Figure 2.61: Undeformed structure (*Image courtesy of ESA*)

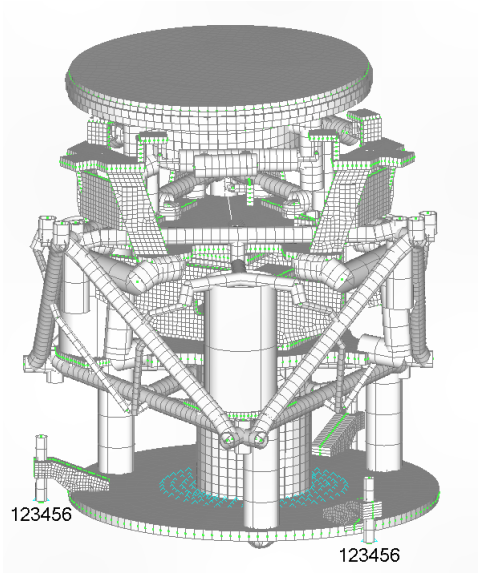

Figure 2.62: Mode 2 (*Image courtesy of ESA*)

- **Mode 3**: $f_3 = 0.450$ Hz

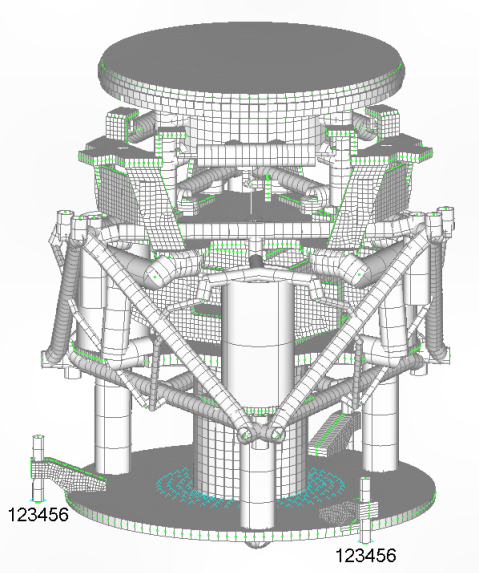

Figure 2.63: Undeformed structure (*Image courtesy of ESA*)

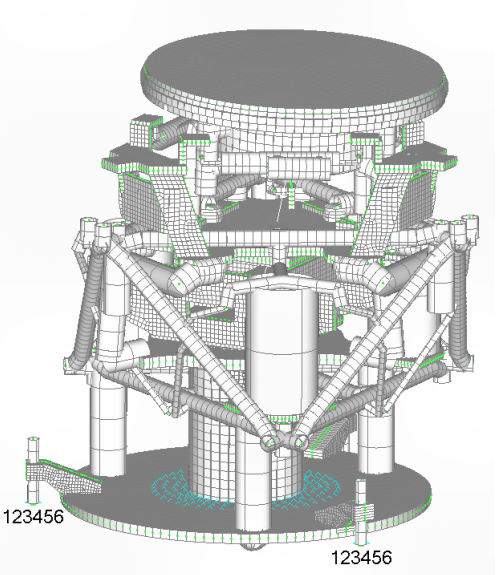

Figure 2.64: Mode 3 (*Image courtesy of ESA*)

- **Mode 5**: $f_5 = 0.639$ Hz

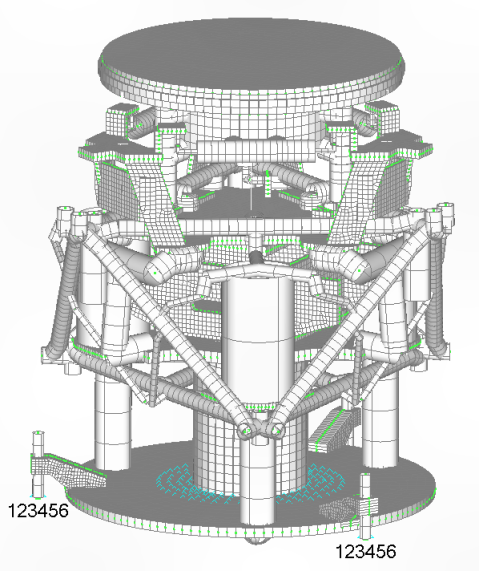

Figure 2.65: Undeformed structure (*Image courtesy of ESA*)

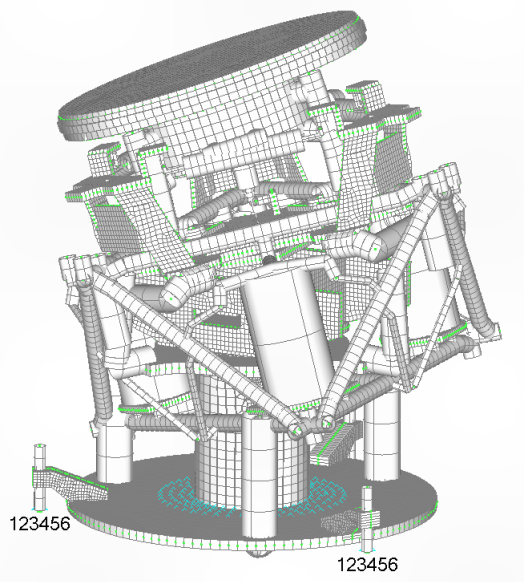

Figure 2.66: Mode 5 (*Image courtesy of ESA*)

- **Mode 6**: $f_6 = 0.645$ Hz

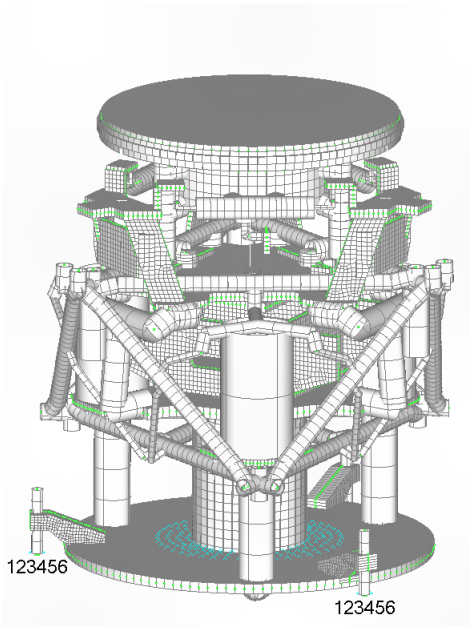

Figure 2.67: Undeformed structure (*Image courtesy of ESA*)

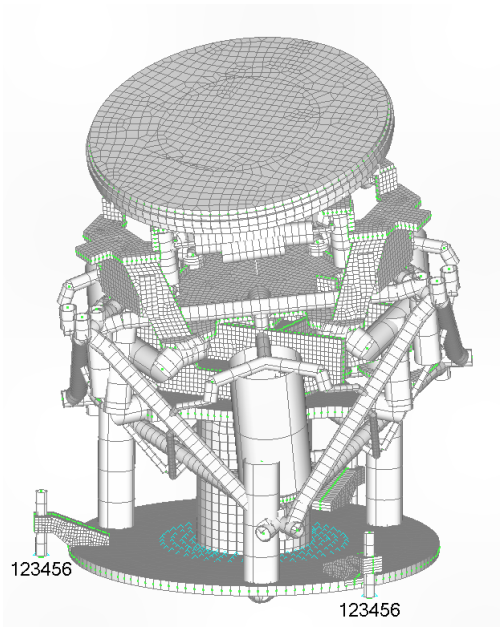

Figure 2.68: Mode 6 (*Image courtesy of ESA*)

- **Mode 7**: $f_7 = 0.682$ Hz

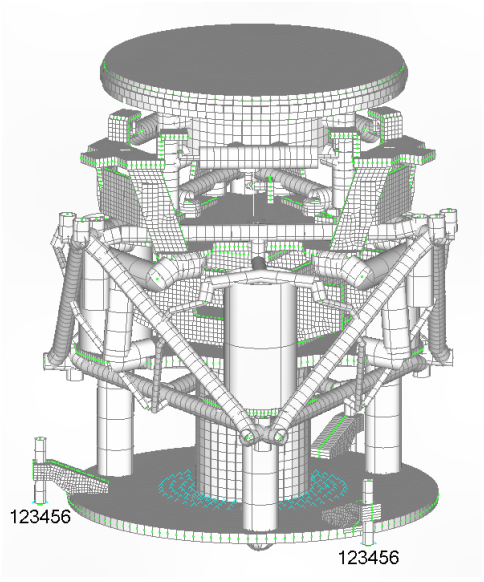

Figure 2.69: Undeformed structure (*Image courtesy of ESA*)

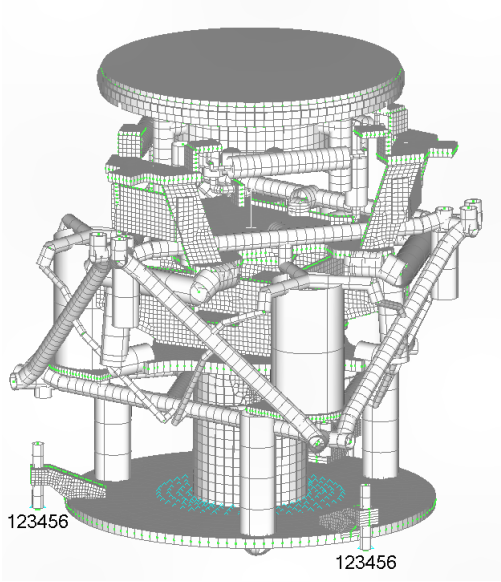

Figure 2.70: Mode 7 (*Image courtesy of ESA*)

- **Mode 9**: $f_9 = 0.055$ Hz

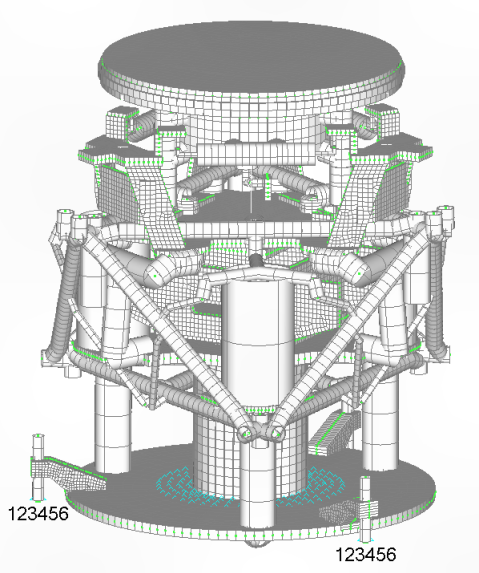

Figure 2.71: Undeformed structure (*Image courtesy of ESA*)

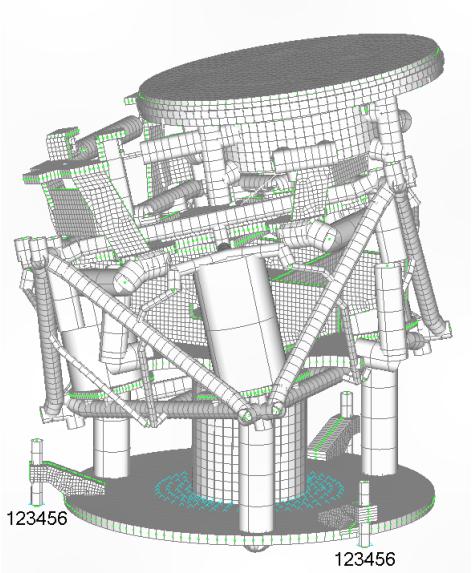

Figure 2.72: Mode 9 (*Image courtesy of ESA*)

- **Mode 10**: $f_{10} = 0.058$ Hz

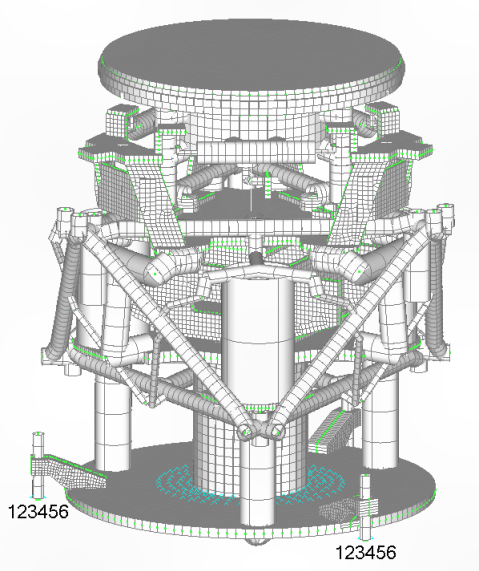

Figure 2.73: Undeformed structure (*Image courtesy of ESA*)

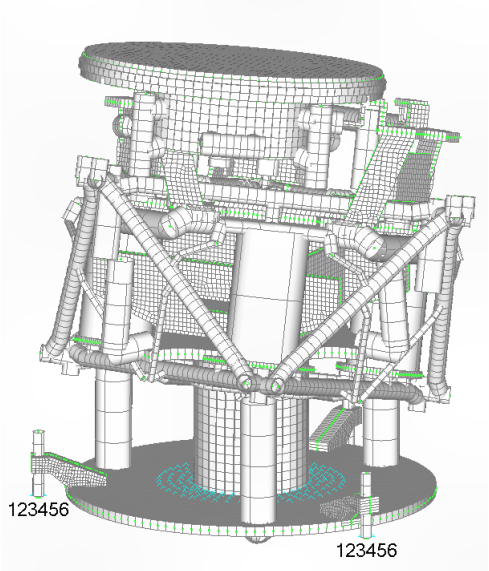

Figure 2.74: Mode 10 (*Image courtesy of ESA*)

3 | Control Design

Two controllers have to be modelled: one on the VIBISIO and one on the MPLAT. Since the equivalent 2DoF model has been validated, it is possible to design the control system on this model, and afterwards extend it to the condensed CB model.

3.1. Isolation Platform Control

The only performance requirement which has been provided is the request of attenuating the resonance peaks of $-20\ dB$. The controller of the VIBISO is intended to isolating the IUT from ground vibrations in 6 DoFs by combining a passive vibration isolation system with active control.

A typical negative-stiffness **passive isolator** gives good isolation at high-frequencies ($>$ 10 Hz), but amplifies vibration at its resonant frequency (usually between 0.1 Hz and 1 Hz) and offers no attenuation below this point.

Inertial sensors placed on the passive isolation platform can be used to measure platform vibration and drive **FB control**, which can be delivered by voice coil force actuators onto the platform. FB control will act to lock the platform to an inertial reference frame, and so attenuate the resonance of the passive isolation platform and improve its low-frequency performance. The purpose of the FB control is to lock the isolation platform to an inertial reference frame defined by the inertial mass of the platform seismometers. The FB control is a velocity control, which acts to smooth the passive platform resonance. The three tri-axial seismometers on the platform are sufficient to measure 6DoF motion and so 6DoF FB control is possible.

Adding an inertial sensor to the ground can be used to drive **FF control**. By measuring ground vibration and predicting the force this vibration will exert on the platform, actuators can be driven to counteract this force. FF control will act to attenuate all platform vibration caused by ground vibration. The FF control minimises isolation platform vibration by measuring ground vibration and then applying a force on the platform which opposes the force exerted on the platform by the ground vibration. In order for this control to be effective, the force caused by ground vibration must be estimated. If

the platform can be approximated as a simple damped mass-spring system, the equivalent force, F_g, exerted on the platform by ground vibration, q_g, is:

$$F_g = K_i q_g + C_i \dot{q}_g \tag{3.1}$$

Where K_i and C_i are the effective spring stiffness and dampening of the platform respectively. These parameters are estimated in an automated procedure by actively stimulating the platform, measuring the response and using standard system identification techniques. The attenuation resulting from FF control is only limited by inaccuracies in estimating the force on the platform and exerting an opposing force.

Isolation Platform Sensors

The VIBISO uses four tri-axial Guralp CMG-3T seismometers as inertial sensors to drive the control algorithm. Each seismometer operates in velocity mode and has its own controller interface which outputs sensor data and allows mass centring. The parameters of the seismometer are summarised in table 3.1.

Table 3.1: Seismometer specification summary

Parameter	**Value**
Sensitivity	2000 Vs/m
Bandwidth	0.0027 Hz to 50 Hz
Mass	13.5 kg
Height	34.4 cm
Diameter	16.8 cm
Mass centring range	$\pm 2.5°$ from horizontal
Lowest spurious resonance	> 140 Hz

The three platform seismometers were chosen to be hung below the top-plate rather than placed on top, or level with the top-plate. This allowed the diameter of the system to be constrained within the 1 m requirement without limiting the size of the load that could be placed on the top-plate. This seismometer arrangement also had the advantage that the CoG of the system would be lowered, increasing platform stability.

3.1.1. Control of the 2DoF Model: VIBISIO

Since this analysis focuses on the actuator mode of the facility, the force f_{IUT} is not present. Moreover, for the moment only the first actuator is considered since the objective is to design a control system to isolate the VIBISIO from ground vibrations. Thus, the model becomes:

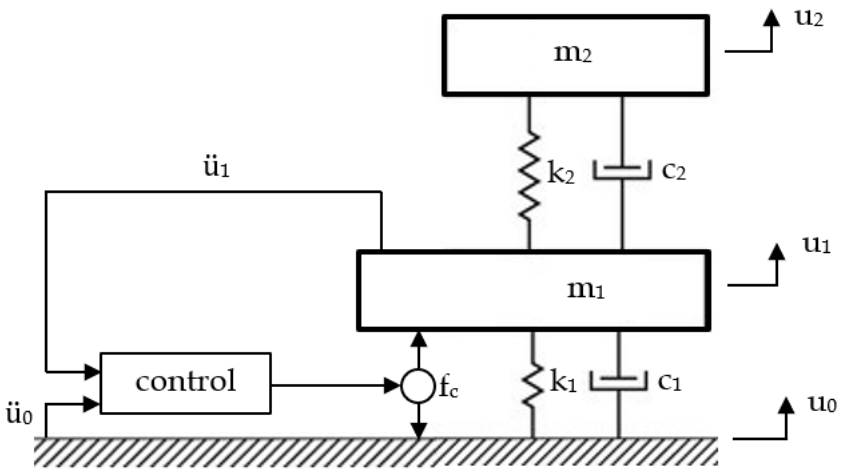

Figure 3.1: 2DoF model for the control

Since for the present analysis a Rayleigh damping matrix is considered, the equations of motion can be written with the Lagrangian approach without considering the damping in the beginning. The equations of motion of the 2DoF model in fig. 3.1 can be retrieved by computing the kinetic, potential and damping energies, and then the virtual work as follows:

$$T = \frac{1}{2}m_1\dot{u}_1^2 + \frac{1}{2}m_2\dot{u}_2^2 \tag{3.2}$$

$$V = \frac{1}{2}k_1(u_1 - u_0)^2 + \frac{1}{2}k_2(u_2 - u_1)^2 \tag{3.3}$$

$$D = 0 \tag{3.4}$$

$$\delta W = \delta u_1 f_c - \delta u_0 f_c = \delta(u_1 - u_0) f_c \tag{3.5}$$

The Lagrange equations of motion are calculated as:

$$\begin{cases} \frac{d}{dt}\left(\frac{\partial T}{\partial \dot{u}_1}\right) - \frac{\partial T}{\partial u_1} + \frac{\partial V}{\partial u_1} + \frac{\partial D}{\partial \dot{u}_1} = Q_1 \\ \frac{d}{dt}\left(\frac{\partial T}{\partial \dot{u}_2}\right) - \frac{\partial T}{\partial u_2} + \frac{\partial V}{\partial u_2} + \frac{\partial D}{\partial \dot{u}_2} = Q_2 \end{cases} \tag{3.6}$$

Hence, the equations of motion in absolute coordinates are:

$$\begin{cases} m_1\ddot{u}_1 + k_1(u_1 - u_0) - k_2(u_2 - u_1) = f_c \\ m_2\ddot{u}_2 + k_2(u_2 - u_1) = 0 \end{cases} \tag{3.7}$$

The relative displacements are:

$$y_1 = u_1 - u_0 \tag{3.8}$$

$$y_2 = u_2 - u_0 \tag{3.9}$$

By defining $k_{tot} = k_1 + k_2$ and $a_0 = \ddot{u_0}$, the equations of motion in relative coordinates are retrieved:

$$\begin{cases} m_1\ddot{y}_1 + k_{tot}y_1 - k_2y_2 = -m_1a_0 + f_c \\ m_2\ddot{y}_2 - k_2y_1 + k_2y_2 = -m_2a_0 \end{cases} \tag{3.10}$$

In matrix form:

$$\begin{bmatrix} m_1 & 0 \\ 0 & m_2 \end{bmatrix} \begin{Bmatrix} \ddot{y}_1 \\ \ddot{y}_2 \end{Bmatrix} + \begin{bmatrix} k_{tot} & -k_2 \\ -k_2 & k_2 \end{bmatrix} \begin{Bmatrix} y_1 \\ y_2 \end{Bmatrix} = \begin{Bmatrix} -m_1a_0 + f_c \\ -m_2a_0 \end{Bmatrix} \tag{3.11}$$

By adding the Rayleigh damping, where the damping matrix is defined as $\mathbf{C} = \alpha\mathbf{M} + \beta\mathbf{K}$, it results that:

$$\begin{bmatrix} m_1 & 0 \\ 0 & m_2 \end{bmatrix} \begin{Bmatrix} \ddot{y}_1 \\ \ddot{y}_2 \end{Bmatrix} + \begin{bmatrix} C_{11} & C_{12} \\ C_{21} & C_{22} \end{bmatrix} \begin{Bmatrix} \dot{y}_1 \\ \dot{y}_2 \end{Bmatrix} + \begin{bmatrix} k_{tot} & -k_2 \\ -k_2 & k_2 \end{bmatrix} \begin{Bmatrix} y_1 \\ y_2 \end{Bmatrix} = \begin{Bmatrix} -m_1a_0 + f_c \\ -m_2a_0 \end{Bmatrix} \tag{3.12}$$

which means:

$$\mathbf{M}\ddot{\mathbf{y}}(t) + \mathbf{C}\dot{\mathbf{y}}(t) + \mathbf{K}\mathbf{y}(t) = \mathbf{F}(t) \tag{3.13}$$

For completeness, the system of equations is:

$$\begin{cases} m_1\ddot{y}_1 + C_{11}\dot{y}_1 + C_{12}\dot{y}_2 + k_{tot}y_1 - k_2y_2 = -m_1a_0 + f_c \\ m_2\ddot{y}_2 + C_{21}\dot{y}_1 + C_{22}\dot{y}_2 - k_2y_1 + k_2y_2 = -m_2a_0 \end{cases} \tag{3.14}$$

By writing the equations of motion (eq. (3.14)) in the Laplace domain:

$$\begin{cases} (s^2m_1 + sC_{11} + k_{tot})y_1(s) + (sC_{12} - k_2)y_2(s) = -m_1a_0(s) + f_c(s) \\ (s^2m_2 + sC_{22} + k_2)y_2(s) + (sC_{21} - k_2)y_1(s) = -m_2a_0(s) \end{cases} \tag{3.15}$$

From eq. (3.8), it is possible to retrieve the absolute acceleration of mass m_1 as $\ddot{u}_1 = \ddot{y}_1 + a_0$ and the absolute acceleration of mass m_2 as $\ddot{u}_2 = \ddot{y}_2 + a_0$. These can be defined in the Laplace domain as: $a_1(s) = \ddot{u}_1(s) = s^2y_1(s) + a_0(s)$ and $a_2(s) = \ddot{u}_2(s) = s^2y_2(s) + a_0(s)$. By rearranging eq. (3.15), it is possible to retrieve two transfer functions. The subscript i can be equal to 1 or 2 depending on whether it is related to the degree of freedom u_1 or u_2, respectively.

- $P_i(s) = \frac{a_i(s)}{a_0(s)}$: represents the Primary path, from the base acceleration to the acceleration of the VIBISIO or of the MPLAT, depending on the value of the subscript i.
- $S_i(s) = \frac{a_i(s)}{f_c(s)}$: represents the Secondary path, from the actuator control force to the acceleration of the VIBISIO or of the MPLAT, depending on the value of the subscript i.

It results that:

$$a_1(s) = P_1(s)a_0(s) + S_1(s)f_c(s) \tag{3.16}$$

$$a_2(s) = P_2(s)a_0(s) + S_2(s)f_c(s) \tag{3.17}$$

The transfer functions of the Primary path, $P_i(s)$, and of the Secondary path, $S_i(s)$, can be retrieved in the following way.

First, it is necessary to define the $\mathbf{m}$ vector of masses and the $\mathbf{L}_c$ load vector:

$$\mathbf{m} = \begin{Bmatrix} -m_1 \\ -m_2 \end{Bmatrix} \tag{3.18}$$

$$\mathbf{L}_c = \begin{Bmatrix} 1 \\ 0 \end{Bmatrix} \tag{3.19}$$

$P_{all}(s)$ and $S_{all}(s)$ can be computed respectively as:

$$P_{all}(s) = s^2((s^2\mathbf{M} + s\mathbf{C} + \mathbf{K})^{-1}\mathbf{m}) + \begin{Bmatrix} 1 \\ 1 \end{Bmatrix} \tag{3.20}$$

$$S_{all}(s) = s^2((s^2\mathbf{M} + s\mathbf{C} + \mathbf{K})^{-1}\mathbf{L}_c) \tag{3.21}$$

It is possible to extract $P_1(s)$ and $P_2(s)$ from $P_{all}(s)$, while $S_1(s)$ and $S_2(s)$ from $S_{all}(s)$. $P_1(s)$ and $S_1(s)$ are obtained by taking the transfer function from input 1 ($a_0(s)$) to output 1 ($a_1(s)$) of $P_{all}(s)$ and $S_{all}(s)$, respectively. On the other hand, $P_2(s)$ and $S_2(s)$ are retrieved by considering the transfer function from input 1 ($a_0(s)$) to output 2 ($a_2(s)$) of $P_{all}(s)$ and $S_{all}(s)$, respectively. The TFs of the Primary and Secondary paths can now be written extensively, either considering the Rayleigh damping or the modal one.

- If the Rayleigh damping is considered, the equations of the transfer functions in which a_1 is involved are:

$$P_1(s) = \frac{\begin{array}{r}(m_2C_{12} + m_2C_{11})s^3 + (C_{11}C_{22} + m_2k_1 - C_{12}C_{21})s^2 + \\ + (C_{11}k_2 + C_{22}k_1 + C_{22}k_2 + C_{12}k_2 + C_{21}k_2)s + k_1k_2\end{array}}{D_1(s)} \tag{3.22}$$

$$S_1(s) = \frac{s^2(m_2s^2 + C_{22}s + k_2)}{D_1(s)} \tag{3.23}$$

where:

$$\begin{aligned} D_1(s) = m_1m_2s^4 + (m_1C_{22} + m_2C_{11})s^3 + (m_1k_2 + C_{11}C_{22} + m_2k_{tot} - C_{12}C_{21})s^2 + \\ + (C_{11}k_2 + C_{22}k_{tot} + C_{12}k_2 + C_{21}k_2)s + k_1k_2 \end{aligned} \tag{3.24}$$

On the other hand, the equations in which a_2 is involved are:

$$P_2(s) = \frac{(m_1C_{22} + m_1C_{21})s^3 + (C_{11}C_{22} - C_{12}C_{21}s^2) + \\ + (C_{22}k_{tot} + C_{11}k_2 + C_{21}k_2 + C_{12}k_2)s + k_1k_2}{D_2(s)} \tag{3.25}$$

$$S_2(s) = \frac{-s^2(C_{21}s - k_2)}{D_2(s)} \tag{3.26}$$

where:

$$D_2(s) = m_1m_2s^4 + (m_2C_{11} + m_1C_{22})s^3 + (m_2k_{tot} + C_{11}C_{22} + m_1k_2 - C_{12}C_{21})s^2 + \\ + (C_{22}k_{tot} + C_{11}k_2 + C_{21}k_2 + C_{12}k_2)s + k_1k_2 \tag{3.27}$$

- If instead the modal damping is considered, the equations of the transfer functions in which a_1 is involved are:

$$P_1(s) = (sc_1 + k_1)Q_1(s) \tag{3.28}$$

$$S_1(s) = s^2Q_1(s) \tag{3.29}$$

where:

$$Q_1(s) = \frac{s^2m_2 + sc_2 + k_2}{(s^2m_1 + sc_{tot} + k_{tot})(s^2m_2 + sc_2 + k_2) - (sc_2 + k_2)^2} \tag{3.30}$$

On the other hand, the equations of the transfer functions in which a_2 is involved are:

$$P_2(s) = (sc_1 + k_1)Q_2(s) \tag{3.31}$$

$$S_2(s) = s^2Q_2(s) \tag{3.32}$$

where:

$$Q_2(s) = \frac{sc_2 + k_2}{s^4 m_1 m_2 + s^3(m_2 c_{tot} + m_1 c_2) + s^2(m_2 k_{tot} + c_2 c_{tot} + m_1 k_2 - c_2^2) + \\ + s(c_2 k_{tot} + c_{tot} k_2 - 2c_2 k_2) + k_2 k_{tot} - k_2^2} \tag{3.33}$$

Hence, the block diagram of the **open-loop** control system is:

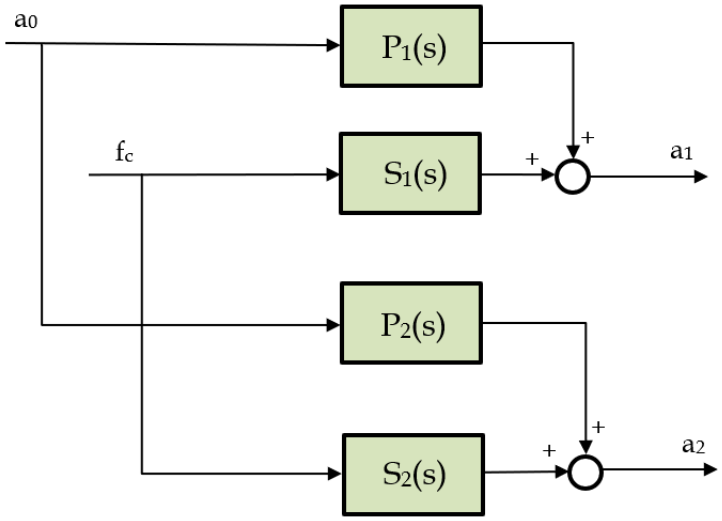

Figure 3.2: Open-loop control system of the 3DoF model

The open-loop transmissibility functions, from a_0 to a_1 and from a_0 to a_2, result:

$$\frac{a_1(s)}{a_0(s)} = T_{1open}(s) = P_1(s) \tag{3.34}$$

$$\frac{a_2(s)}{a_0(s)} = T_{2open}(s) = P_2(s) \tag{3.35}$$

Three cases of control strategies can be investigated:

1. FB controller;
2. FF controller;
3. Combined FB and FF controller.

The block diagram of the **closed-loop** control system is the following:

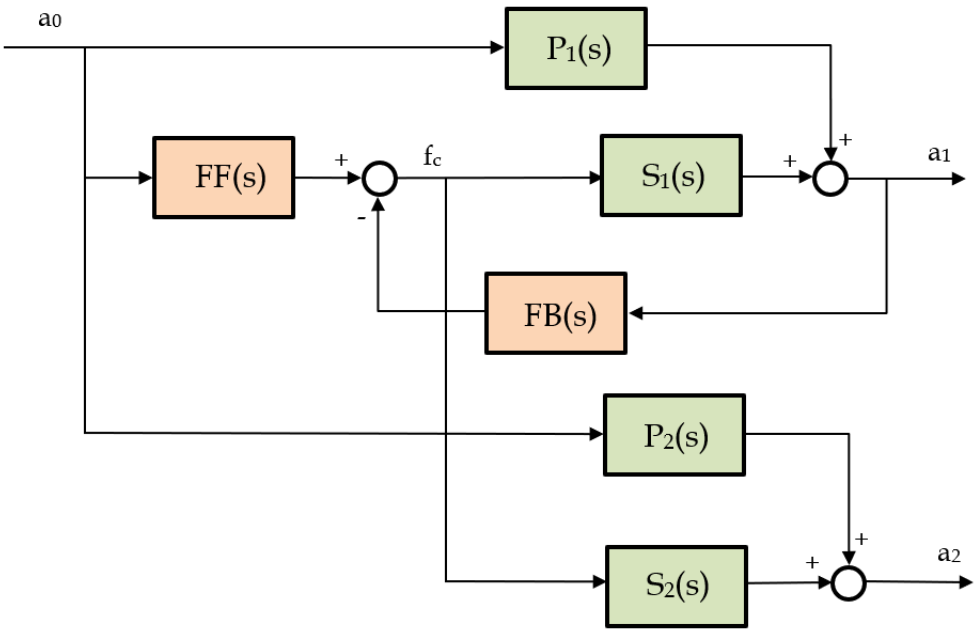

Figure 3.3: Closed-loop control system of the 2DoF model

The three control cases consist of:

1. FF(s)=0, design FB(s);
2. FB(s)=0, design FF(s);
3. Design FB(s) and FF(s) by combining the previous designs.

The closed-loop transmissibility functions, from a_0 to a_1 and from a_0 to a_2, result:

$$\frac{a_1(s)}{a_0(s)} = T_{1closed}(s) = \frac{P_1(s) + S_1(s)FF(s)}{1 + S_1(s)FB(s)} \tag{3.36}$$

$$\frac{a_2(s)}{a_0(s)} = T_{2closed}(s) = P_2(s) + S_2(s)FF(s) - S_2(s)FB(s)T_{1closed}(s) \tag{3.37}$$

However, the real actuators and seismometers are characterised by a saturation level and an internal dynamics respectively, which can be modelled in order to obtain results closer to reality. The specifications of the real sensors and actuators present on the facility are reported in an internal document provided by NPL.

- Each one of the mounted **actuators** can provide up to ± 1 N force. Three are the longitudinal actuators in the VIBISIO, and the z component of the control force they

produce is always one. Thus, it follows that the equivalent force to be considered as the saturation can be set to $\pm 3\ N$. The saturation of the actuators is modelled in Simulink® by means of a specific block called *Saturation*.

- The model of the **seismometers** is Güralp CMG-3T. The amplitude and phase which characterise this seismometer model are:

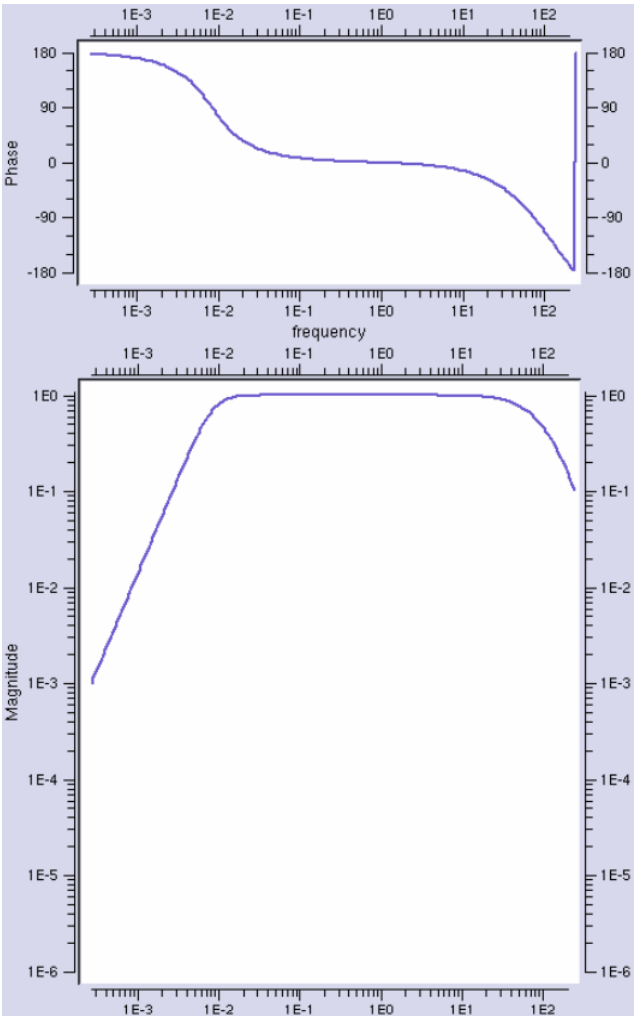

Figure 3.4: Güralp CMG-3T [2]

The magnitude graph in fig. 3.4 shows that the passband of the seismometer is from 0.01 Hz to 100 Hz approximately. The internal dynamics of the seismometer is modelled by means of a passband filter with the following transfer function:

$$H(s) = \frac{s}{s+a}\frac{b}{s+b} \tag{3.38}$$

where the first fraction represents a high-pass filter and the second one a low-pass

filter. The parameters a and b are tuned according to the passband of the sensor, from which it results that $a = 2\pi 0.01\ rad/s$ and $b = 2\pi 100\ rad/s$. Since the peaks of the FRFs are in the low-frequency range, the bandwidth of the seismometer will probably not cause any problem at frequencies higher than 100 Hz, while it can provide an imprecise measurement at frequencies lower than 0.01 Hz. A solution to this issue can be to increase the control gain. Anyway, a phase lag, which adds negative phase to the system over the specified frequency range [27], could take to instability or a decrease in performances.

By adding the saturation block and the internal dynamics of the seismometer $H(s)$, the block diagram becomes:

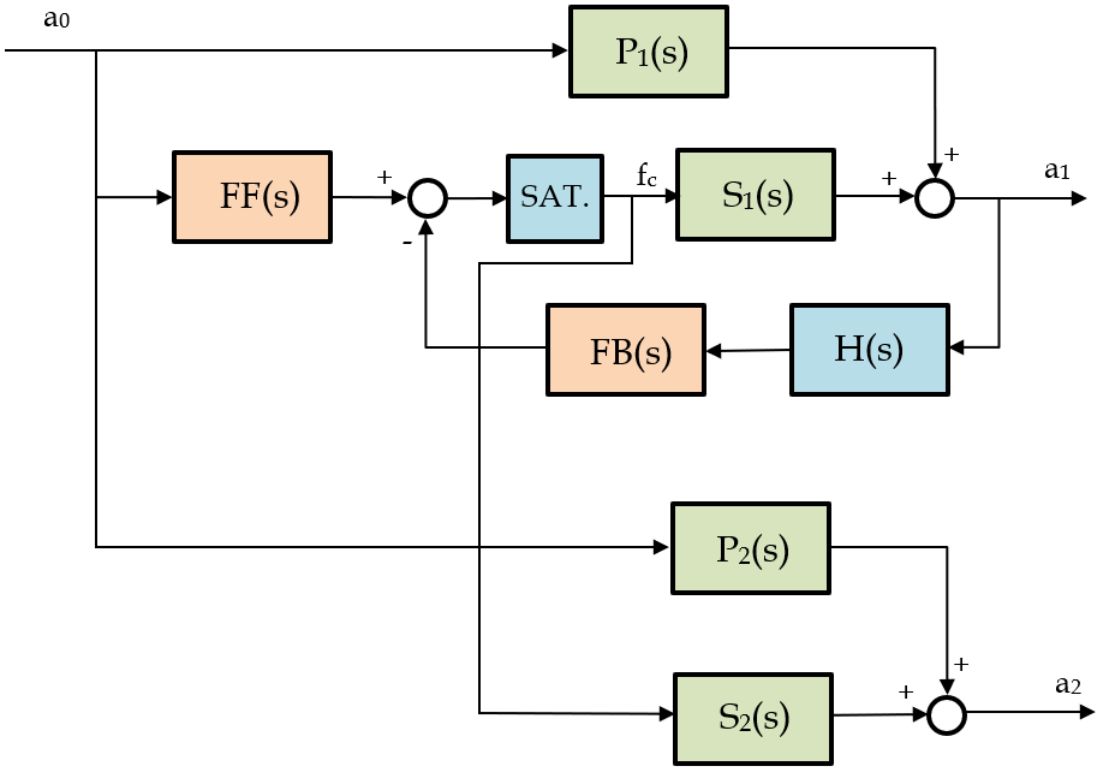

Figure 3.5: Closed-loop control system of the 2DoF model, including the actuator's saturation and the internal dynamics of the seismometer

By taking into account also the internal dynamics of the seismometer, the closed-loop transmissibility function from a_0 to a_1 becomes:

$$\frac{a_1(s)}{a_0(s)} = T_{1_{closed}}(s) = \frac{P_1(s) + S_1(s)FF(s)}{1 + S_1(s)FB(s)H(s)} \tag{3.39}$$

The closed-loop transmissibility from a_0 to a_2 is instead:

$$\frac{a_2(s)}{a_0(s)} = T_{2_{closed}}(s) = P_2(s) + S_2(s)FF(s) - S_2(s)FB(s)H(s)T_{1_{closed}}(s) \tag{3.40}$$

The excitation signal is the base acceleration a_0, which derives from the ground vibrations present in the building in which the tests are carried out. The acceleration a_0 has a constant power spectral density of 1 G^2/Hz in the frequency range between 0.01 Hz and 20 Hz. It can be modelled as a white noise, which is a a random signal having equal intensity at different frequencies, giving it a constant power spectral density. [10] The employed Simulink® block is called $Band - Limited\ White\ Noise$, which receives as inputs a noise power of 1 W/Hz and a sample time equal to $1/f_s$, with $f_s = 100\ Hz$. To tune the value of the excitation, the output signal of the $Band - Limited\ White\ Noise$ block is multiplied by a multiplicative constant k. In order to test the effectiveness of the control system, it is necessary to check that this excitation level is equal or larger than the maximum value of the total accelerations typical for the environment in which the testing facility is placed. Figure 3.6 shows what are the limit levels of the total accelerations on the z axis for different destinations of usage:

VALORI E LIVELLI LIMITE DELLE ACCELERAZIONI COMPLESSIVE PONDERATE IN FREQUENZA VALIDI PER L'ASSE z		
Destinazione d'uso	**Accelerazione**	
	m/s²	**dB**
Aree critiche	5,0 10-3	74
Abitazioni notte	7,0 10-3	77
Abitazioni giorno	10,0 10-3	80
Uffici	20,0 10-3	86
Fabbriche	40,0 10-3	92

Figure 3.6: Limit levels of the total accelerations on the z axis [4]

The limit level of the total acceleration considered for this specific case is the one related to offices, which is 0.02 m/s^2. Hence, the attenuation of the peaks must be obtained for a value of acceleration a_0 at least equal to 0.02 m/s^2.
Moreover, to implement the control it is vital to underline the fact that the integrator must not be ideal, but a **pseudo-integrator** must be used. Since there exist some low-frequency components, they would be integrated if an ideal integrator was used and hence

the response would keep growing. The transfer function of the pseudo-integrator is:

$$\tilde{H}(s) = \frac{s}{s^2 + 2\xi\omega s + \omega^2} \tag{3.41}$$

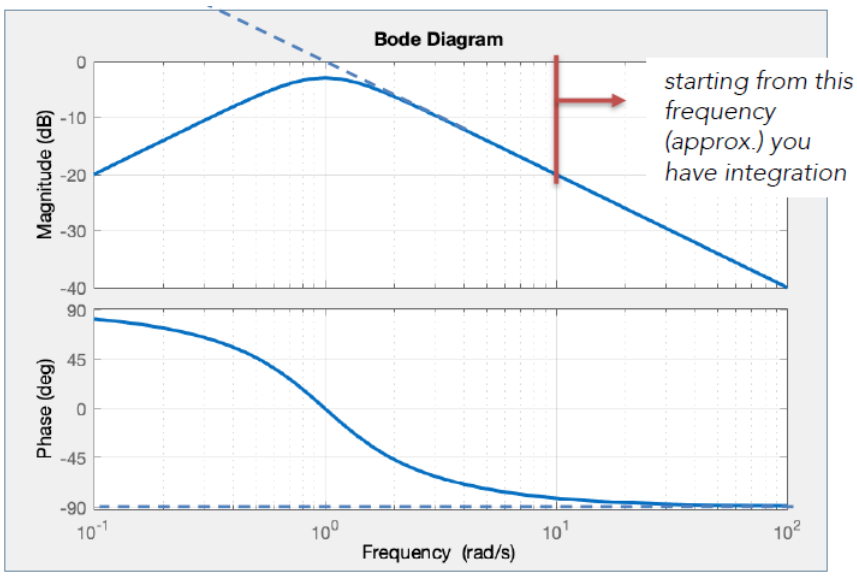

Figure 3.7: Pseudo-integrator [13]

The design of the integrator consists of selecting the frequency approximately one decade below the frequency at which it is desired to start to integrate (see fig. 3.7) and the damping is selected approximately equal to 0.7 to avoid amplification. [13] In fact, the parameters ξ and ω have been chosen as:

- $\xi = 0.707$ in order to keep the transition smooth;
- $\omega = 2\pi 0.01\ rad/s$, where the frequency 0.01 Hz has been selected as one decade lower than the first resonance peak of the frequency response function, which is around 0.45 Hz. It has not been taken the value 0.04 Hz, but 0.01 Hz to be conservative in the transition region.

Feedback Control: Description

The **sky-hook damping** has been selected as a FB control design approach. Consider a single-axis soft isolator connecting two rigid bodies, which consists of a soft spring k acting in parallel with a force actuator f_c, to isolate the sensitive payload M from the disturbance source m. There is a seismometer to measure the velocity of the payload and the signal is fed back to the force actuator. The sky-hook damper is represented in

fig. 3.8, imagining that the payload is suspended by a damper to a point in the sky. [17]

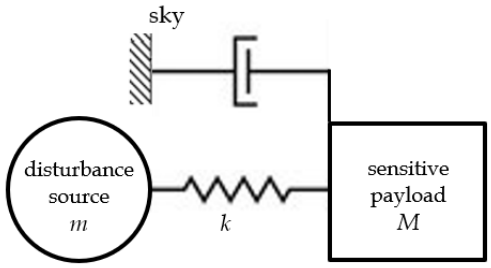

Figure 3.8: Equivalent sky-hook damper

In the sky-hook damper technique, the FB is based on the absolute acceleration of the sensitive payload, $a_1(s)$, with integral controller $g\tilde{H}(s)$ leading to the FB equation:

$$f_c(s) = -g\tilde{H}(s)a_1(s) \tag{3.42}$$

It can be clearly seen that the active control force is proportional to the absolute velocity of the payload. By defining $FB(s) = g\tilde{H}(s)$, where the integrator is necessary to obtain the velocity from the acceleration, eq. (3.42) becomes:

$$f_c(s) = -FB(s)a_1(s) \tag{3.43}$$

Now, the transmissibility function in case of FB control with sky-hook damping can be retrieved. Considering $FF(s) = 0$, eq. (3.39) becomes:

$$T_{sky}(s) = \frac{P(s)}{1 + S(s)FB(s)H(s)} \tag{3.44}$$

Feedback Control: Results

In the beginning of the following analysis, the internal dynamics of the seismometer and the saturation of the actuator are not taken into account. The multiplicative constant of the excitation, k, has been set to 0.00045, since in this way the disturbance a_0 assumes a maximum value in the order of 0.02 m/s^2, as required by fig. 3.6.
In fig. 3.9 and fig. 3.11 are represented the frequency responses of the closed-loop transmissibilities, obtained with the MATLAB® command *bodeplot*, varying the value of the gain from 0 to 1000.

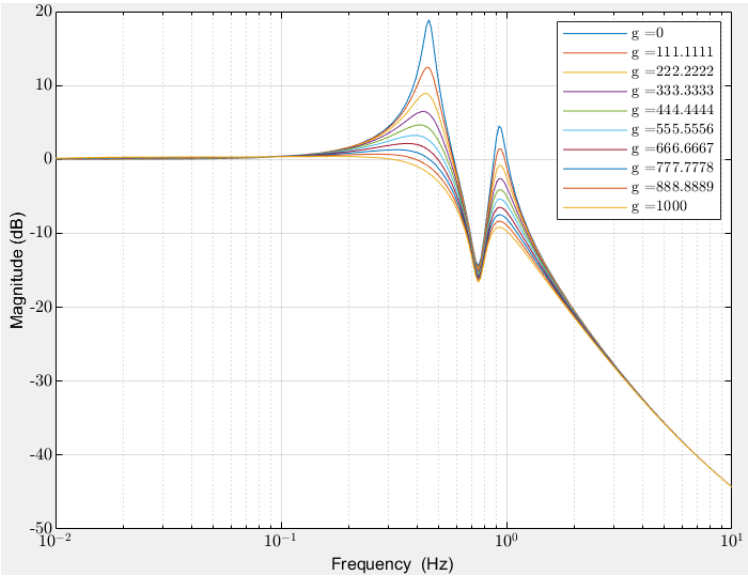

Figure 3.9: Closed loop transmissibility (*bode* of transfer function) from a_0 to a_1

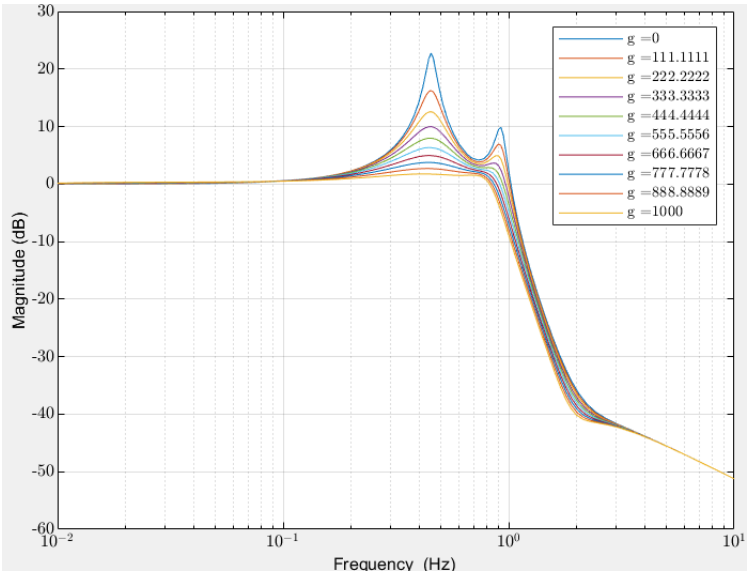

Figure 3.10: Closed loop transmissibility (*bode* of transfer function) from a_0 to a_2

Figure 3.11 and fig. 3.12 display the FRFs of the closed-loop transmissibilities retrieved with the MATLAB® command $tfestimate$ from the time responses obtained with $lsim$.

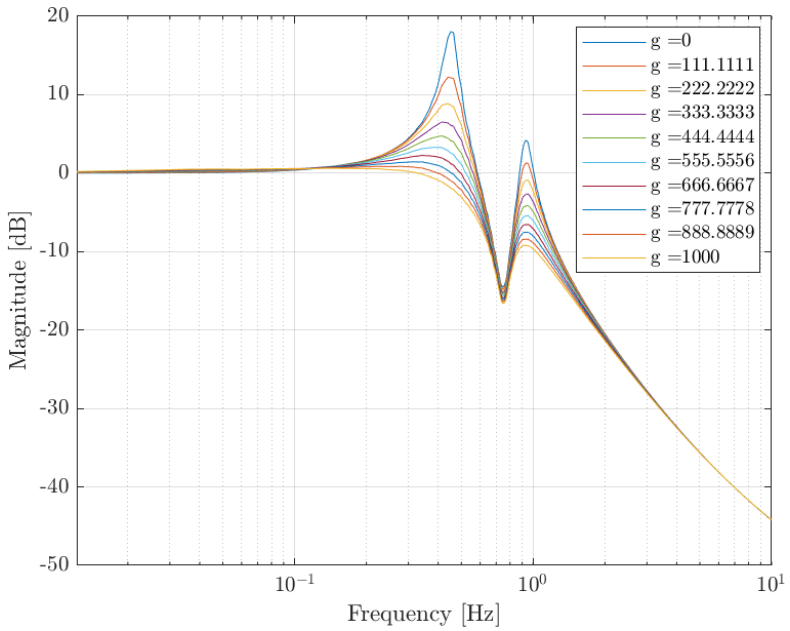

Figure 3.11: Closed loop transmissibility ($tfestimate$ from response with $lsim$) from a_0 to a_1

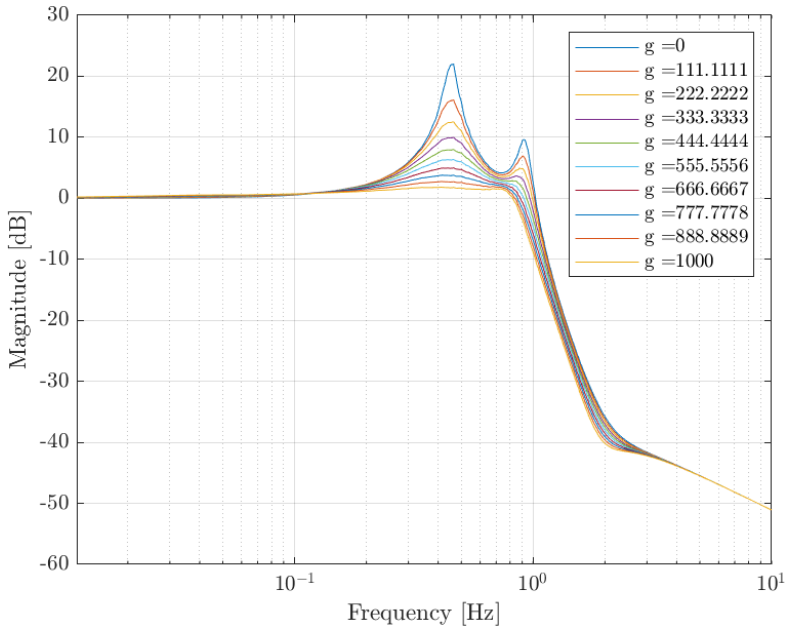

Figure 3.12: Closed loop transmissibility ($tfestimate$ from response with $lsim$) from a_0 to a_2

From the four figures above, it can be noted that, by changing the values of the gain, it results that the two resonance peaks are attenuated: the higher is the gain, the larger is the attenuation. It is shown that the complete flattening of the first peak and the

best attenuation of the second one occur when choosing $g = 1000$. However, it has to be checked that for this value of the gain the actuator does not reach saturation.
Figure 3.13 and fig. 3.14 show the FRFs of the transmissibility from a_0 to a_1 and from a_0 to a_2, respectively. They are obtained by means of the command $tfestimate$, taking as inputs the temporal history of the accelerations retrieved from Simulink®. The simulation is stopped when the actuators reach saturation, hence the last gain value in the legend is the largest gain among the ones taken as samples for which the actuator does not saturate.

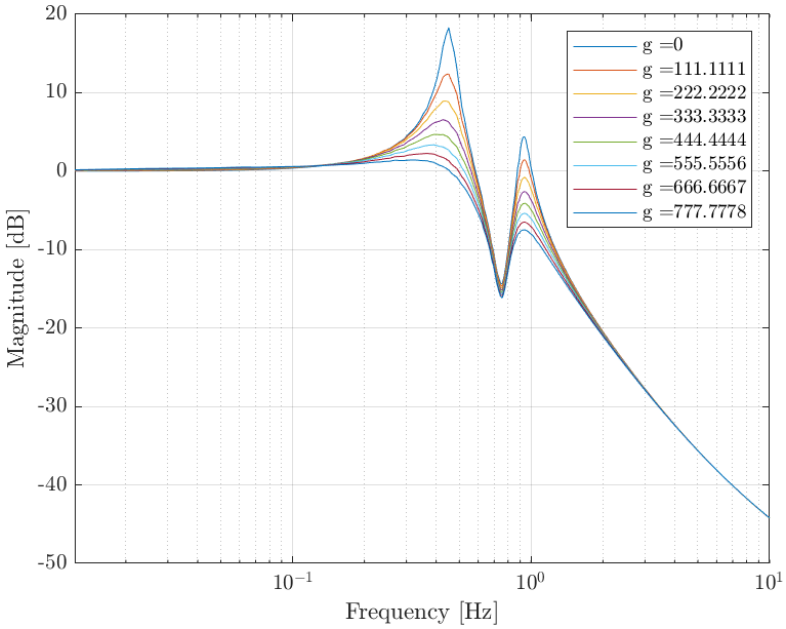

Figure 3.13: Closed loop transmissibility ($tfestimate$ from Simulink® time responses) from a_0 to a_1

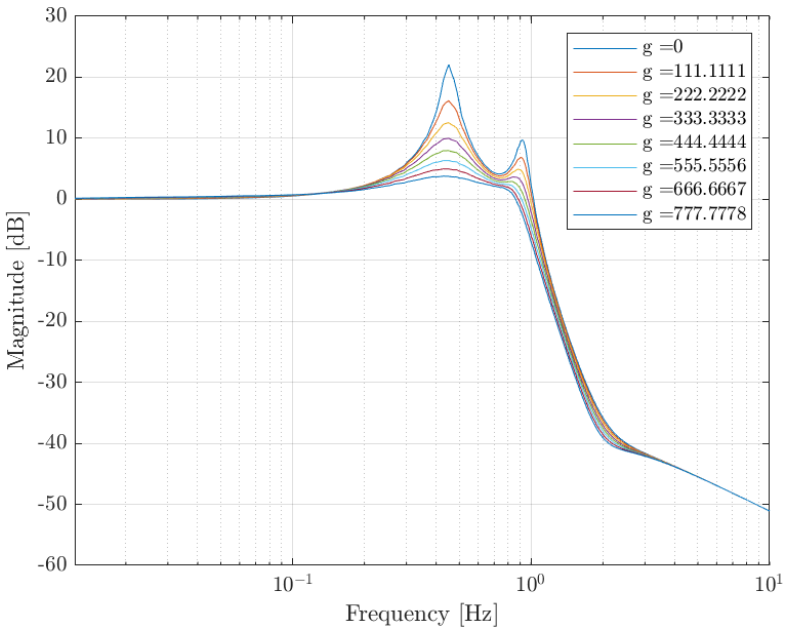

Figure 3.14: Closed loop transmissibility ($tfestimate$ from Simulink® time responses) from a_0 to a_2

From fig. 3.13 and fig. 3.14 it can be appreciated that the largest gain, among the considered ones, for which saturation is not reached is 777.78. In fact, for the next value of the gain, 888.89, the actuator saturates, as it can be seen in fig. 3.15, where for that value of the gain f_c reaches $\pm 3N$.

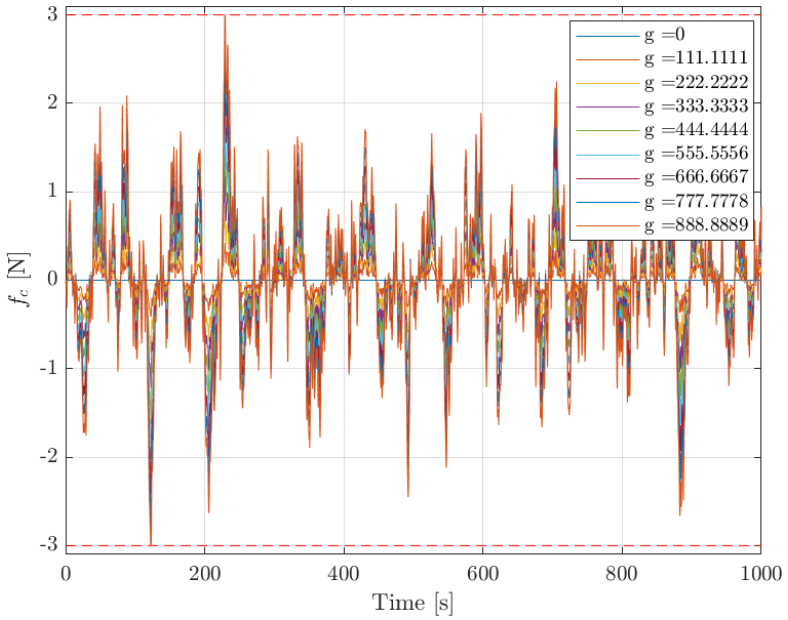

Figure 3.15: Actuator control force for different values of the gain until saturation

To define the largest gain for which saturation is not reached, the bisection method is used, which consists of iteratively reducing the interval between the largest gain for which saturation is not reached and the first gain for which saturation is reached. The largest gain value for which saturation is not reached is found to be equal to 824.83.
Figure 3.16 and fig. 3.17 show the comparison between the open-loop and the closed-loop responses with $g = 824.84$.

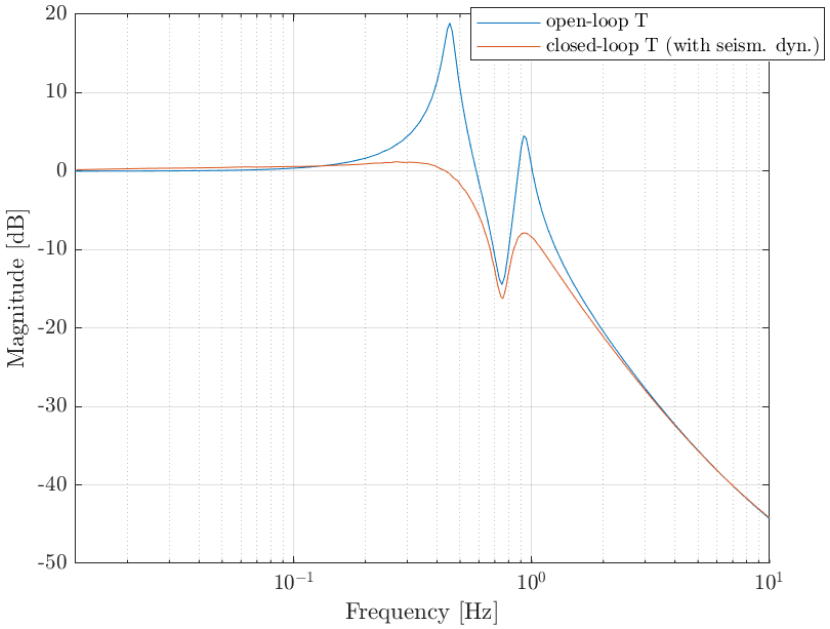

Figure 3.16: Comparison between open-loop and closed-loop response, transmissibility from a_0 to a_1, $g = 824.84$

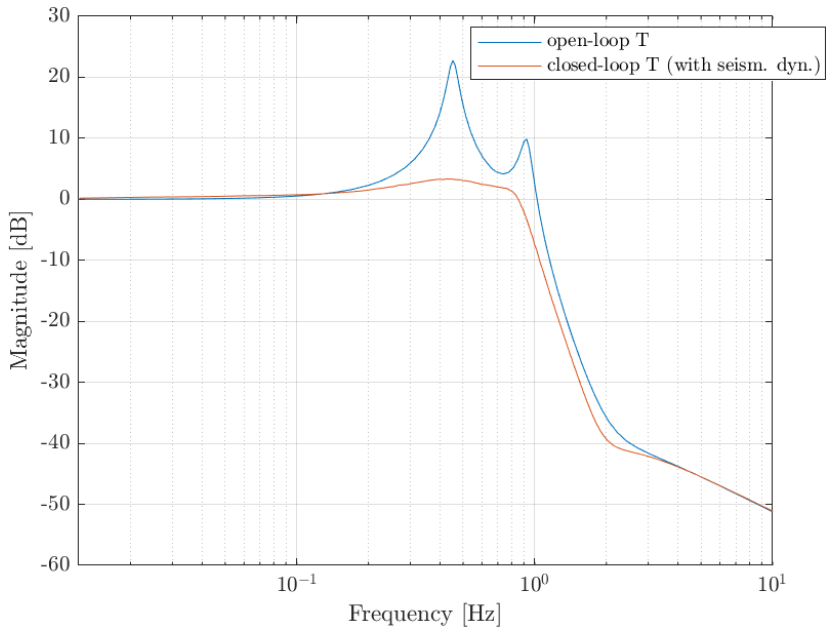

Figure 3.17: Comparison between open-loop and closed-loop response, transmissibility from a_0 to a_2, $g = 824.84$

Since the required attenuation is of $-20\ dB$, table 3.2 and table 3.3 report the magnitude difference in dB between the peaks of the closed loop responses and the target value which would be obtained with an attenuation of $-20\ dB$ of the original peaks (in correspondence of the resonance frequencies).

Table 3.2: Attenuation of the peaks: transmissibility from a_0 to a_1

Gain	**First peak** $(0.45Hz)$ **[dB]**	**Second peak** $(0.93Hz)$ **[dB]**
0	20	20
111.11	14.0848	17.0033
222.22	10.5105	14.7624
333.33	7.9645	12.9764
444.44	5.9910	11.4929
555.56	4.3810	10.2249
666.67	3.0218	9.1178
777.78	1.8460	8.1355
824.83	1.3923	7.7507

Table 3.3: Attenuation of the peaks: transmissibility from a_0 to a_2

Gain	**First peak** $(0.45Hz)$ **[dB]**	**Second peak** $(0.93Hz)$ **[dB]**
0	20	20
111.11	14.0614	16.9022
222.22	10.4646	14.5591
333.33	7.8955	12.6695
444.44	5.8985	11.0810
555.56	4.2648	9.7066
666.67	2.8817	8.4917
777.78	1.6819	7.4003
824.83	1.2179	6.9689

From table 3.2 and table 3.3, it can be appreciated that the distance between the peaks in closed loop and the target magnitude if an attenuation of $-20\ dB$ was present decreases the more the gain increases, which means that an increase in the gain leads to a flattening of the peaks. Moreover, it can be noted that the same gain generates a similar level of attenuation of the same peak, both in the case of transmissibility from a_0 to a_1 and of transmissibility from a_0 to a_2. Furthermore, from the same tables it is evident that the first resonance peak is much better attenuated than the second one.
The most relevant conclusion is that the largest gain for which no saturation occurs, equal to 824.83, is not able to generate an attenuation of the peaks of $-20\ dB$, given the considered excitation level (multiplicative constant of the excitation, k, equal to 0.00045). To have a stronger attenuation, the addition of a FF control is necessary or, otherwise, a different control strategy must be followed, for example the $H - infinity$ method [17].

The objective of the control is to obtain the desired attenuation of the resonance peaks also in the case of the **highest expected excitation**. Even if the requirement on the maximum excitation level in laboratories is $a_0 = 0.02\ m/s^2$ (fig. 3.6), it is possible to study how much the excitation level can be increased while maintaining an acceptable attenuation of the peaks. Since the actuators are already mounted on the facility, their characteristics are fixed, in particular their saturation. Under the saturation constraint, it is possible to obtain the desired performances only by tuning the gain and by granting that the excitation level remains below a threshold. As a matter of fact, a compromise must be reached, since both a too high gain or a too high excitation level prevent from respecting the saturation constraint.

In the following, it is looked for the largest gain which avoids saturation when the excitation level is increased. Hence, the multiplicative constant of the excitation, k, is gradually increased starting from the initial value of 0.00045.

- If k is set to 0.0008, saturation is reached when the gain becomes 555.56, as it can be noted from the time history of the actuator control force in fig. 3.18.

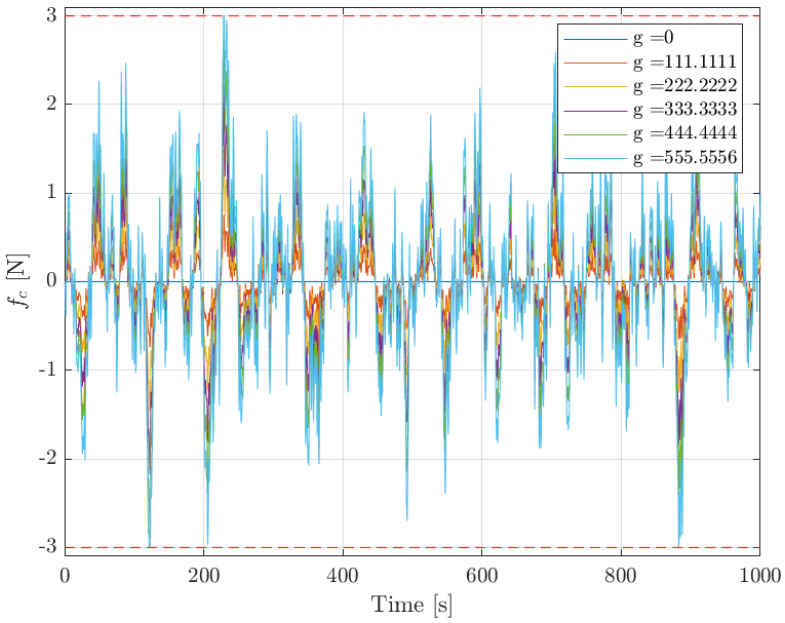

Figure 3.18: Actuator control force until saturation, excitation with $k = 0.0008$

Figure 3.19 and fig. 3.20 display the closed-loop frequency responses for the different values of the gain for which saturation is not reached.

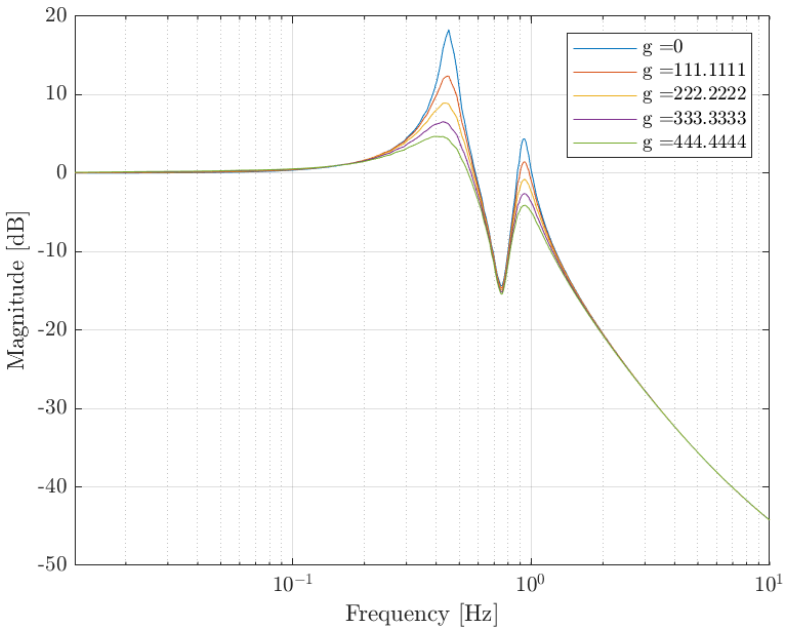

Figure 3.19: Damping for different values of the gain before saturation, excitation with $k = 0.0008$, transmissibility from a_0 to a_1

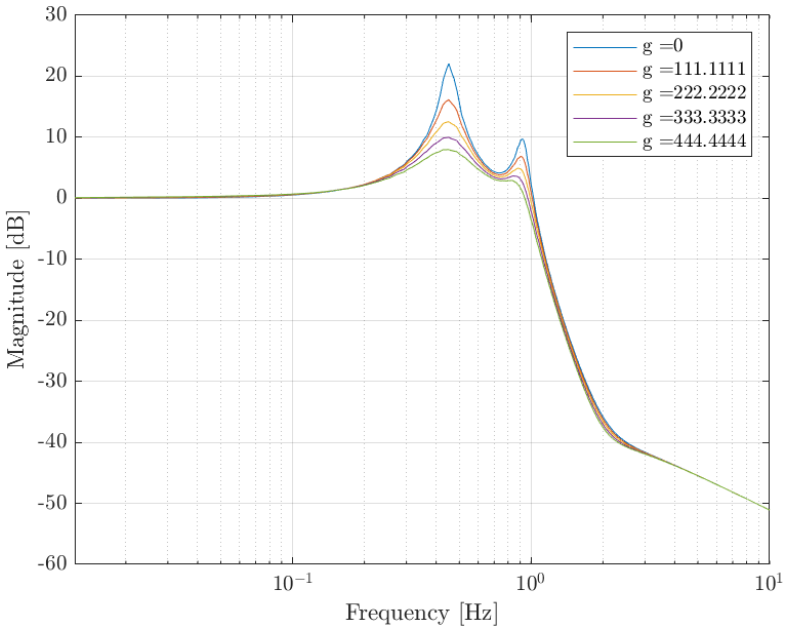

Figure 3.20: Damping for different values of the gain before saturation, excitation with $k = 0.0008$, transmissibility from a_0 to a_2

- If k is set to 0.0015, saturation is reached when the gain becomes 333.33, as it can be noted from the time history of the actuator control force in fig. 3.21.

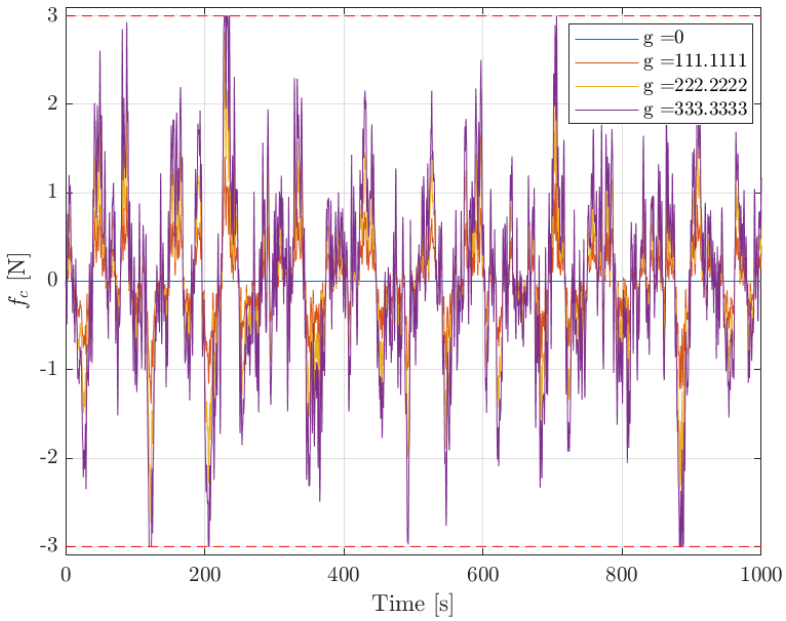

Figure 3.21: Actuator control force until saturation, excitation with $k = 0.0015$

Figure 3.22 and fig. 3.23 display the closed-loop frequency responses for the values of the gain for which saturation is not reached.

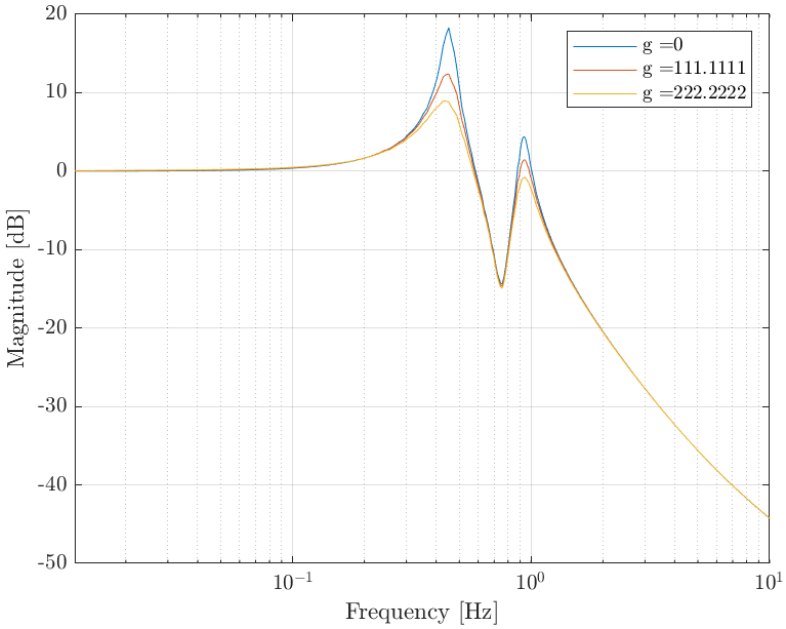

Figure 3.22: Damping for different values of the gain, excitation with $k = 0.0015$, transmissibility from a_0 to a_1

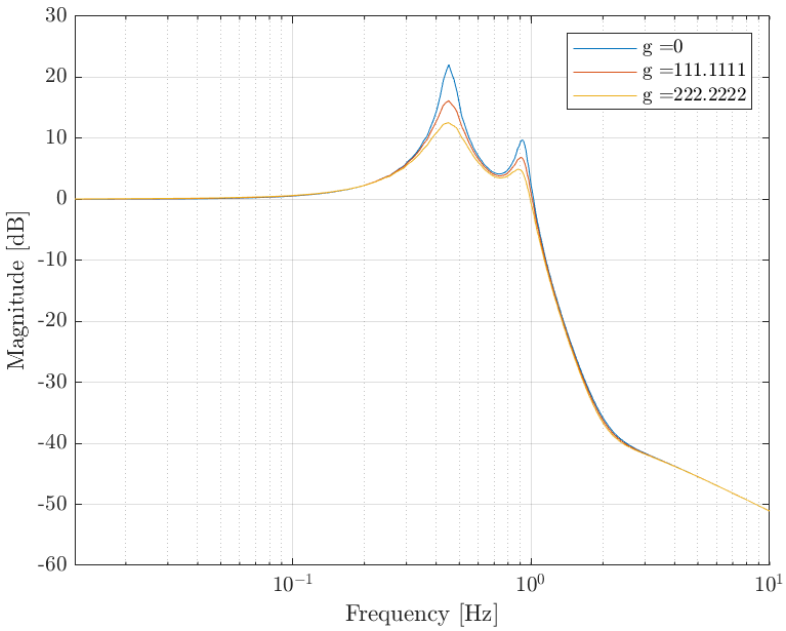

Figure 3.23: Damping for different values of the gain, excitation with $k = 0.0015$, transmissibility from a_0 to a_2

- $k = 0.005$: Saturation is reached when the gain becomes 111.11, as it can be noted from the time history of the actuator control force in fig. 3.24.

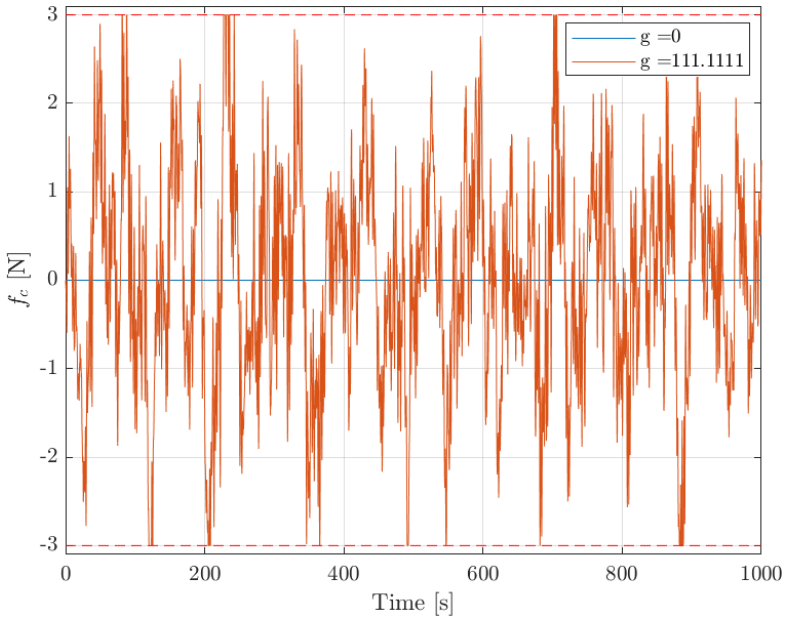

Figure 3.24: Actuator control force until saturation, excitation with $k = 0.005$

Figure 3.25 and fig. 3.26 display the closed-loop frequency responses for the unique value of the gain for which saturation is not reached. This value is $g = 0$, hence the

open loop response is obtained.

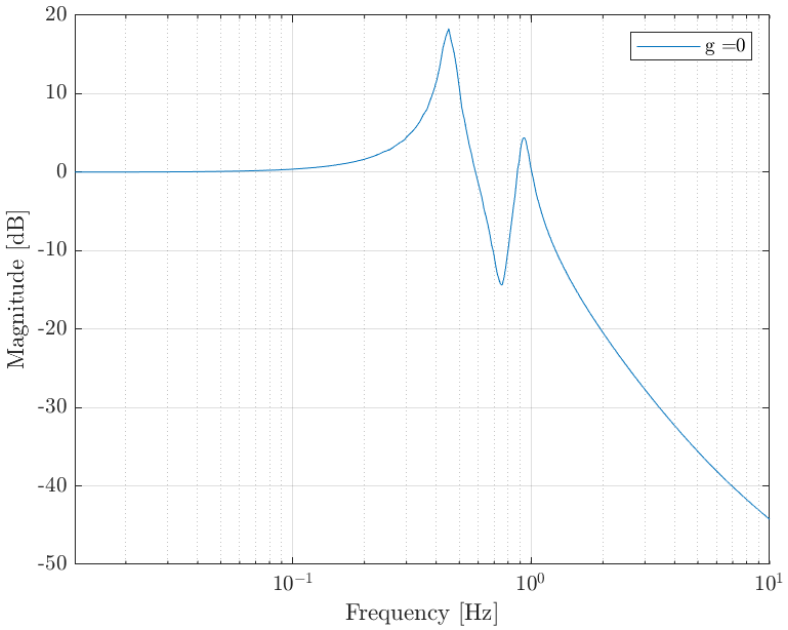

Figure 3.25: Damping for the unique value of the gain which does not reach saturation, excitation with $k = 0.005$, transmissibility from a_0 to a_1

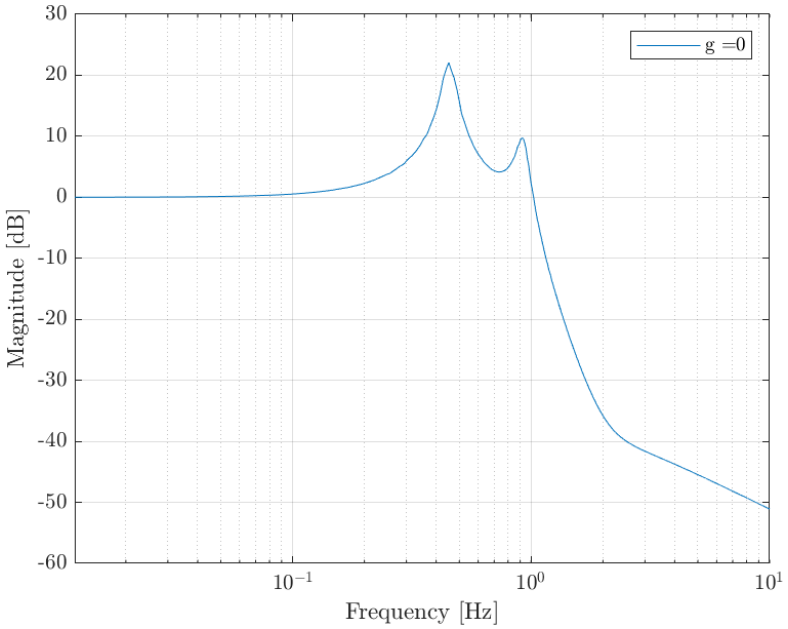

Figure 3.26: Damping for the unique value of the gain which does not reach saturation, excitation with $k = 0.005$, transmissibility from a_0 to a_2

As it can be seen from fig. 3.25 and fig. 3.26, in case of $k = 0.005$ no value of the gain allows to control the system without reaching saturation of the actuator.

From these simulations, it results that an increase in the excitation level causes a decrease in the maximum possible attenuation of the peaks before reaching saturation. In case of $k = 0.0008$, the maximum attenuation before saturation is not satisfactory, as it can be seen in fig. 3.19 and fig. 3.20. After some iterations, it has been found that the largest excitation for which the peaks remain fairly damped before saturation is $k = 0.00055$, with a resulting maximum value of the acceleration a_0 of 0.0247 m/s^2. For such an excitation value, the maximum allowable gain before saturation is 668.99. The resulting transmissibility FRFs are shown in fig. 3.27 and fig. 3.28.

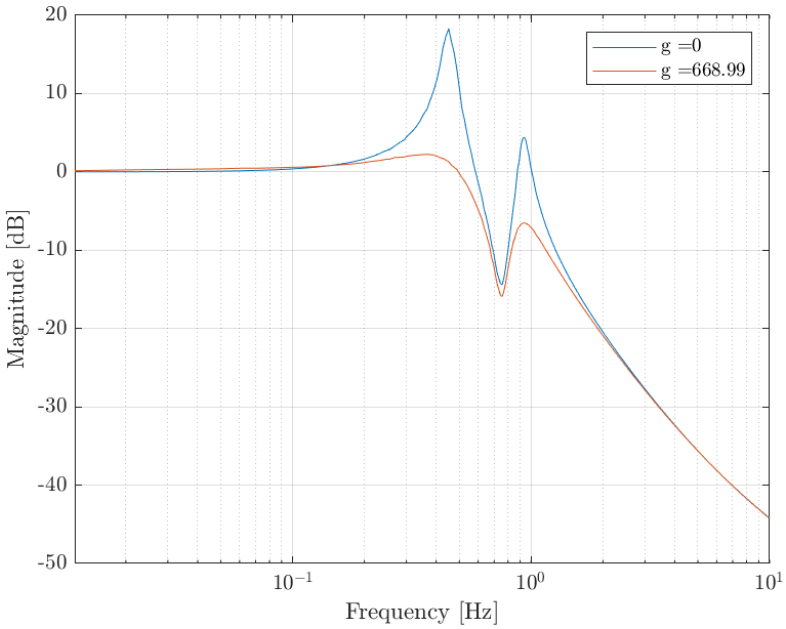

Figure 3.27: Magnitude plot, comparison between open-loop and closed-loop transmissibilities ($g = 668.99$, $k = 0.00055$): transmissibility from a_0 to a_1

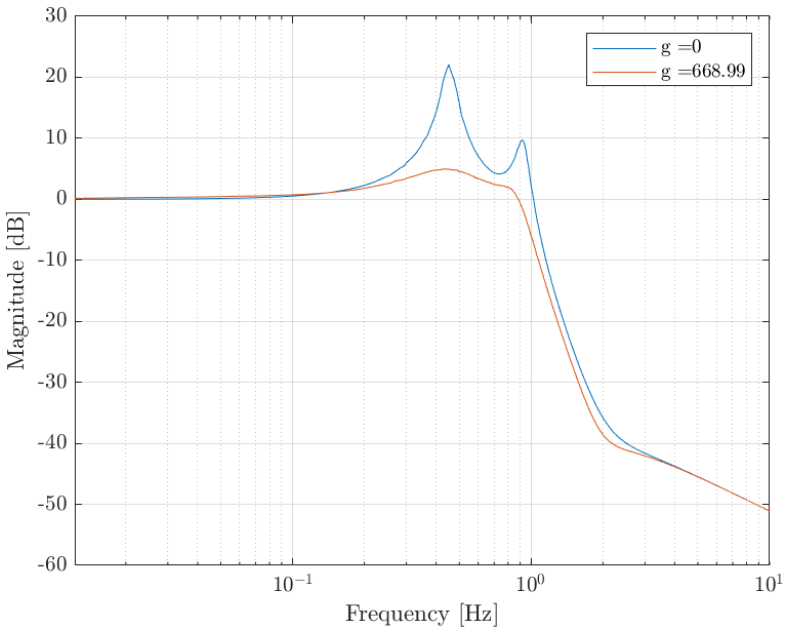

Figure 3.28: Magnitude plot, comparison between open-loop and closed-loop transmissibilities ($g = 668.99$, $k = 0.00055$): transmissibility from a_0 to a_2

In this case, the difference between the damped peak and the desired attenuation of $-20\ dB$ is 2.8817 dB for the first peak and 8.4917 dB for the second one. As expected, for such an excitation value, the maximum obtainable attenuation and its correspondent gain are lower than in the case with $k = 0.00045$. Hence, also in this case it is necessary to add a FF control or to adopt a different control strategy if the target attenuation of $-20\ dB$ needs to be obtained.
However, since it is not necessary to consider an excitation level higher than 0.02 m/s^2 (fig. 3.6), in the following it is considered $k = 0.00045$, with the corresponding maximum acceptable gain of 824.83.

In fig. 3.29 and fig. 3.30, it is desired to highlight the difference between the closed-loop frequency response with and without the addition of the internal dynamics of the seismometer.

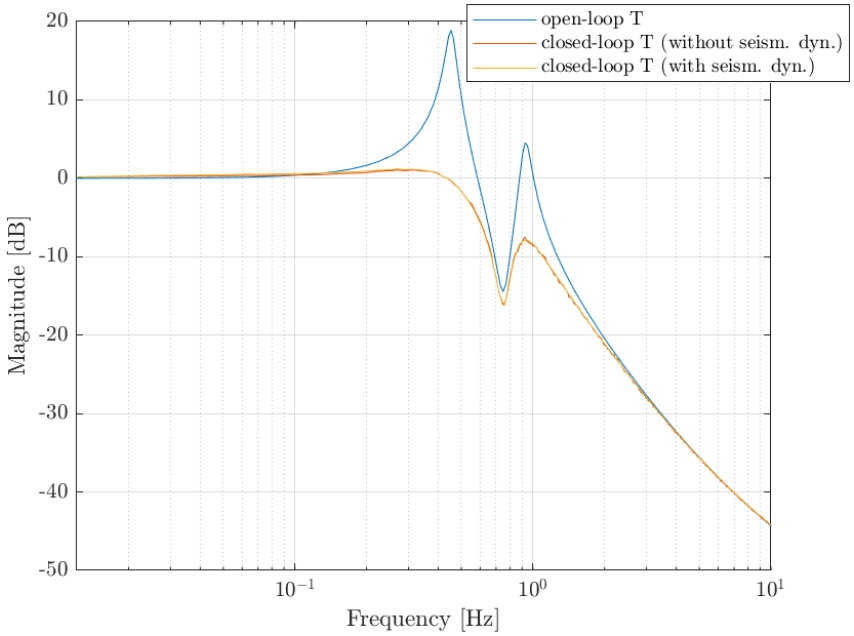

Figure 3.29: Magnitude plot, comparison between open-loop and closed-loop transmissibilities ($g = 824.83$, $k = 0.00045$): transmissibility from a_0 to a_1

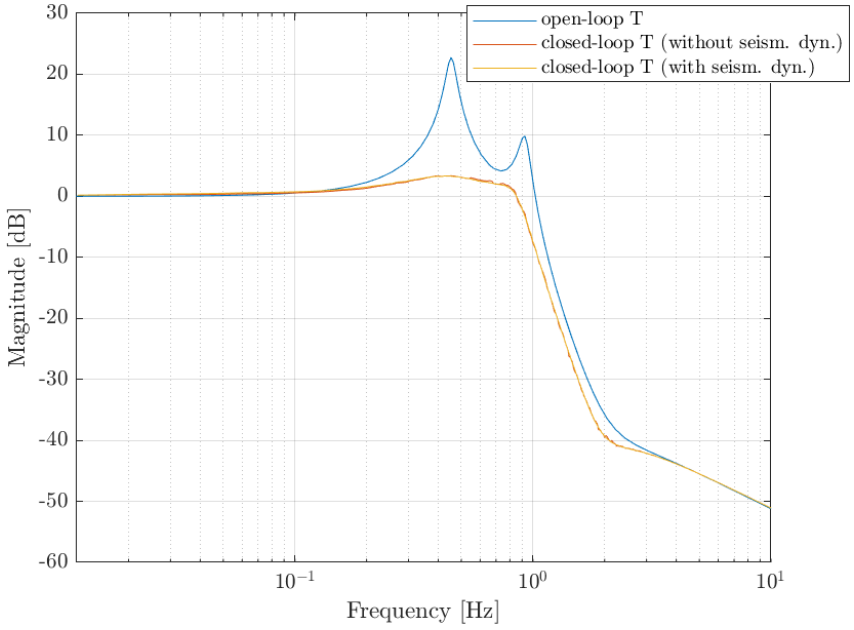

Figure 3.30: Magnitude plot, comparison between open-loop and closed-loop transmissibilities ($g = 824.83$, $k = 0.00045$): transmissibility from a_0 to a_2

From fig. 3.29 and fig. 3.30, it results that with a gain of 824.83 the addition of the internal dynamics of the seismometer does not significantly affect the magnitude of the closed-loop FRF.

As far as the phase is concerned, the closed-loop response detaches from the open-loop one. However, the behaviour of the closed-loop curve, either with or without the addition of the internal dynamics of the seismometer, is considerably similar, as it can be noted from fig. 3.31 and fig. 3.32:

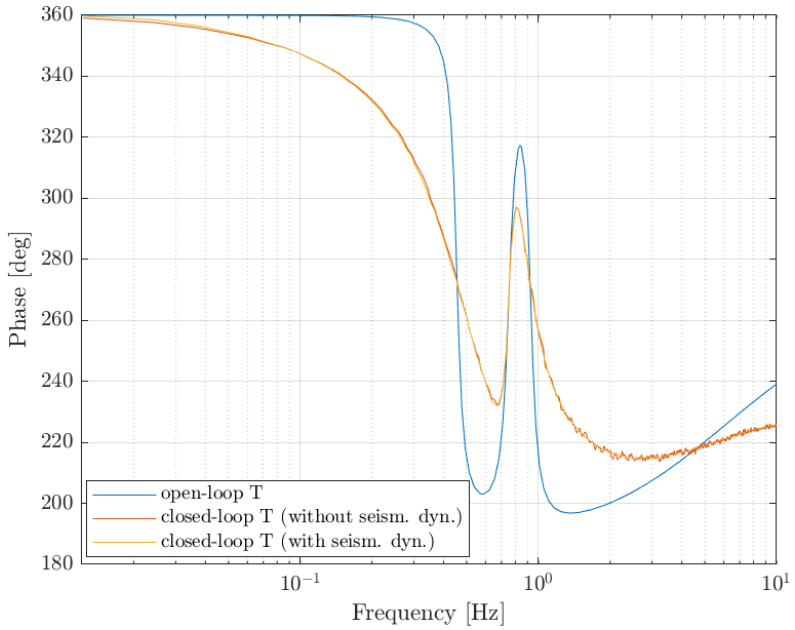

Figure 3.31: Phase plot, comparison between open-loop and closed-loop transmissibilities ($g = 824.83$, $k = 0.00045$): transmissibility from a_0 to a_1

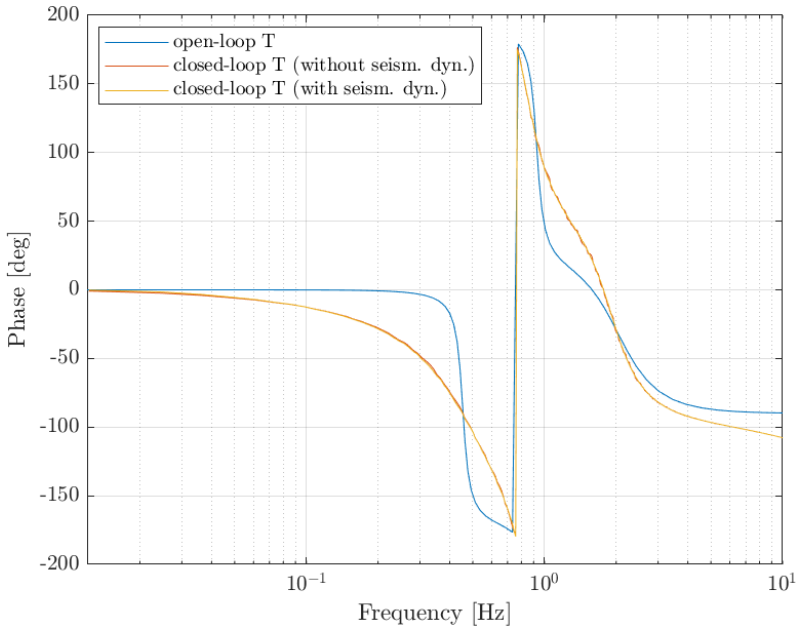

Figure 3.32: Phase plot, comparison between open-loop and closed-loop transmissibilities ($g = 824.83$, $k = 0.00045$): transmissibility from a_0 to a_2

If instead larger values of the gain or larger excitation levels were considered, for which saturation would be reached, the magnitude and phase curves would become more noisy. This happens because if the actuator reaches saturation, a nonlinear term is added. The fact that actuators reach saturation or not depends on the gain and on the velocity, according to the definition of the control force with sky-hook damping (eq. (3.42)). In turn, the velocity depends on the excitation level since the output of $P_1(s)$ is the acceleration and its input is indeed the base excitation.

Feedforward Control: Description

The FF control has the aim of furtherly flattening the resonance peaks until an attenuation of $-20\ dB$. The transfer function of the FF block is found by imposing the ratio $\frac{a_1(s)}{a_0(s)}$ equal to zero and hence by setting to zero the numerator of the transmissibility function from a_1 to a_0 (eq. (3.39)). It is important to underline the fact that it is necessary to consider the modal damping and not the Rayleigh one when the FF control is added, since in its TF the coefficient c_1 is present. In fact, if the equations with the modal damping are considered, it results that:

$$P_1(s) + S_1(s)FF(s) = 0 \tag{3.45}$$

$$S_1(s)FF(s) = -P_1(s) \tag{3.46}$$

$$FF(s) = -S_1^{-1}(s)P_1(s) \tag{3.47}$$

Since $P_1(s) = (sc_1 + k_1)Q_1(s)$ and $S_1(s) = s^2Q_1(s)$, it results that:

$$FF(s) = -s^{-2}Q_1^{-1}(s)(sc_1 + k_1)Q_1(s) = -s^{-2}(sc_1 + k_1) \tag{3.48}$$

From here, the ideal FF control with perfect cancellation results to be:

$$FF(s) = -\frac{sc_1 + k_1}{s^2} = -\frac{1}{s}\left(c_1 + \frac{k_1}{s}\right) \tag{3.49}$$

From eq. (3.49) it comes the consideration that the parameters c_1 and k_1 assume the role of a proportional and a derivative gain, respectively, and hence the FF is written under the form of a Proportional-Integral (PI) controller. Anyway, to avoid any possible drift

and actuator saturation, the pure integrators in the previous expression are replaced as follows:

$$\frac{1}{s} \rightarrow \frac{1}{s+\alpha} \tag{3.50}$$

where α needs to be tuned with a value one decade below the first resonance frequency, as for the frequency ω in the pseudo-integrator seen before (eq. (3.41)).
As a result, eq. (3.49) becomes:

$$FF(s) = -\frac{1}{s+\alpha}\left(c_1 + \frac{k_1}{s+\alpha}\right) \tag{3.51}$$

Note that k_1 and c_1 are not known exactly, but only a non-perfect estimate of the parameters is available since they have been estimated by comparing dynamic responses. Hence:

$$k_1 \rightarrow \hat{k}_1 \tag{3.52}$$

$$c_1 \rightarrow \hat{c}_1 \tag{3.53}$$

Therefore, the FF control is given by:

$$FF(s) = -\frac{1}{s+\alpha}\left(\hat{c}_1 + \frac{\hat{k}_1}{s+\alpha}\right) \tag{3.54}$$

The effects of the uncertainties on the estimates of k_1 and c_1 can be simulated as:

$$0.9\ k_1 \leq \hat{k}_1 \leq 1.1\ k_1 \tag{3.55}$$

$$0.9\ c_1 \leq \hat{c}_1 \leq 1.1\ c_1 \tag{3.56}$$

Combined FB and FF Control: Results

At first, no saturation is considered in the simulations and the FB gain is set to 824.83, which was the largest acceptable gain when the FB control alone was implemented and

saturation was considered. Moreover, the parameters $\hat{c}_1$ and $\hat{k}_1$ are for the moment taken as fixed and assume the value of their perfect estimates when considering the modal damping, hence: $\hat{c}_1{=}c_1$ and $\hat{k}_1{=}k_1$. Figure 3.33 and fig. 3.34 display the effects of the addition of the FF control when different values of the α parameter are considered, before imposing the saturation constraint.

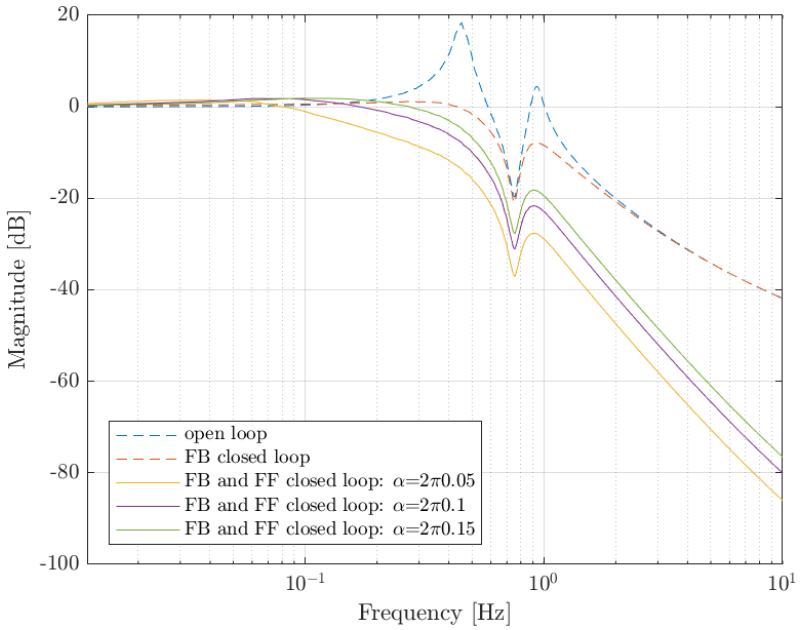

Figure 3.33: Closed-loop transmissibility from a_0 to a_1: effect of the FF control

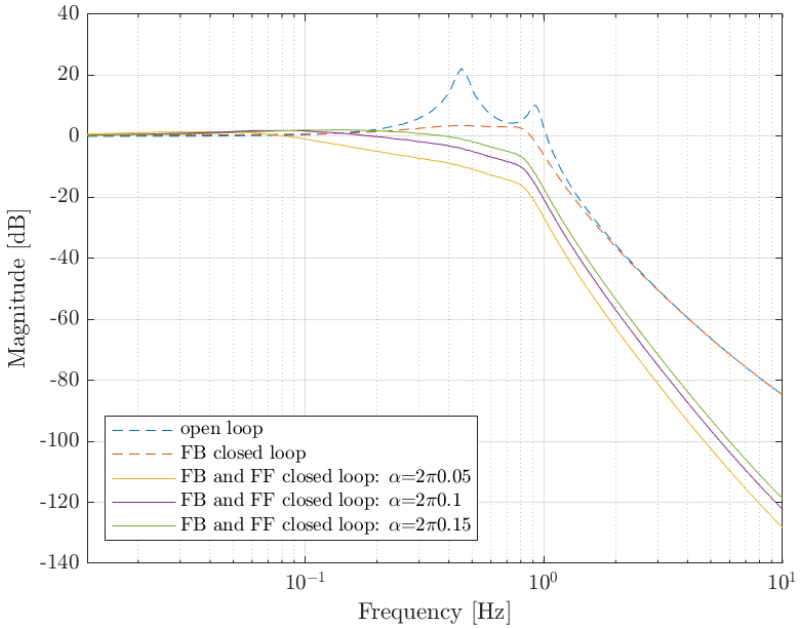

Figure 3.34: Closed-loop transmissibility from a_0 to a_2: effect of the FF control

From fig. 3.33 and fig. 3.34 it is evident that the introduction of the FF control allows to improve the roll-off rate at high frequencies with respect to the case in which only the FB is considered. Moreover, it results that the FF control can cause a visible improvement in the damping of the resonance peaks. The attenuation gets better the more α decreases, but this requires a larger control force to the actuator, as it can be seen in fig. 3.35.

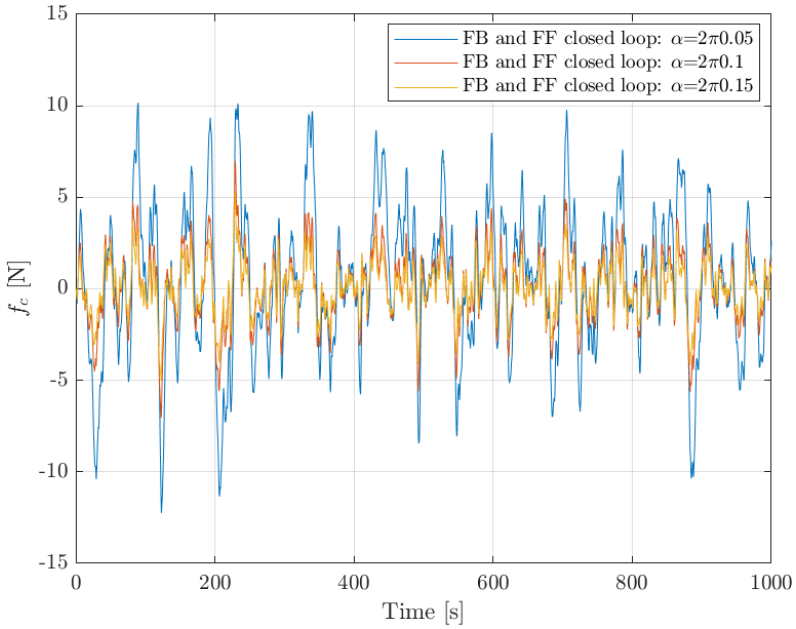

Figure 3.35: Actuator control force: FB and FF

Introduce now the presence of the saturation of the actuator at $\pm 3\ N$. Since in the FB the maximum acceptable gain before saturation has been considered, it results that no contribution to the control force is left to the FF control. To respect the saturation constraint, it is necessary to lower the gain of the FB loop and find a compromise between the performances granted by the FB and the ones of the FF control. Some simulation trials have been made considering to respect the following constraints:

- Granting an attenuation of the resonance peaks of at least $-20\ dB$;
- Requiring a control force lower than the saturation limit of $\pm 3\ N$.

Unfortunately, there is no combination of the values of the gain and of the α parameter that can grant the required attenuation of the peaks by providing, at the same time, a control force lower than saturation. For this reason, it is necessary to relax one of the two constraints: either some performances are given up or it is required a larger control force to the actuators by exceeding the saturation limit. The two cases are distinguished

in the following.

Respecting the Saturation Constraint

Since it is not provided any information on the exploitation possibility of the actuator, its saturation should be considered at $\pm 3\ N$, which is the value present on the datasheet. However, this saturation level leads to the fact that, even at the top of the control, an attenuation of $-20\ dB$ cannot be reached.
The FF addition leads to an increase in the roll-off rate at higher frequencies due to the choice of the α parameter. For the saturation limit to be respected, it is necessary to find a compromise between the increase in the FB gain and the decrease in the α parameter of the FF. The best results obtained respecting the saturation limit are shown in fig. 3.36 and fig. 3.37, with $g = 600$ and $\alpha = 2\pi 0.27$.

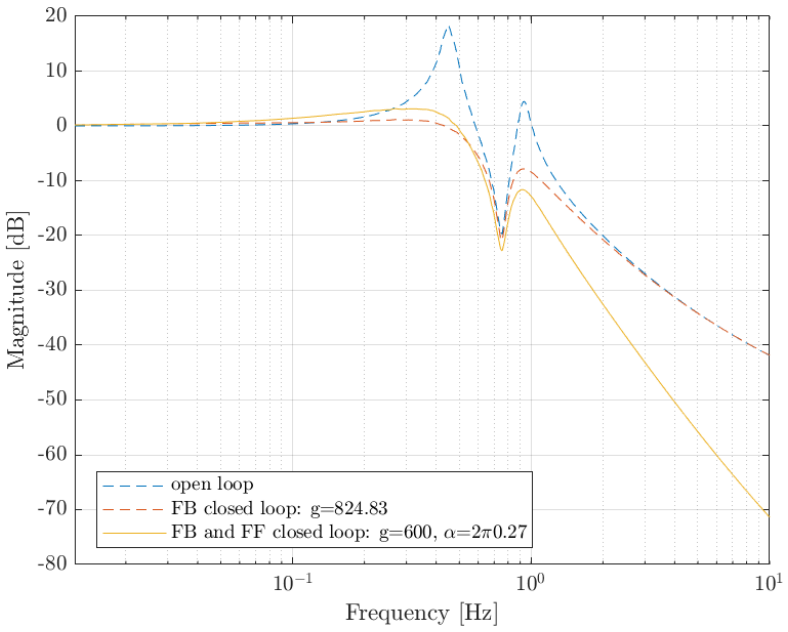

Figure 3.36: Closed-loop transmissibility from a_0 to a_1: FB control with $g = 600$ and FF control with $\alpha = 2\pi 0.27$

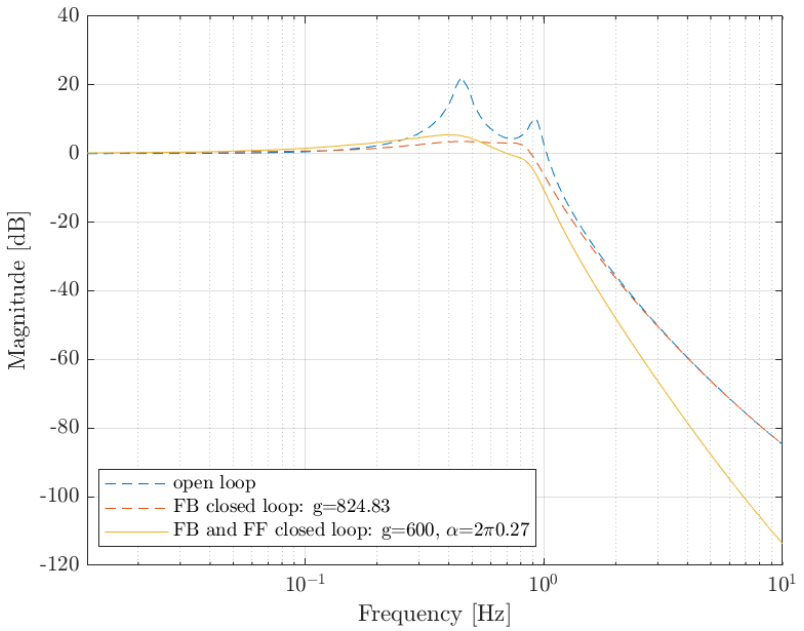

Figure 3.37: Closed-loop transmissibility from a_0 to a_2: FB control with $g = 600$ and FF control with $\alpha = 2\pi 0.27$

As it results from the figures above, the attenuation of the second peak is improved for both the transmissibilities, while the attenuation of the first peak has worsened with respect to the case of FB control alone. This is due to the chosen value of the α parameter, which is the cutoff frequency of the FF. This problem could be solved by decreasing the value of α, but the issue is that in this way the saturation limit would not be respected anymore. If at the same time the gain was decreased, it would not be possible anyway to have an improvement in the attenuation both of the first and of the second peak.
The attenuation levels provided in the case of $g = 600$ and $\alpha = 2\pi 0.27$ are displayed in table 3.4 and table 3.5, where the attenuations are defined as the difference between the magnitude of the resonance peak and the magnitude which would be obtained if the desired attenuation of $-20\ dB$ was obtained.

Table 3.4: Attenuation of the peaks: transmissibility from a_0 to a_1

Gain	α	**First peak** $(0.45Hz)$ **[dB]**	**Second peak** $(0.93Hz)$ **[dB]**
0	\	20	20
824.83	\	1.3923	7.7507
600	$2\pi 0.27$	3.6625	5.3265

Table 3.5: Attenuation of the peaks: transmissibility from a_0 to a_2

Gain	α	**First peak** $(0.45Hz)$ **[dB]**	**Second peak** $(0.93Hz)$ **[dB]**
0	\	20	20
824.83	\	1.3923	7.7507
600	$2\pi 0.27$	3.6623	5.3279

As it results from table 3.4 and table 3.5, the first peak is less attenuated with respect to the case of FB control alone (table 3.2 and table 3.3). For this reason, in the case in which it is desired to respect the saturation limit of $\pm 3\ N$, the best performance is obtained with FB control alone without the addition of a FF control.

Exceeding the Saturation Constraint

In order to obtain a saturation of $-20\ dB$, it is considered to increase the maximum control force required to the actuator. In fact, if the actuator could be exploited more than its actual saturation limit, it would be possible to prioritize the performances over the saturation constraint. Simulations have shown that the first saturation value which allows to obtain an attenuation of $-20\ dB$ is $\pm 4.3\ N$. In this way, the actuators are stressed 143.33% of their nominal saturation value, which is anyway acceptable in practical terms. Under this new saturation constraint, the gain and the α parameter which grant a larger attenuation than $-20\ dB$ are 824.83 (equal to the gain with FB alone) and $2\pi 0.209$, respectively. The resulting transmissibility functions are represented in fig. 3.38 and fig. 3.39.

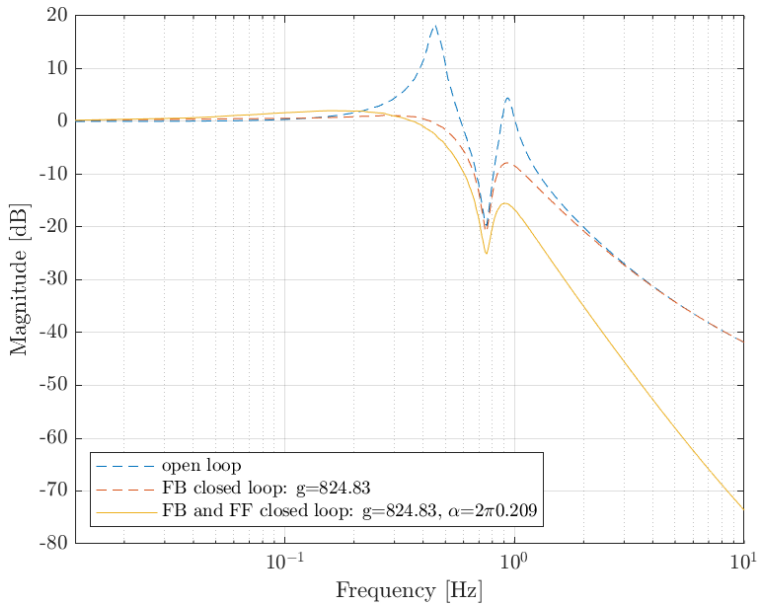

Figure 3.38: Closed-loop transmissibility from a_0 to a_2: FB and FF control with g=824.83 and $\alpha = 2\pi 0.209$

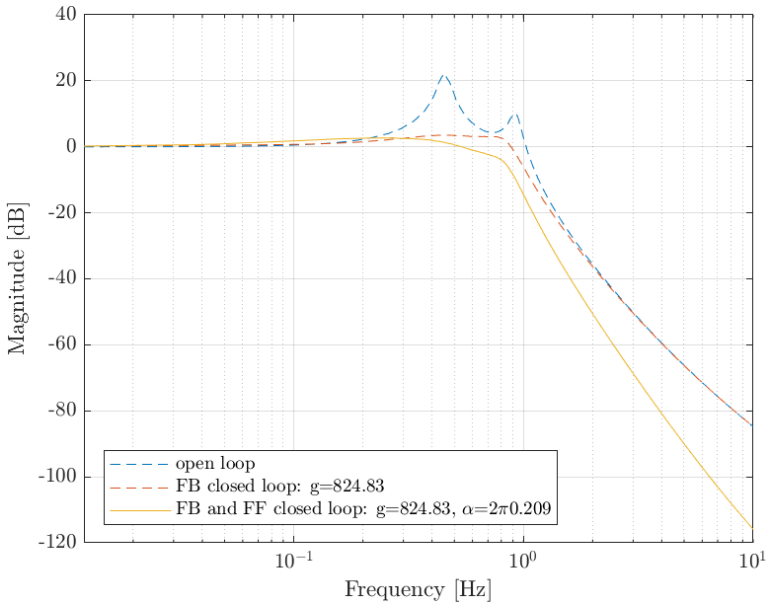

Figure 3.39: Closed-loop transmissibility from a_0 to a_2: FB and FF control with g=824.83 and $\alpha = 2\pi 0.209$

The required control force is represented in fig. 3.40, which shows the overcome of the saturation limit since $\pm 4.3\ N$ are reached.

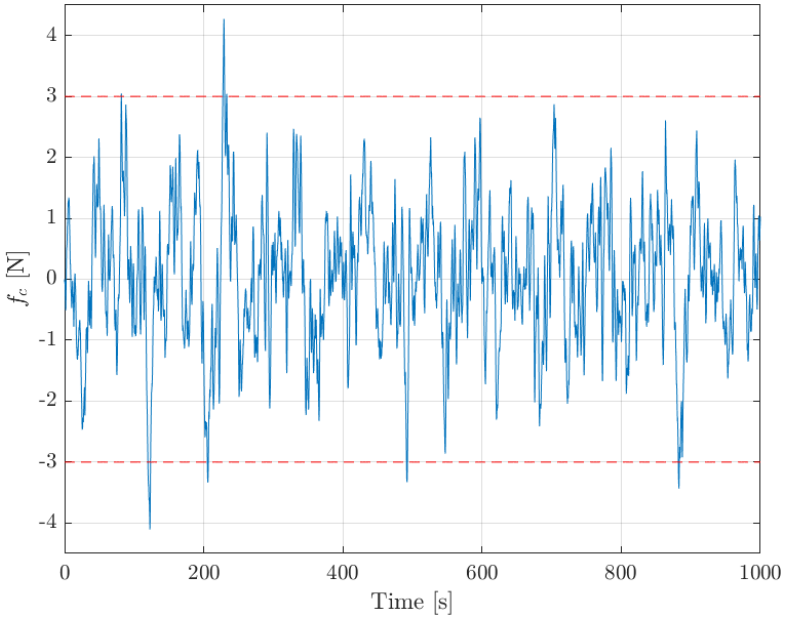

Figure 3.40: Actuator control force: FB and FF control with g=824.83 and $\alpha = 2\pi 0.209$

From fig. 3.38 and fig. 3.39 it results that the attenuation of the peaks is considerably larger than the one obtained with the FB control alone. Table 3.6 and table 3.7 show the difference between the peak and the desired attenuation of $-20\ dB$. It results that the attenuation of $-20\ dB$ is achieved, since the values related to the control with FB and FF are negative.

Table 3.6: Attenuation of the peaks: transmissibility from a_0 to a_1

Gain	α	**First peak** $(0.45Hz)$ **[dB]**	**Second peak** $(0.93Hz)$ **[dB]**
0	\	20	20
824.83	\	1.3923	7.7507
824.83	$2\pi 0.209$	-0.8518	-0.0131

Table 3.7: Attenuation of the peaks: transmissibility from a_0 to a_2

Gain	α	**First peak** $(0.45Hz)$ **[dB]**	**Second peak** $(0.93Hz)$ **[dB]**
0	\	20	20
824.83	\	1.2179	6.9689
824.83	$2\pi 0.209$	-0.8564	-0.0755

Figure 3.38 and fig. 3.39 show that at lower frequencies the FRF with FF control rises up. This issue is not due to the wind-up phenomenon, since saturation is not reached, and it

is even not due to the waterbed effect, since no unstable poles nor zeros are present. This overshoot phenomenon is inevitable in the inertial FB systems because the amplification near the unity gain points happens for phase margin less than 60^o. To reduce the effect of the overshoots at the unity gain points on the stability of the system, the phase margin should be increased. This could be achieved thanks to a phase lag and a phase lead compensators.

- The **phase lag** is addressed to the low frequency unity gain point. Added to the FB compensator, the phase lag serves to increase the compensation gain which results in decreasing the closed loop magnitude (overshoots) near the low frequency unity gain point.
- The **phase lead** is addressed to the high frequency unity gain point. Added at high frequency unity gain point, the phase lead shifts the phase of the closed-loop away from the line of -180^o which increases the phase margin and assures higher stability conditions. [17]

In the following, it is necessary to verify that the **uncertainties** on the values of $\hat{k}_1$ and $\hat{c}_1$ still allow to respect the required performances and the saturation constraint. Hence, a sensitivity analysis to the possible variations of $\hat{k}_1$ and $\hat{c}_1$ is conducted, by keeping fixed the values of the gain and of the parameter α at 824.83 and $2\pi 0.209$, respectively. The effects of uncertainties on the estimates of k_1 and c_1 are simulated as in eq. (3.57) and eq. (3.58).

$$0.9\ k_1 \leq \hat{k}_1 \leq 1.1\ k_1 \tag{3.57}$$

$$0.9\ c_1 \leq \hat{c}_1 \leq 1.1\ c_1 \tag{3.58}$$

First, it is considered to vary only the $\hat{k}_1$ parameter and the results are represented in fig. 3.41 and fig. 3.42.

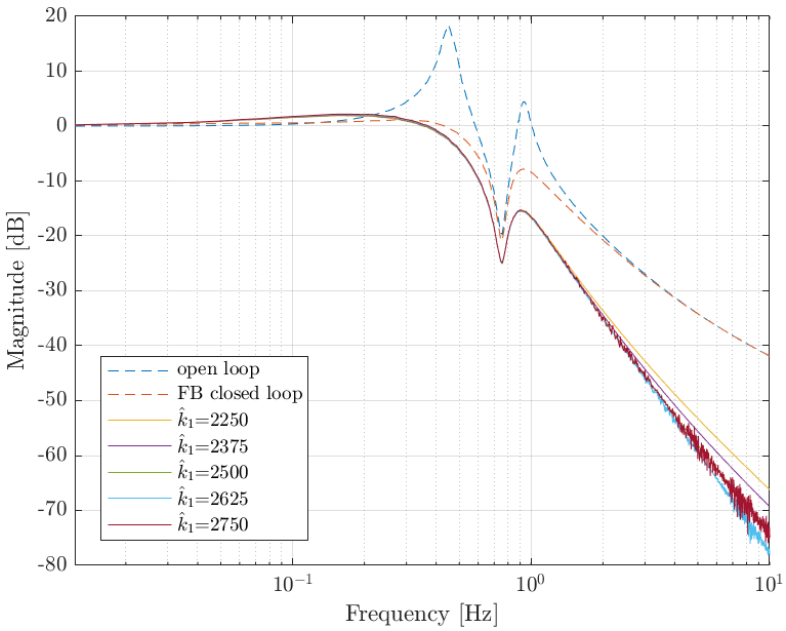

Figure 3.41: FB and FF closed-loop transmissibility from a_0 to a_1: $0.9\ k_1 \leq \hat{k}_1 \leq 1.1\ k_1$

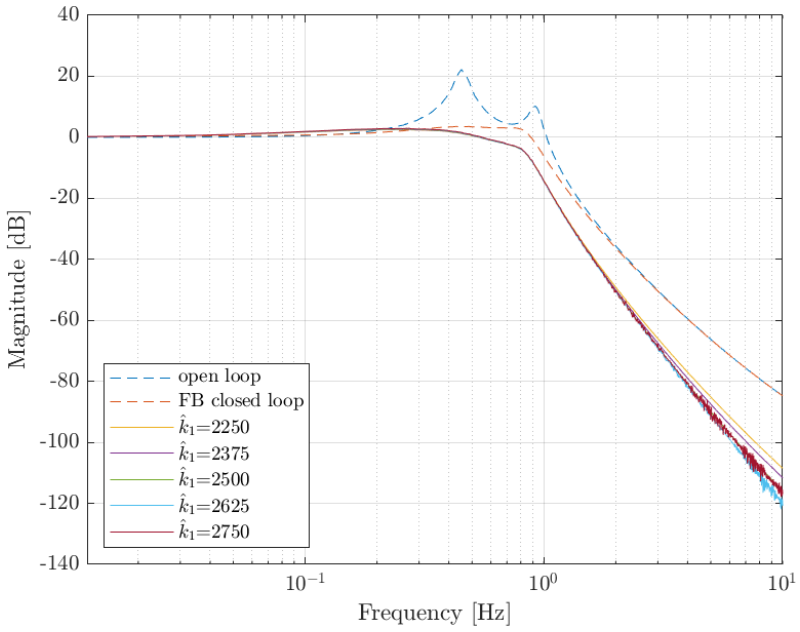

Figure 3.42: FB and FF closed-loop transmissibility from a_0 to a_2: $0.9\ k_1 \leq \hat{k}_1 \leq 1.1\ k_1$

From fig. 3.41 and fig. 3.42, it can be noted that at high frequencies some noise appears for values of $\hat{k}_1$ larger than the nominal one. This is due to the fact that saturation is reached in those cases, and the oscillations are the nonlinear terms introduced. As an observation, the fact that saturation is reached does not generate a relevant increase in the rise-up of the magnitude of the FRF at lower frequencies, hence the wind-up phenomenon does not

have a consistent effect. Saturation is reached for values of $\hat{k}_1$ larger than the nominal one because the employed α parameter was the limit value that could at the same time guarantee the required performances and respect the saturation limit, while maximising the value of the gain. The issue of the oscillations at higher frequencies can be solved in one of the following ways:

- by reducing the ranges of possible $\hat{k}_1$;
- by giving up on some attenuation, allowing a worsening of the performance;
- by requiring more control force to the actuators.

The attenuation granted by the range of values of $\hat{k}_1$ is reported in table 3.8 and in table 3.9. It is highlighted in red the case obtained with the nominal value of $\hat{k}_1$.

Table 3.8: Attenuation of the peaks (uncertain $\hat{k}_1$): transmissibility from a_0 to a_1

$\hat{k}_1$ $[\frac{N}{m}]$	**First peak** $(0.45Hz)$ **[dB]**	**Second peak** $(0.93Hz)$ **[dB]**
2250	-0.9581	0.1945
2375	-0.9162	0.0425
2500	-0.8518	-0.0131
2625	-0.7655	0.0134
2750	-0.6600	0.0816

Table 3.9: Attenuation of the peaks (uncertain $\hat{k}_1$): transmissibility from a_0 to a_2

$\hat{k}_1$ $[\frac{N}{m}]$	**First peak** $(0.45Hz)$ **[dB]**	**Second peak** $(0.93Hz)$ **[dB]**
2250	-0.9627	0.1321
2375	-0.9209	-0.0198
2500	-0.8564	-0.0755
2625	-0.7702	-0.0492
2750	-0.6649	0.0169

From table 3.8 and table 3.9 it results that the required performances are obtained only when the nominal value of $\hat{k}_1$ is involved. Otherwise, both for smaller and larger values of $\hat{k}_1$, the second peak is not attenuated of at least $-20\ dB$ in the transmissibility from a_0 to a_1. Hence, even if for values of $\hat{k}_1$ lower than the nominal one saturation is not reached, there is however the issue that the requirement on the attenuation of $-20\ dB$ is not fulfilled. Anyway, since the main goal is to attenuate the micro vibrations transmitted to the MPLAT, it is enough to guarantee an attenuation of at least $-20\ dB$ in the

transmissibility from a_0 to a_2. Thus, acceptable values of $\hat{k}_1$ become the ones lower or equal to the nominal k_1 showing a negative value for both the peaks in table 3.9.

Now, the nominal value of $\hat{k}_1$ is considered as fixed, while the parameter $\hat{c}_1$ is varied in the interval between 0.9 c_1 and 1.1 c_1. The results of the effect of the sensitivity analysis to the uncertainties of the parameter $\hat{c}_1$ are shown in fig. 3.43 and fig. 3.44.

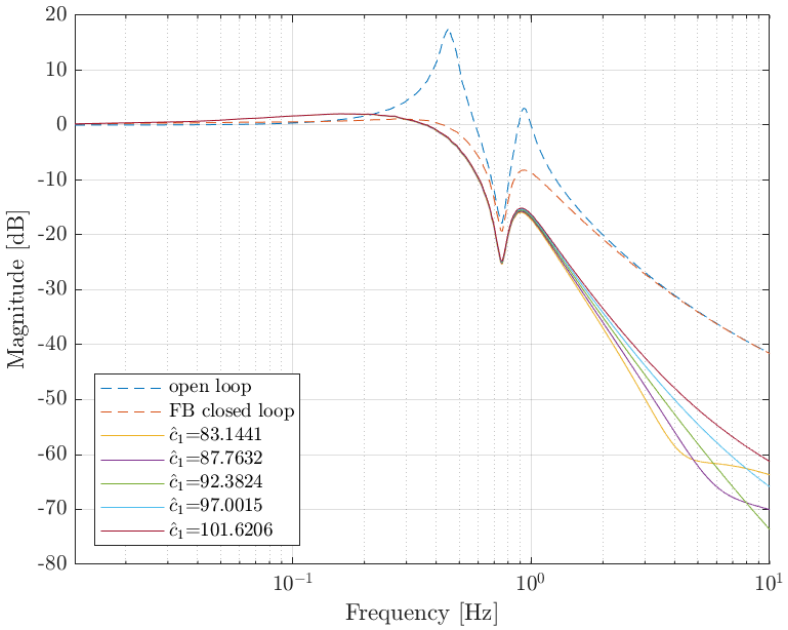

Figure 3.43: FB and FF closed-loop transmissibility from a_0 to a_1: $0.9\, c_1 \leq \hat{c}_1 \leq 1.1\, c_1$

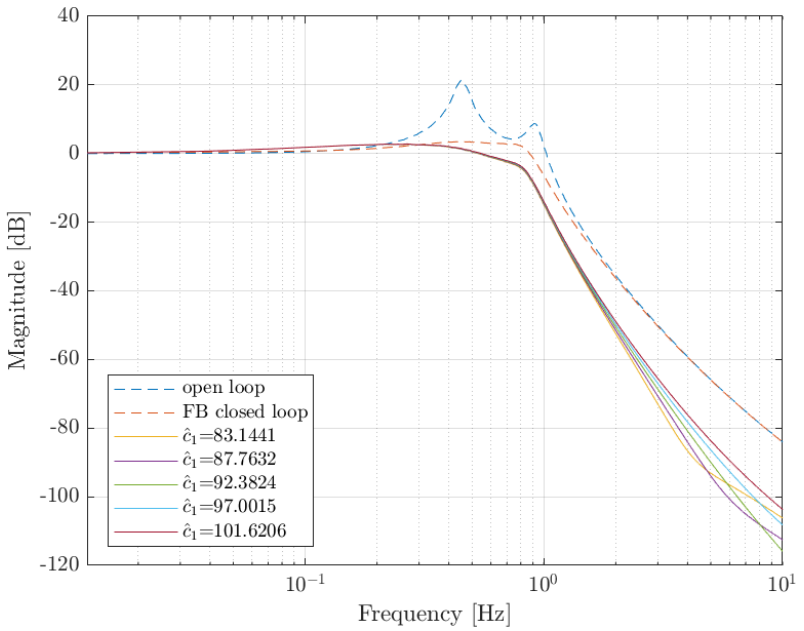

Figure 3.44: FB and FF closed-loop transmissibility from a_0 to a_2: $0.9\ c_1 \leq \hat{c}_1 \leq 1.1\ c_1$

As it can be appreciated from fig. 3.43 and fig. 3.44, saturation is not reached when $\hat{k}_1$ is kept fixed and $\hat{c}_1$ is varied. In fact, no oscillations at higher frequencies are present. The provided attenuation is displayed in table 3.10 and table 3.11.

Table 3.10: Attenuation of the peaks: transmissibility from a_0 to a_1

$\hat{c}_1$ $[\frac{Ns}{m}]$	**First peak** $(0.45Hz)$ **[dB]**	**Second peak** $(0.93Hz)$ **[dB]**
83.1441	-0.9518	-0.4254
87.7632	-0.9016	-0.2170
92.3824	-0.8518	-0.0131
97.0015	-0.8019	0.1869
101.6206	-0.7525	0.3823

Table 3.11: Attenuation of the peaks: transmissibility from a_0 to a_2

$\hat{c}_1$ $[\frac{Ns}{m}]$	**First peak** $(0.45Hz)$ **[dB]**	**Second peak** $(0.93Hz)$ **[dB]**
83.1441	-0.9565	-0.4874
87.7632	-0.9063	-0.2791
92.3824	-0.8564	-0.0755
97.0015	-0.8066	0.1246
101.6206	-0.7571	0.3199

From table 3.10 and table 3.11, it results that the required attenuation is obtained for values of $\hat{c}_1$ smaller or equal to the nominal one given by the modal damping. For larger values of $\hat{c}_1$, an attenuation of at least $-20\ dB$ is not achieved anymore.

To sum up, it is possible to define the acceptable ranges of $\hat{k}_1$ and $\hat{c}_1$ in order to grant the fulfillment of the performance and to respect the new saturation constraint of $\pm 4.3\ N$.
The range of $\hat{k}_1$ is defined as follows:

- to avoid saturation: $0.9\ k_1 \leq \hat{k}_1 \leq k_1$;
- to grant an attenuation of at least $-20\ dB$: $0.95\ k_1 \leq \hat{k}_1 \leq 1.05\ k_1$.

Hence, the acceptable range of $\hat{k}_1$ is $0.95\ k_1 \leq \hat{k}_1 \leq k_1$.
On the other hand, the range of $\hat{c}_1$ is defined as follows:

- to avoid saturation: any value of $\hat{c}_1$ is acceptable;
- to grant an attenuation of at least $-20\ dB$: $0.9\ c_1 \leq \hat{c}_1 \leq c_1$.

Thus, all values in the range $0.9\ c_1 \leq \hat{c}_1 \leq c_1$ are acceptable.

3.1.2. Control of the Condensed Craig-Bampton Model: VIBISIO

The control of the VIBISIO designed for the 2DoF model has been then extended to the condensed CB model. It has been decided to apply the designed control which exceeds the saturation limit of $\pm 3\ N$, but is able to achieve an attenuation of $-20\ dB$. Such a control consists of FB and FF, where the FB is a skyhook damper with $g = 824.83$, and in the FF the α parameter is equal to $2\pi 0.209$.

Description

The control system designed for the 2DoF model can now be extended to the condensed CB one. For this control design, the condensed CB model with LM is considered. Despite the 2DoF model was described by transfer functions, the CB one is represented in SS form, since the number of DoFs is much larger. The condensed CB model expressed in SS form becomes:

$$\underbrace{\begin{Bmatrix}\dot{\mathbf{u}}_{cond}\\ \ddot{\mathbf{u}}_{cond}\end{Bmatrix}}_{\dot{\mathbf{x}}(t)} = \underbrace{\begin{bmatrix}\mathbf{0} & \mathbf{I}\\ -\mathbf{M}_{cond}^{-1}\mathbf{K}_{cond} & -\mathbf{M}_{cond}^{-1}\mathbf{Damp}_{cond}\end{bmatrix}}_{\mathbf{A}}\underbrace{\begin{Bmatrix}\mathbf{u}_{cond}\\ \dot{\mathbf{u}}_{cond}\end{Bmatrix}}_{\mathbf{x}(t)} + \underbrace{\begin{bmatrix}\mathbf{0}\\ \mathbf{M}_{cond}^{-1}\mathbf{P_d}\end{bmatrix}}_{\mathbf{B}_d}\underbrace{a_0}_{d(t)} + \underbrace{\begin{bmatrix}\mathbf{0}\\ \mathbf{M}_{cond}^{-1}\mathbf{P_u}\end{bmatrix}}_{\mathbf{B}_u}\underbrace{f_c}_{u(t)} \tag{3.59}$$

The vectors $\mathbf{P_d}$ and $\mathbf{P_u}$ are associated to the disturbance and to the control input respectively.

$$\mathbf{P_d} = zeros(14,1) \rightarrow \mathbf{P_d}(3) = m_0 \tag{3.60}$$

$$\mathbf{P_u} = zeros(14,1) \rightarrow \mathbf{P_u}(2) = 1; \mathbf{P_u}(3) = -1; \tag{3.61}$$

The measured output is the velocity $\dot{u}_1(t)$, which needs to be employed in the FB. The performance vector $\mathbf{z}(t)$ represents the variables that it is desired to monitor. For completeness, it has been decided to retrieve the velocities and accelerations of all the DoFs. Hence, the performance vector $\mathbf{z}(t)$ coincides with the derivative of the state $\dot{\mathbf{x}}(t)$.

The block diagram of the **open-loop** control system is the following:

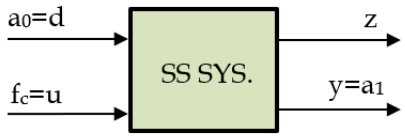

Figure 3.45: Open-loop control system of the CB model

The block diagram of the **closed-loop** control system of the CB model is the following:

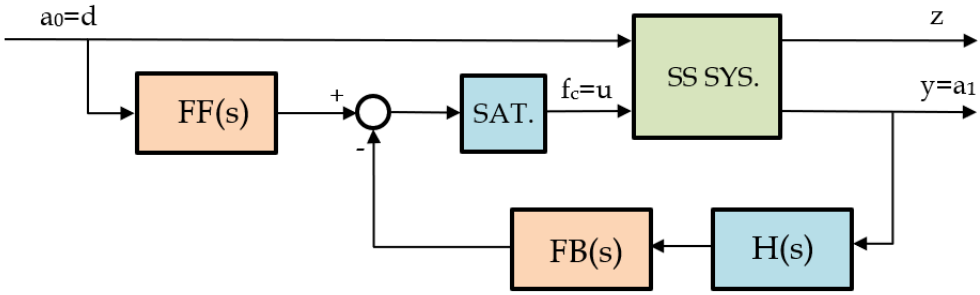

Figure 3.46: Closed-loop control system of the CB model

The FB and FF transfer functions are the ones obtained for the equivalent 2DoF model. The objective is to prove that the VIBISIO control designed on the equivalent model is suitable also for the CB one. To this aim, the 14DoF model is employed, which is more detailed with respect to the 2DoF one, since it contains also 11 modal DoFs. The VIBISIO control has been applied to the 14DoF system, defined both in state space form and with the inversion of the dynamics matrix.
The frequency response is retrieved thanks to the command *tfestimate* from the time histories of the accelerations obtained from the Simulink® simulations. This command estimates the transfer function of the system using Welch's averaged, modified periodogram method and receives as inputs:

- the time histories of the acceleration of the base and of the VIBISIO or of the MPLAT, depending on the transfer function which is desired to retrieve;
- Hanning window;
- number of DFT points equal to 8192;
- sampling frequency of 100 Hz.

The output is the quotient of the Cross Power Spectral Density of the acceleration time history of the base and the acceleration time history of the VIBISIO or of the MPLAT, and the Power Spectral Density of the time history of the acceleration of the base.

After having obtained the transfer functions $H(j\omega)$ by means of *tfestimate*, the Bode magnitude diagrams related to the VIBISIO and the MPLAT are retrieved with eq. (3.62).

$$H_{dB} = 20\ log_{10} \mid H(j\omega) \mid \tag{3.62}$$

In fig. 3.47 and fig. 3.48 are reported the Bode diagrams of the open-loop responses of the VIBISIO and of the MPLAT, respectively. The red curve represents the FRF computed in MATLAB®, while the other two correspond to the frequency responses computed starting from the temporal histories of the accelerations obtained in Simulink®. The blue curve is obtained with the system defined in state space form, while the green one is retrieved with the inversion of the dynamics matrix.

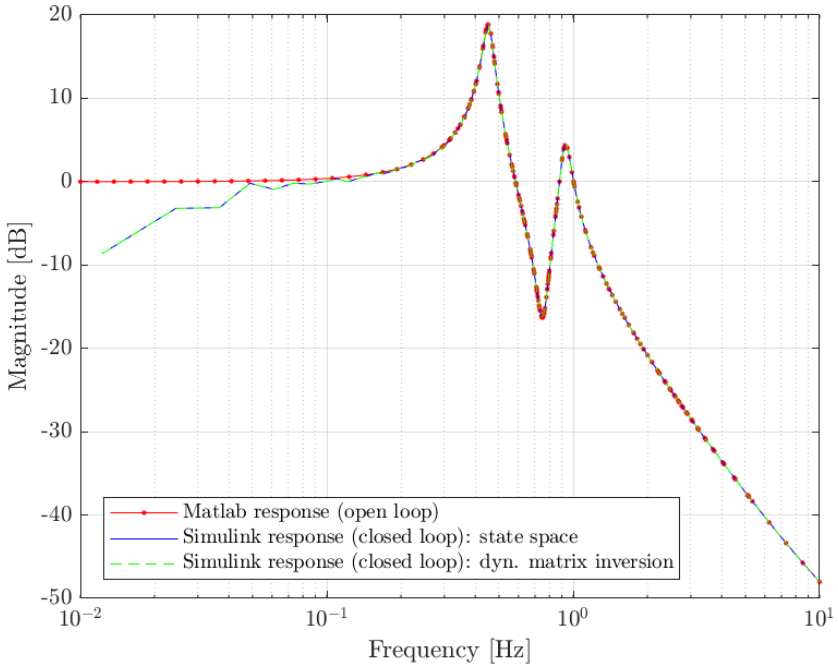

Figure 3.47: VIBISIO open loop response

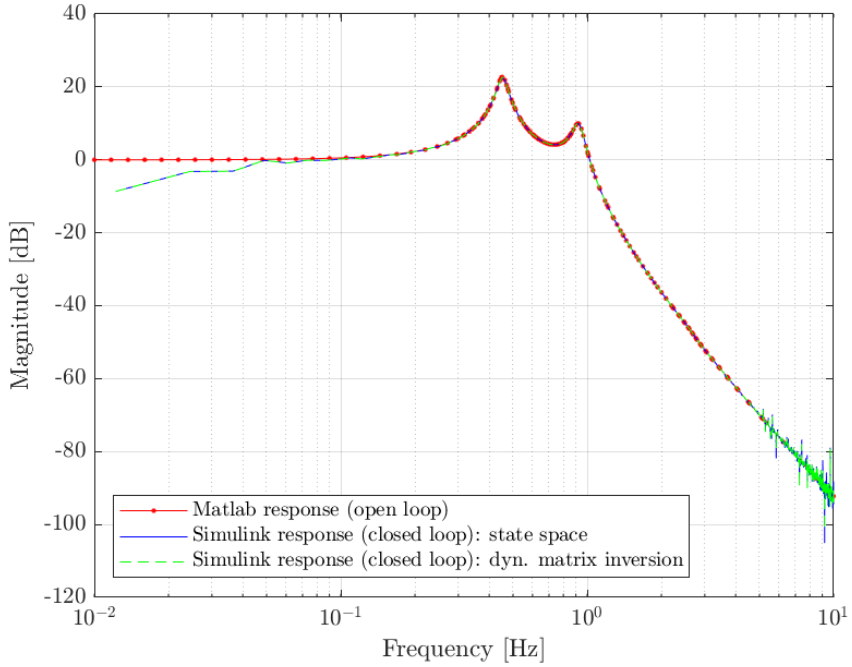

Figure 3.48: MPLAT open loop response

Figure 3.47 and fig. 3.48 show that the Bode diagrams retrieved from the Simulink® time histories with a random load well overlap with the FRFs obtained in MATLAB®.
The frequency responses obtained starting from the Simulink® simulation are in the case of the condensed CB model less noisy with respect to the full CB one, also thanks to the fact that the simulation can last longer (1000 s) without meeting any singularity. However, due to signal processing, the responses still show some noise, in particular at higher frequencies, but it is irrelevant and definitely acceptable. Moreover, the discrepancy at lower frequencies is due to the reconstruction of the FRF from the time domain.

Results

The control of the VIBISIO performed on the 14DoF model is able to attenuate the resonance peaks, as in the equivalent 2DoF model. The Bode diagram and the FRF related to the acceleration of the VIBISIO, divided by the base acceleration, are displayed in fig. 3.49 and fig. 3.50.

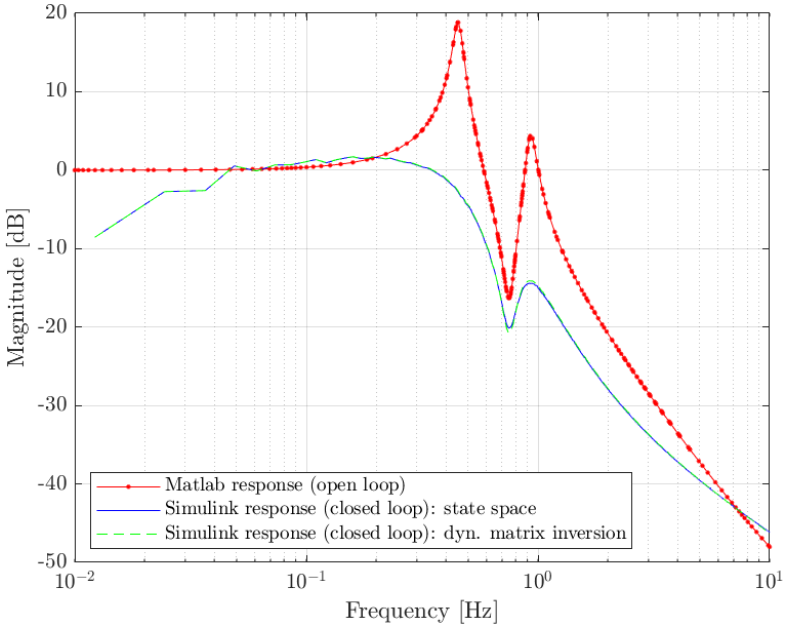

Figure 3.49: Control of the VIBISIO (FB and FF) in the 14DoF system: Bode diagram related to the VIBISIO

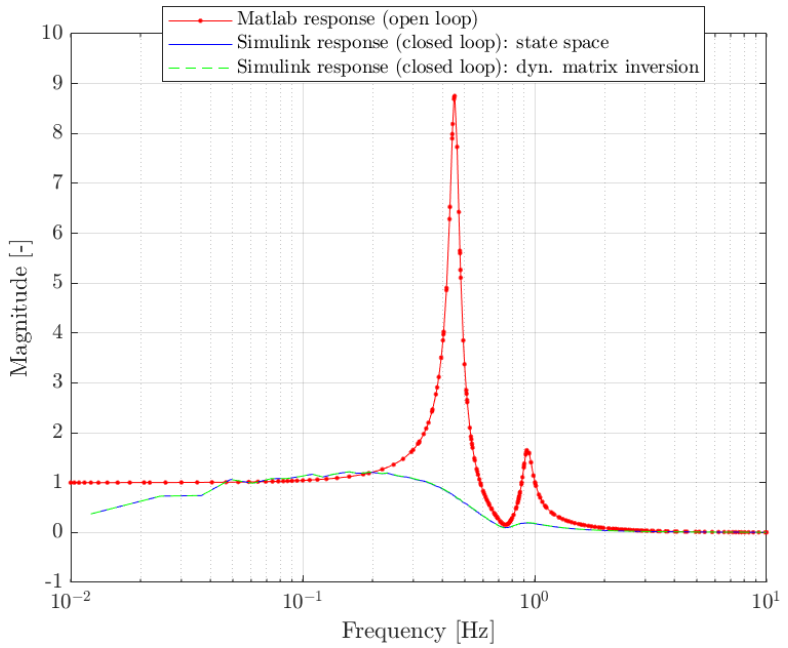

Figure 3.50: Control of the VIBISIO (FB and FF) in the 14DoF system: FRF related to the VIBISIO

The Bode diagram and the FRF related to the acceleration of the MPLAT, divided by the base acceleration, are displayed in fig. 3.51 and fig. 3.52.

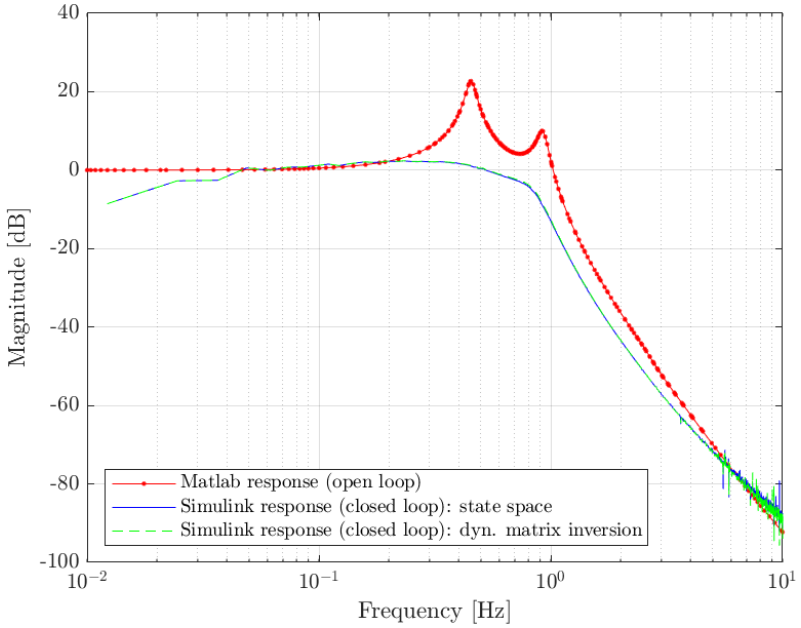

Figure 3.51: Control of the VIBISIO (FB and FF) in the 14DoF system: Bode diagram related to the MPLAT

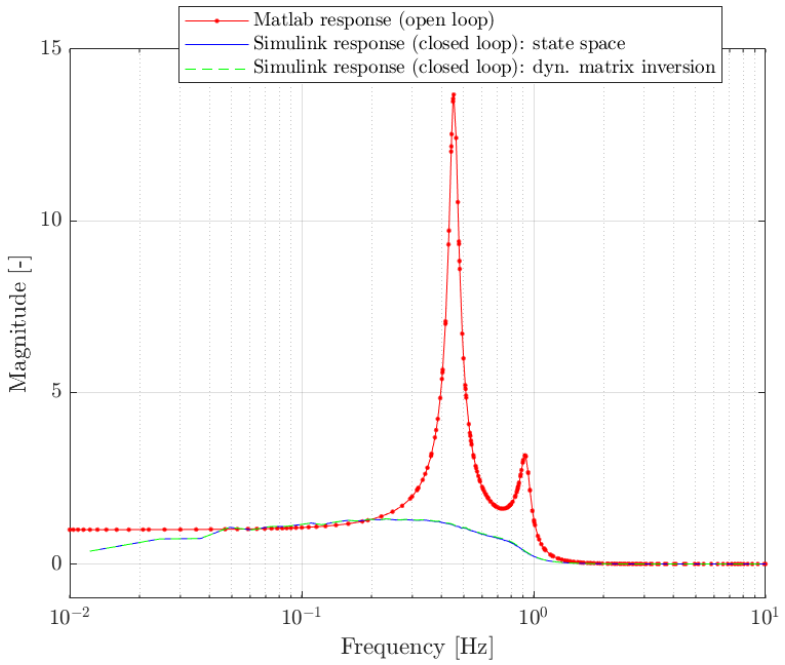

Figure 3.52: Control of the VIBISIO (FB and FF) in the 14DoF system: FRF related to the MPLAT

3.2. Measurement Platform Control

After having designed the control for the VIBISIO, the focus is displaced to the control of the MPLAT.
In sensor mode, using position sensors measuring the distance between the isolation platform and measurement platform, the measurement platform is held in null-displacement to the isolation platform. The measurement platform control computes the feedback force required to counteract any displacement of the platform caused by a specimen exerted force. The drive signal from the controller to the force actuator gives the measure of the force. Additionally, an extra damping term can be added to the platform control force to help the high-frequency control of the measurement platform.
The control for the MPLAT has been designed with the H-infinity technique. The corresponding MATLAB® command is $hinfsyn$, which calculates the H-infinity optimal controller **K** for the LTI plant **P**.
The H-infinity synthesis is used to synthesize a controller to achieve stabilization with guaranteed performance. The H-infinity controller is designed by simultaneously shaping the frequency responses for tracking and disturbance rejection, noise reduction and robustness, and controller effort. The control problem is expressed as a mathematical optimization problem and then the controller that solves this optimization is found.
The process has to be represented according to the following standard configuration:

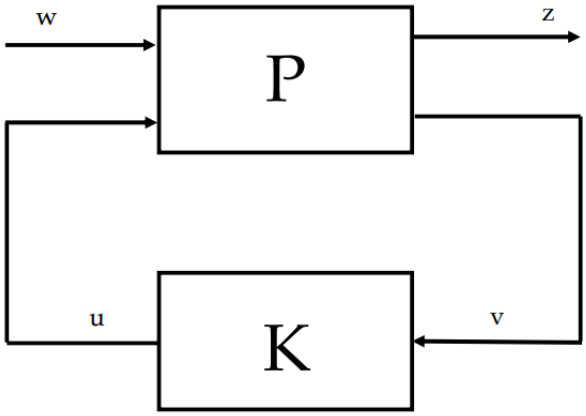

Figure 3.53: Standard configuration of H-infinity control

The plant **P** has:

- two inputs: the exogenous input w, that includes reference signal and disturbances, and the manipulated variables u;

- two outputs: the error signals z that we want to minimize, and the measured variables v, that are used to control the system.

v is used in $\mathbf{K}$ to calculate the manipulated variables u. In formulae, the system is:

$$\begin{Bmatrix} z \\ v \end{Bmatrix} = \mathbf{P}(s) \begin{Bmatrix} w \\ u \end{Bmatrix} = \begin{bmatrix} P_{11}(s) & P_{12}(s) \\ P_{21}(s) & P_{22}(s) \end{bmatrix} \begin{Bmatrix} w \\ u \end{Bmatrix} \tag{3.63}$$

$$u = \mathbf{K}(s)v \tag{3.64}$$

It is therefore possible to express the dependency of z on w as:

$$z = F_\ell(\mathbf{P}, \mathbf{K})w \tag{3.65}$$

F_ℓ is the *lower linear fractional transformation* and is defined as:

$$F_\ell(\mathbf{P}, \mathbf{K}) = P_{11} + P_{12}\mathbf{K}(I - P_{22}\mathbf{K})^{-1}P_{21} \tag{3.66}$$

The objective of the H-infinity control design is to find a controller $\mathbf{K}$ such that $F_\ell(\mathbf{P}, \mathbf{K})$ is minimised according to the H-infinity norm. The infinity norm of the transfer function matrix $F_\ell(\mathbf{P}, \mathbf{K})$ is defined as:

$$||F_\ell(\mathbf{P}, \mathbf{K})||_\infty = \sup_\omega \bar{\sigma}(F_\ell(\mathbf{P}, \mathbf{K})(j\omega)) \tag{3.67}$$

where $\bar{\sigma}$ is the maximum singular value of the matrix $F_\ell(\mathbf{P}, \mathbf{K})(j\omega)$. The aim of the control design is to minimize $||F_\ell(\mathbf{P}, \mathbf{K})||_\infty$, hence to minimize the maximum singular value.
The traditional two-sensitivity-function H-infinity controller synthesis algorithm is used, since it allows a complex control problem to be split into two discrete sections, one dealing with stability, the other dealing with performance. The sensitivity function, $S(s)$, and the complementary sensitivity function, $T(s)$, are used in the controller synthesis and are given by:

$$S(s) = \frac{1}{1 + P(s)K(s)} \tag{3.68}$$

$$T(s) = \frac{P(s)K(s)}{1 + P(s)K(s)} \tag{3.69}$$

The sensitivity function has an associated frequency-dependent weighting function, W_1, which is used to limit the magnitude of the sensitivity function within a particular frequency range, i.e. $||W_1(s)S(s)||_\infty < 1$. W_1 is the performance weighting function (measure) in the controller synthesis. In a similar fashion the complementary sensitivity function is combined with a frequency-dependent weighting function, W_2, which is used to limit the magnitude of T within a particular frequency range, i.e. $||W_2(s)T(s)||_\infty < 1$. W_2 is the robustness weighting function (stability constraint) in the controller synthesis. The two sensitivity functions are combined, with their respective weighting functions, into a single augmented state-space representation of the design problem. The problem then becomes one of finding a stabilising controller, if it exists, that satisfies both the performance and robustness criteria. It has been shown that a stabilising controller exists if positive semi-definite solutions can be determined to two Riccati equations, derived from the augmented state-space representation, and the spectral radius of the two solutions is strictly less than γ, which is the controller performance level. [6]

Measurement Platform Sensors

The zero displacement of the measurement platform is measured via six 1DoF Michelson type interferometers. The interferometer performance requirements are as follows:

- Bandwidth of $\leq 1\ mHz$ to $\geq 1\ MHz$;
- Non-linearity of $< 0.1\%$;
- Noise floor of $< 1\ nm$.

The requirements of the laser source for the interferometer are as follows:

- 633 nm HeNe laser;
- Power: $> 0.6\ mW$;
- Frequency stability (30 s): $< 50\ MHz$;
- Intensity stability (30 s): $< 3\%$.

The requirements for the electronic interface which takes optical fibre signals from each interferometer and convert them to a distance measurement are the following:

- Cope with interferometer speed of 1 mm/s (plus margin of at least 10) without

losing fringe lock;

- Resolution at least 1 nm;
- Noise $< 1\ nm$;
- Interface with optical fibre ring.

3.2.1. Control of the 2DoF Model: MPLAT

In the equivalent 2DoF model the objective is to minimize the vertical displacement of the MPLAT, which can be measured by the interferometer in the longitudinal direction. In fact, the rotations and the two horizontal displacements cannot be detected in the 2DoF model, since it only represents longitudinal translations.

Description

The general scheme of the H-infinity control for the 2DoF system is represented in fig. 3.54.

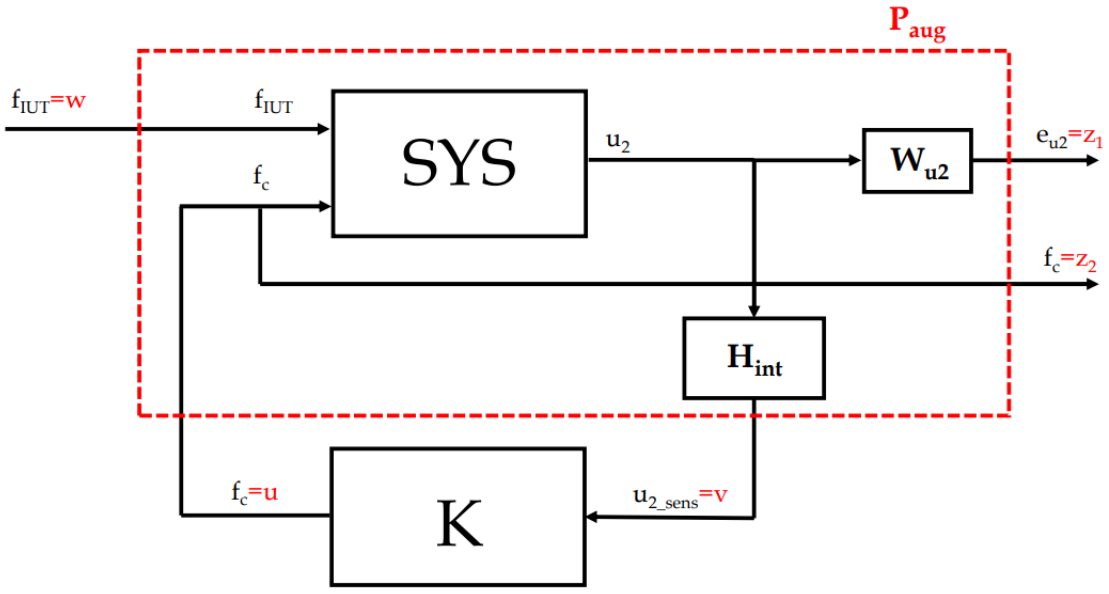

Figure 3.54: Control of the MPLAT (H-infinity) in the 2DoF system - general control scheme

The system **SYS** is the 2DoF equivalent model, which is defined in eq. (3.70) (from fig. 2.20). The damping is modelled in the Rayleigh form.

$$\underbrace{\begin{bmatrix} m_1 & 0 \\ 0 & m_2 \end{bmatrix}}_{\mathbf{M}} \underbrace{\begin{Bmatrix} \ddot{u}_1 \\ \ddot{u}_2 \end{Bmatrix}}_{\ddot{\mathbf{u}}} + \underbrace{\begin{bmatrix} C_{11} & C_{12} \\ C_{21} & C_{22} \end{bmatrix}}_{\mathbf{Damp}} \underbrace{\begin{Bmatrix} \dot{u}_1 \\ \dot{u}_2 \end{Bmatrix}}_{\dot{\mathbf{u}}} + \underbrace{\begin{bmatrix} k_1 + k_2 & -k_2 \\ -k_2 & k_2 \end{bmatrix}}_{\mathbf{K}} \underbrace{\begin{Bmatrix} u_1 \\ u_2 \end{Bmatrix}}_{\mathbf{u}} = \underbrace{\begin{Bmatrix} -f_{c2} \\ f_{c2} + f_{IUT} \end{Bmatrix}}_{\mathbf{F}} \tag{3.70}$$

In state space form it results:

$$\underbrace{\begin{Bmatrix} \dot{\mathbf{u}} \\ \ddot{\mathbf{u}} \end{Bmatrix}}_{\dot{\mathbf{x}}(t)} = \underbrace{\begin{bmatrix} \mathbf{0} & \mathbf{I} \\ -\mathbf{M}^{-1}\mathbf{K} & -\mathbf{M}^{-1}\mathbf{Damp} \end{bmatrix}}_{\mathbf{A}} \underbrace{\begin{Bmatrix} \mathbf{u} \\ \dot{\mathbf{u}} \end{Bmatrix}}_{\mathbf{x}(t)} + \underbrace{\begin{bmatrix} \mathbf{0} \\ \mathbf{M}^{-1}\mathbf{P_d} \end{bmatrix}}_{\mathbf{B}_d} \underbrace{f_{IUT}}_{d(t)} + \underbrace{\begin{bmatrix} \mathbf{0} \\ \mathbf{M}^{-1}\mathbf{P_u} \end{bmatrix}}_{\mathbf{B}_u} \underbrace{f_{c2}}_{u(t)} \tag{3.71}$$

where $\mathbf{P_d}$ and $\mathbf{P_u}$ are respectively the vectors corresponding to the disturbance force generated by IUT and to the actuator's control force.
Recalling fig. 3.54, the inputs of the system **SYS** are the disturbance force f_{IUT} and the actuator's control force f_c, while its output is the displacement u_2 of the MPLAT, measured by the interferometer.
The weighting functions in the H-infinity control are selected to account for the relative magnitude of signals, their frequency dependence, and their relative importance. In this case, it is fundamental to add the weight W_{u2}, which allows to obtain the desired FRF. W_{u2} is defined as the inverse of the $Target$ closed-loop TF from f_{IUT} to u_2, whose zeros are placed in correspondence of the resonance frequencies of the open-loop TF. Hence, the $Target$ TF is defined as in fig. 3.55.

$$Target(s) = 0.001\frac{(s+c)(s+d)}{s+e} \tag{3.72}$$

where the parameters c and d correspond to the resonance frequencies: $c = 2\pi 0.45\ rad/s$, $d = 2\pi 0.93\ rad/s$. On the other hand, the parameter e has been selected as $e = 2\pi 0.05\ rad/s$ in order to design a bowl function. The gain 0.001 has been tuned to minimize the displacement of the MPLAT. From here, the TF of the weight W_{u2} is defined as in eq. (3.73).

$$W_{u2}(s) = \frac{1}{Target(s)} \tag{3.73}$$

Figure 3.55 displays the Bode diagrams of the open loop TF, $Target$ and W_{u2}.

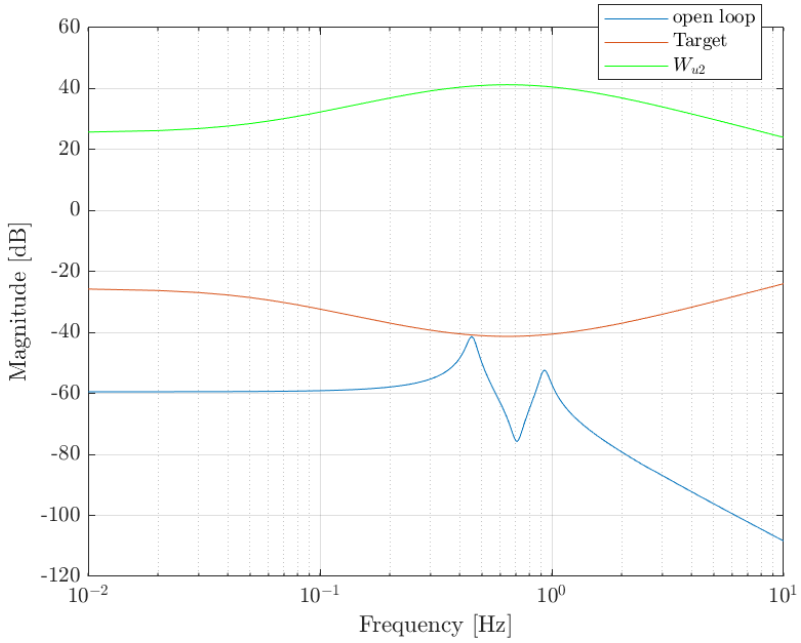

Figure 3.55: Bode diagrams of open loop, Target and W_{u2} TFs

The internal dynamics of the interferometer is modelled as a high-pass filter, given the large value of its bandwidth at high frequencies. This TF is displayed in eq. (3.74):

$$H_{int}(s) = \frac{s}{s+h} \tag{3.74}$$

where $h = 2\pi 10^{-3}\ rad/s$, according to the lower limit of the interferometer's bandwidth. No saturation block for the actuator can be added since saturation is inherently non-linear, while the TF formalism only applies to LTI systems. The check of the control force not exceeding the saturation limit can only be done after having excited the system with the disturbance force, hence when working in the time domain.
The red dashed box in fig. 3.54 represents the augmented plant $\mathbf{P_{aug}}$, which is the analogous of the $\mathbf{P}$ plant in fig. 3.53.
In order to retrieve the $\mathbf{K}$ controller with the command $hinfsyn$, it is necessary to define first the open loop system with the command *connect*. Its scheme is represented in fig. 3.56.

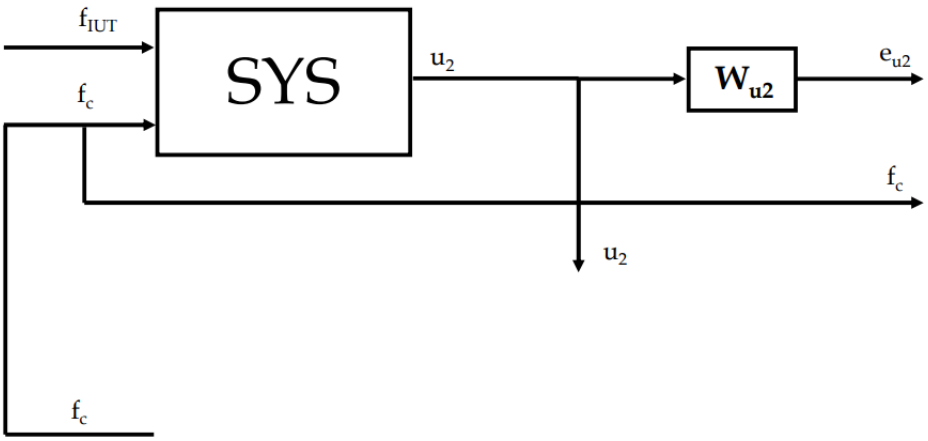

Figure 3.56: Control of the MPLAT (H-infinity) in the 2DoF system - open loop

After having retrieved the **K** controller, it can be connected to the open loop. Hence, the closed loop is built again with the command *connect*, where the input is f_{IUT} and the outputs are u_2 and f_c. The closed loop scheme is represented in fig. 3.57.

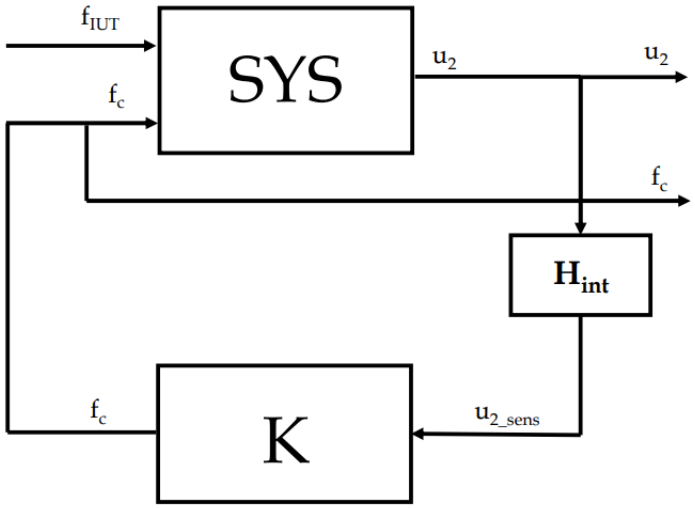

Figure 3.57: Control of the MPLAT (H-infinity) in the 2DoF system - closed loop

Afterwards, the time response to the excitation of the IUT can be studied. Such an excitation is bounded between 10^{-5} N and 0.1 N, as reported in table 1.1. It is modelled as a series of random numbers comprised within this interval, according to eq. (3.75).

$$f_{IUT} = k + (l - k)\ rand(length(t), 1) \tag{3.75}$$

where k and l are 10^{-5} N and 0.1 N, respectively, and t is the time vector. Thanks to the command $lsim$, it is possible to obtain the time responses to the disturbance of the IUT by selecting as output either the displacement of the MPLAT or the control force. As indicated in section 3.2, the noise floor of the interferometer is < 1 nm. Hence, it can be modelled as in eq. (3.76).

$$noise = m + (n - m)\ rand(length(t), 1) \tag{3.76}$$

where m and n are -10^{-9} nm and 10^{-9} nm, respectively. The sensor noise can now be added to the retrieved time history of the displacement of the MPLAT. Thus, the sensed variable u_2 embeds both the model of the internal dynamics of the interferometer and the sensor noise.

Results

Before adding the interferometer's internal dynamics, the displacement of the MPLAT in open and closed loop results as in fig. 3.58.

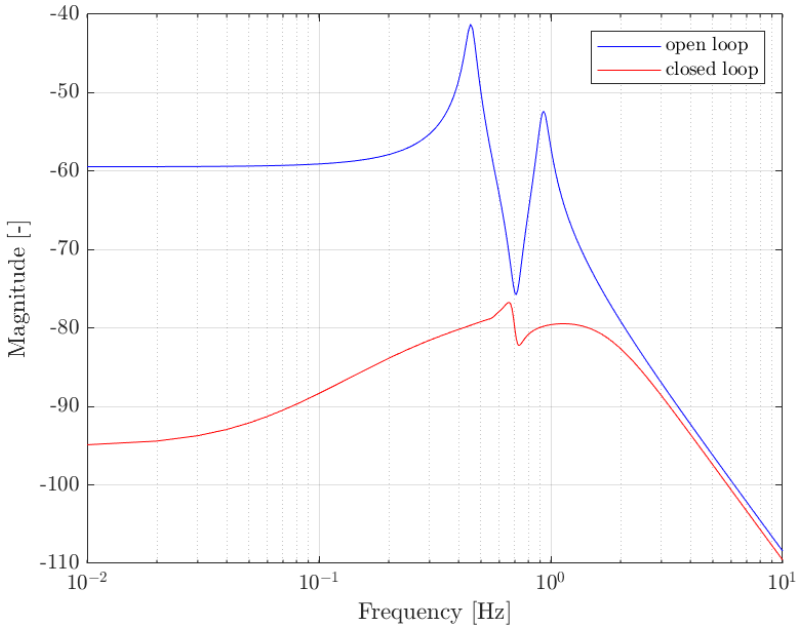

Figure 3.58: Effect of the H-infinity control on the Bode magnitude plot of the TF from f_{IUT} to u_2 - without interferometer's internal dynamics

As it can be appreciated, the magnitude is well damped over the entire frequency range.

The TF of the resulting **K** controller is:

$$K(s) = \frac{\begin{array}{c} -5.946 \cdot 10^9 s^5 - 5.707 \cdot 10^{11} s^4 - 4.932 \cdot 10^{12} s^3 + \\ - 2.17 \cdot 10^{13} s^2 - 9.425 \cdot 10^{13} s - 1.691 \cdot 10^{14} \end{array}}{\begin{array}{c} s^6 + 1670 s^5 + 1.29 \cdot 10^6 s^4 + \\ + 4.935 \cdot 10^8 s^3 + 3.263 \cdot 10^8 s^2 + 6.146 \cdot 10^9 s + 1.9 \cdot 10^9 \end{array}} \tag{3.77}$$

The time history of the displacement of the MPLAT is represented in fig. 3.59.

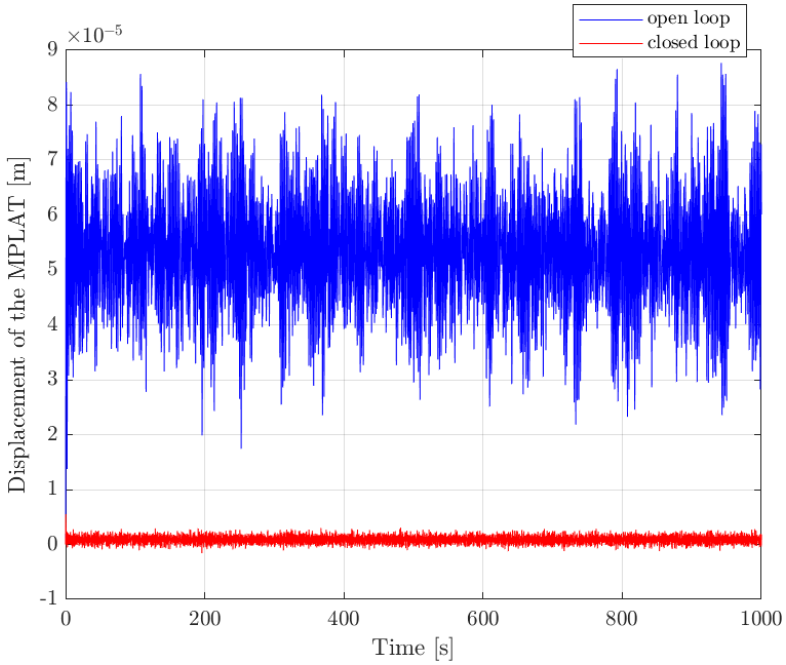

Figure 3.59: Effect of the H-infinity control on the displacement of the MPLAT - without interferometer's internal dynamics

From fig. 3.59, it can be noted that the H-infinity control generates a considerable decrease in the entity of the displacement of the MPLAT.
The time history of the control force generated by the actuator is displayed in fig. 3.60.

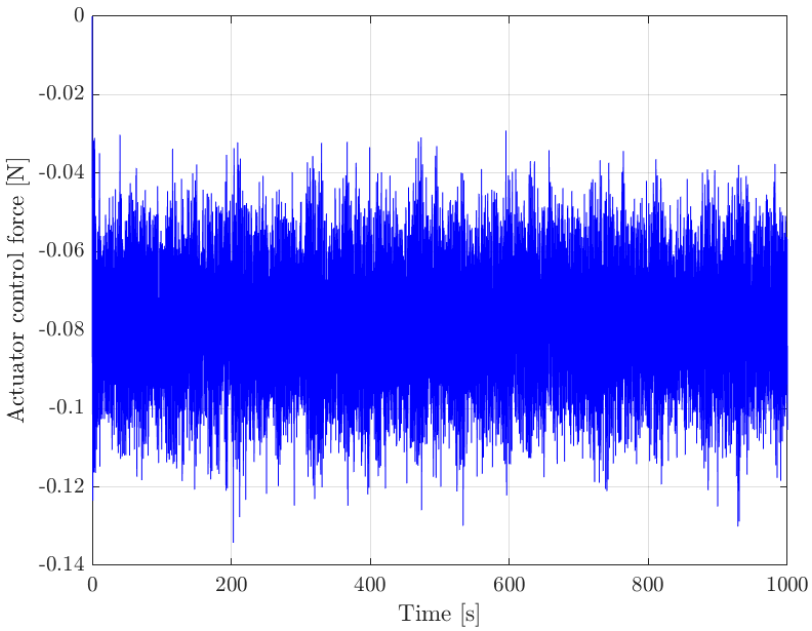

Figure 3.60: Actuator's control force in the H-infinity control - without interferometer's internal dynamics

It is noticeable that the maximum force generated by the actuator does not exceed the saturation limit of $\pm 3\ N$. Moreover, it can be appreciated that, while the disturbance force is positive, the counteracting control force is characterised by negative values. The reason of that can be found in the fact that the actuator's force is the force needed to counteract the disturbance generated by the IUT to minimize the MPLAT displacement. Figure 3.61 shows that the absolute value of the control force is close to the one of the disturbance force.

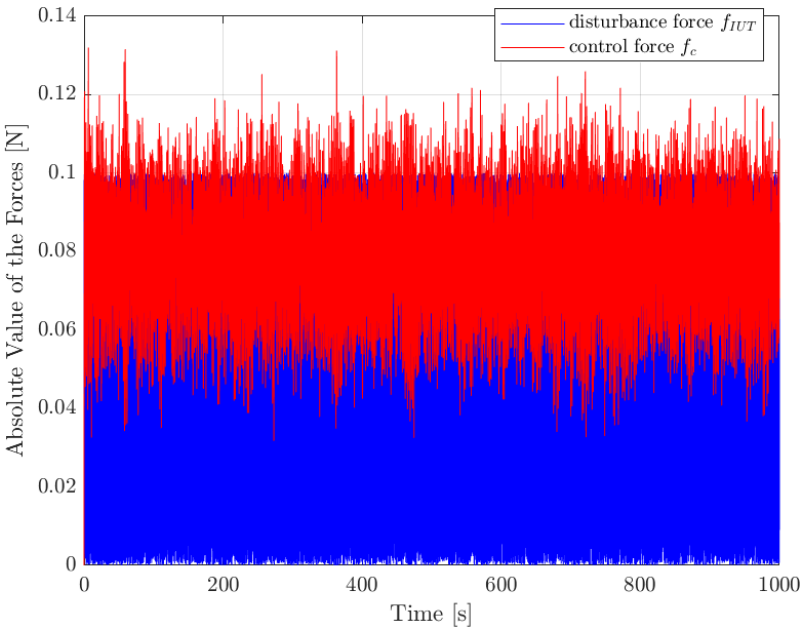

Figure 3.61: Comparison between absolute values of the disturbance force and of the control force

After having added to the loop the internal dynamics of the interferometer, the results are the following.
The effect of the control on the Bode magnitude plot is represented in fig. 3.62.

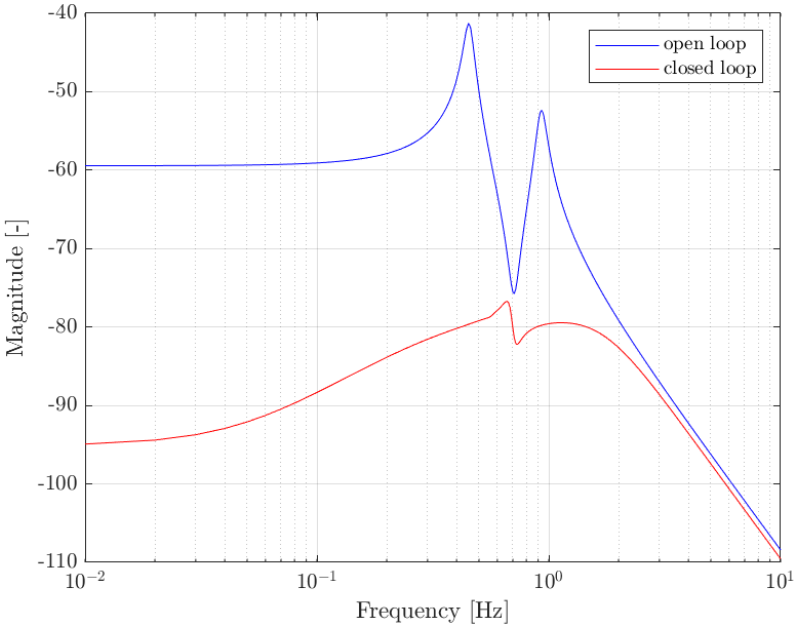

Figure 3.62: Effect of the H-infinity control on the Bode magnitude plot of the TF from f_{IUT} to u_2 - with interferometer's internal dynamics

The effect of the control on the displacement of the MPLAT is represented in fig. 3.63. In this figure the displacement of the MPLAT with and without the interferometer's noise is represented.

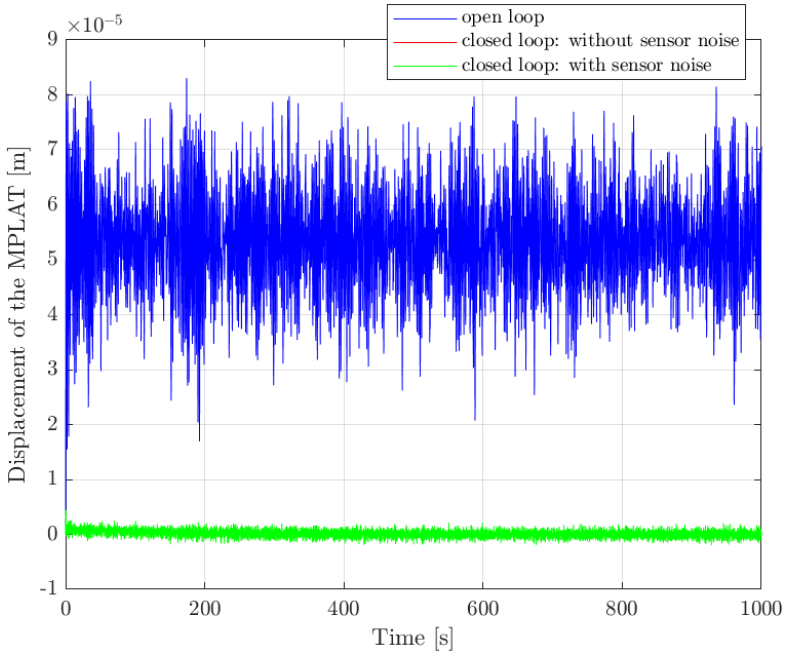

Figure 3.63: Effect of the H-infinity control on the displacement of the MPLAT - with interferometer's internal dynamics

It can be appreciated from fig. 3.63 that the interferometer's noise is sufficiently small to not significantly affect the entity of the displacement of the controlled MPLAT. Moreover, it can be noted that the displacement of the MPLAT passes from the order of 10^{-5} in open loop to the order of 10^{-7} in closed loop, losing two orders of magnitude.
The time history of the actuator's control force is displayed in fig. 3.64.

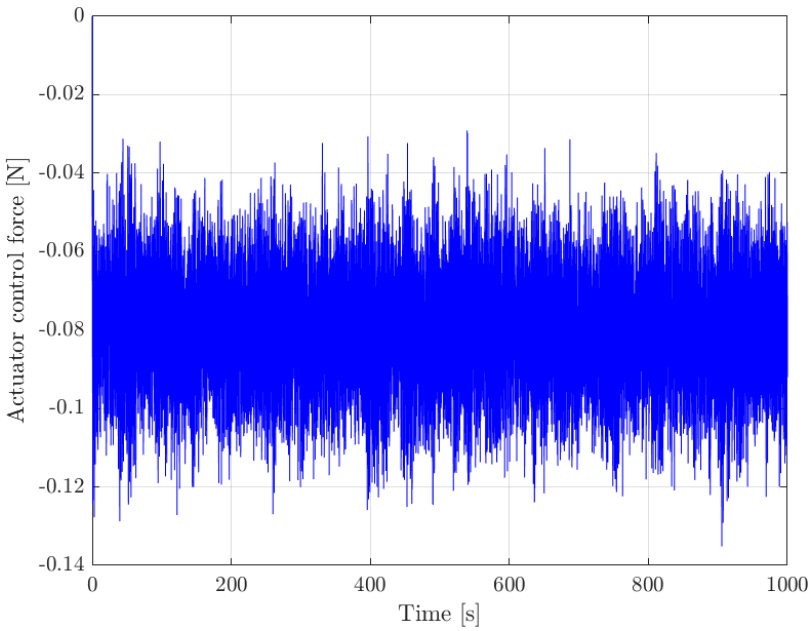

Figure 3.64: Actuator's control force in the H-infinity control - with interferometer's internal dynamics

From fig. 3.64 it is evident that also with the addition of the interferometer's internal dynamics the saturation constraint is again respected.
From the above figures, it results that the graphs with and without the interferometer's internal dynamics are very close to each other. Hence, the interferometer does not strongly affect the closed-loop dynamics.
Eventually, the check on the singular values can be done. The optimal performance level achieved by this controller is returned by the command $hinfsyn$ as γ, which is the H-infinity norm of the closed-loop system. We can examine the singular value plot of the closed-loop system (fig. 3.65) to confirm that its largest singular value does not exceed γ. In this case, $\gamma = 9.53 \cdot 10^{-7} = -120.42\ dB$.

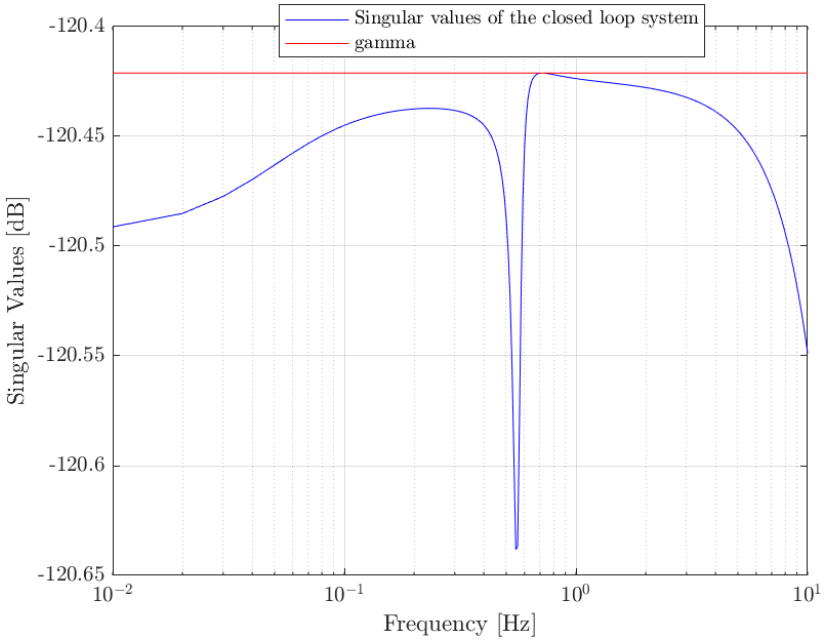

Figure 3.65: Singular values of the controlled 2DoF model

Finally, as a check, it is possible to reconstruct the open and closed loop FRFs from f_{IUT} to u_2 through the MATLAB® command $tfestimate$, starting from the time histories of the disturbance force and of the control force. It can be proven that those curves overlap with the Bode diagrams obtained with the *bode* command, as we can see in fig. 3.66.

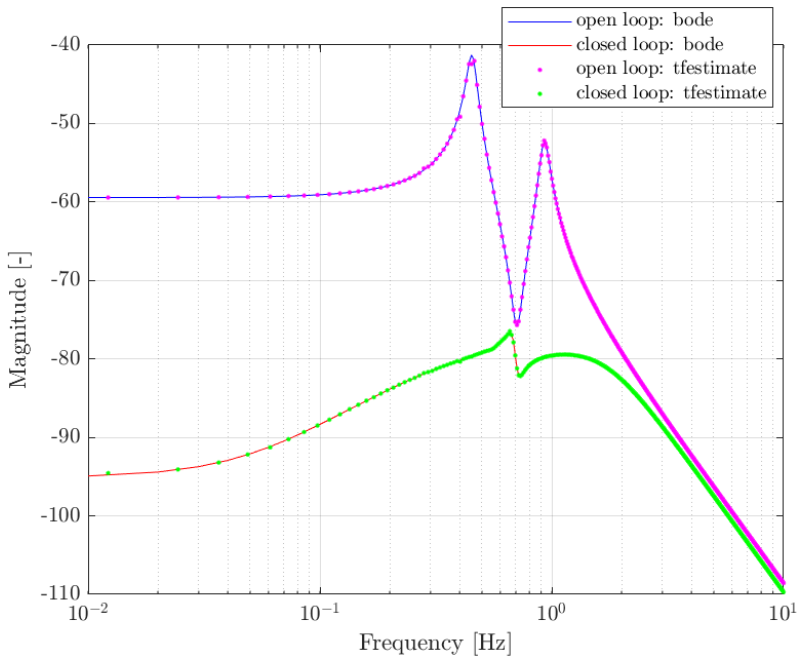

Figure 3.66: Recovery of the Bode diagram of the FRF from f_{IUT} to u_2 from time responses

3.2.2. Control of the Condensed Craig-Bampton Model: MPLAT

The condensed CB model has 3 physical and 11 modal DoFs. The 3 physical DoFs represent the 3 vertical translations of the MPLAT, the VIBISIO and the base, in this order. Like in the 2DoF model, also in the condensed CB one the rotations and the two horizontal displacements cannot be detected. The objective of the control is to minimize the vertical displacement of the MPLAT, whose node occupies the first position in the CB matrices, as illustrated in table 2.1. For this control design, the condensed CB model without LM is employed.

Description

The control system designed for the 2DoF model can now be extended to the condensed CB one, which is represented in SS form as in eq. (3.78):

$$\underbrace{\begin{Bmatrix}\dot{\mathbf{u}}_{cond}\\ \ddot{\mathbf{u}}_{cond}\end{Bmatrix}}_{\dot{\mathbf{x}}(t)} = \underbrace{\begin{bmatrix}\mathbf{0} & \mathbf{I}\\ -\mathbf{M}_{cond}^{-1}\mathbf{K}_{cond} & -\mathbf{M}_{cond}^{-1}\mathbf{Damp}_{cond}\end{bmatrix}}_{\mathbf{A}}\underbrace{\begin{Bmatrix}\mathbf{u}_{cond}\\ \dot{\mathbf{u}}_{cond}\end{Bmatrix}}_{\mathbf{x}(t)} + \underbrace{\begin{bmatrix}\mathbf{0}\\ \mathbf{M}_{cond}^{-1}\mathbf{P_d}\end{bmatrix}}_{\mathbf{B}_d}\underbrace{f_{IUT}}_{d(t)} + \underbrace{\begin{bmatrix}\mathbf{0}\\ \mathbf{M}_{cond}^{-1}\mathbf{P_u}\end{bmatrix}}_{\mathbf{B}_u}\underbrace{f_c}_{u(t)} \tag{3.78}$$

The vectors $\mathbf{P_d}$ and $\mathbf{P_u}$ are associated to the disturbance and to the control input, respectively.

$$\mathbf{P_d} = zeros(14,1) \rightarrow \mathbf{P_d}(1) = 1 \tag{3.79}$$

$$\mathbf{P_u} = zeros(14,1) \rightarrow \mathbf{P_u}(1) = 1; \mathbf{P_u}(2) = -1; \tag{3.80}$$

The output is the displacement of the MPLAT, hence $\mathbf{C}$ is a vector of zeros and one 1 in the first position, and $\mathbf{D}$ is a vector of two zeros.

Results

Before adding the internal dynamics of the interferometer to the loop, the results are the following.
The effect of the control on the Bode magnitude plot is represented in fig. 3.67.

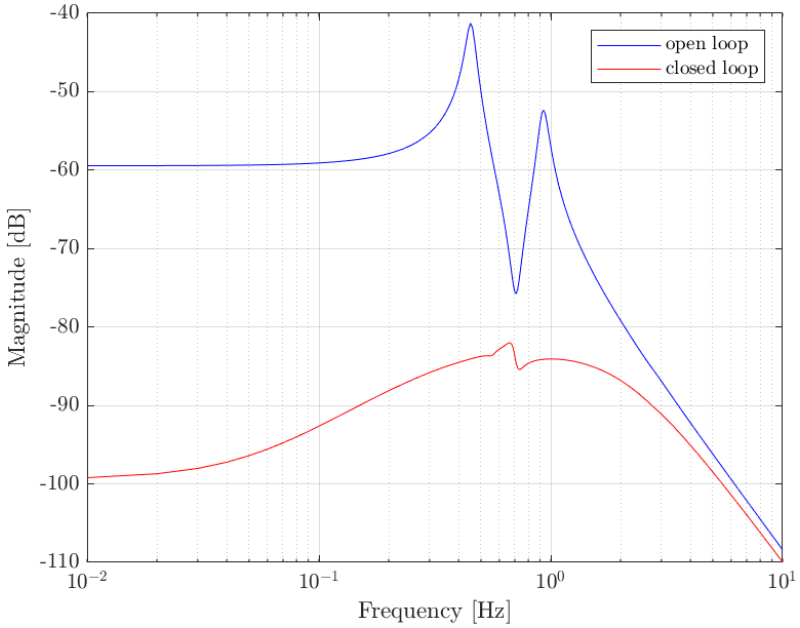

Figure 3.67: Effect of the H-infinity control on the Bode magnitude plot of the TF from f_{IUT} to u_2 - without interferometer's internal dynamics

The effect of the control on the displacement of the MPLAT is represented in fig. 3.68.

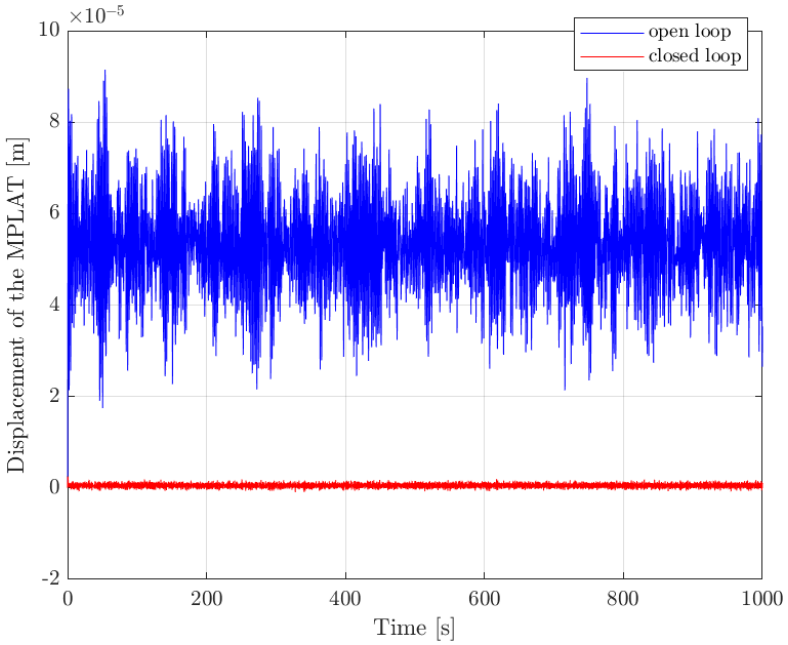

Figure 3.68: Effect of the H-infinity control on the displacement of the MPLAT - without interferometer's internal dynamics

The time history of the actuator's control force is displayed in fig. 3.69.

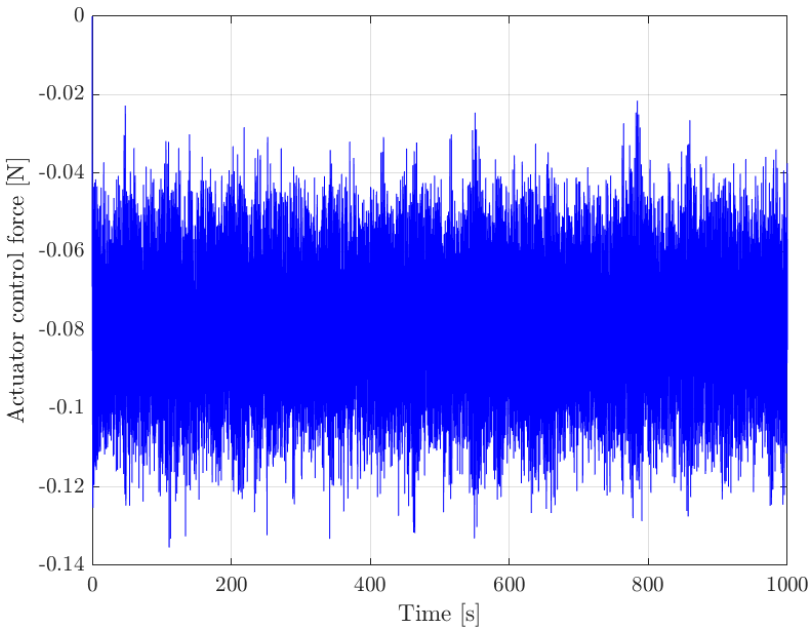

Figure 3.69: Actuator's control force in the H-infinity control - without interferometer's internal dynamics

The above graphs (fig. 3.67, fig. 3.68 and fig. 3.69) result very close to the ones obtained with the control of the 2DoF model (fig. 3.58, fig. 3.59 and fig. 3.60). This means that the extension from the 2DoF system to the condensed CB model has been effective.
From fig. 3.69 it is noticeable that the maximum force generated by the actuator does not exceed the saturation limit of $\pm 3\ N$. As in the 2DoF model, it can be appreciated that, while the disturbance force is positive, the counteracting control force is characterised by negative values. Figure 3.70 shows that the absolute value of the control force is close to the one of the disturbance force.

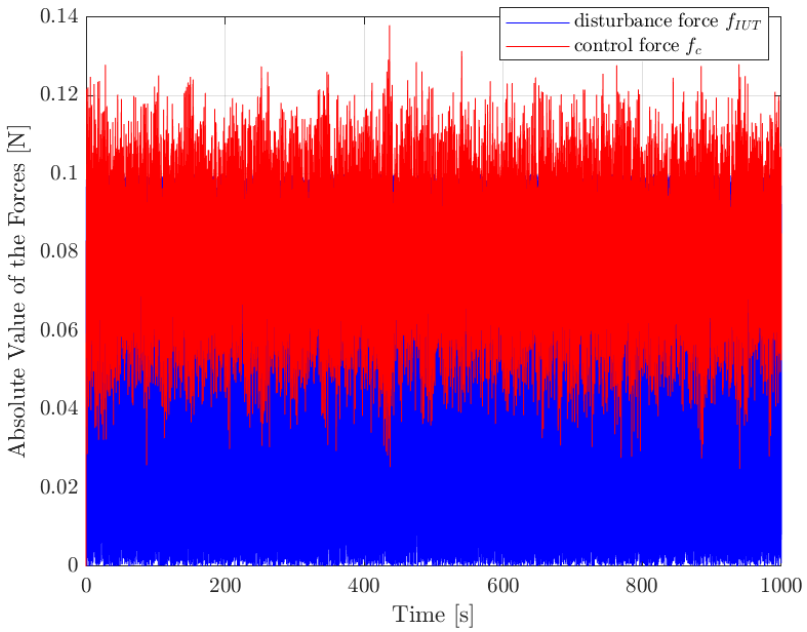

Figure 3.70: Comparison between absolute values of the disturbance force and of the control force

Adding the internal dynamics of the interferometer to the loop, the results are the following.
The effect of the H-infinity control on the Bode diagram still provides a good attenuation of the magnitude over the entire frequency range.

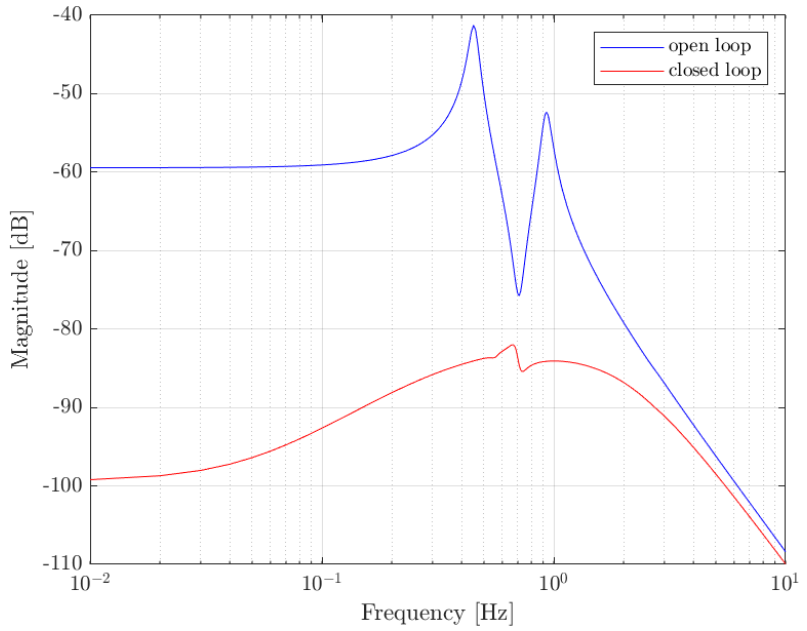

Figure 3.71: Effect of the H-infinity control on the magnitude plot of the TF from f_{IUT} to u_2 - with interferometer's internal dynamics

The effect of the control on the displacement of the MPLAT is represented in fig. 3.72. In this figure the displacement of the MPLAT with and without the interferometer's noise is represented.

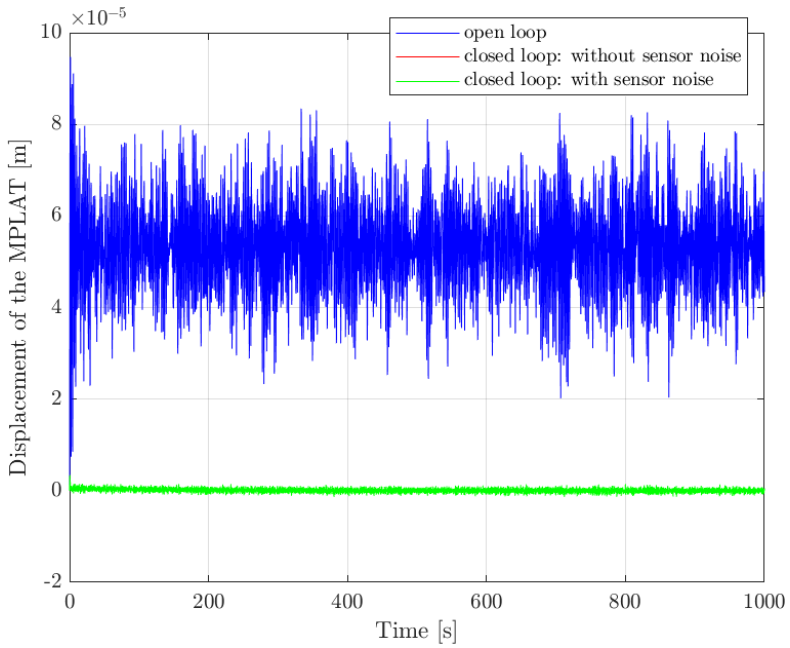

Figure 3.72: Effect of the H-infinity control on the displacement of the MPLAT - with interferometer's internal dynamics

It can be appreciated from fig. 3.72 that the interferometer's noise is sufficiently small to not significantly affect the entity of the displacement of the MPLAT. Moreover, it can be noted that the displacement of the MPLAT passes from the order of 10^{-5} in open loop to the order of 10^{-7} in closed loop, losing two orders of magnitude.
The time history of the actuator's control force is displayed in fig. 3.73.

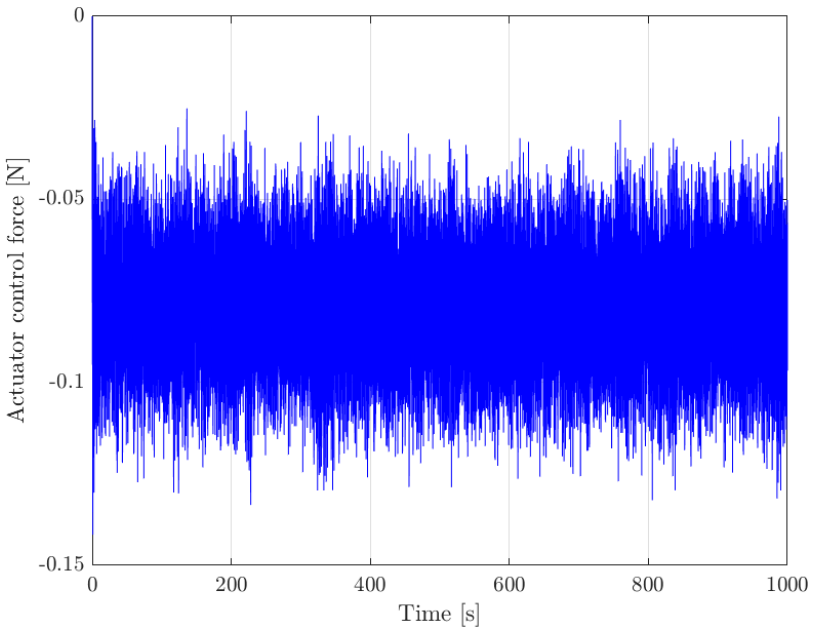

Figure 3.73: Actuator's control force in the H-infinity control - with interferometer's internal dynamics

In general, it results that all the graphs with and without the interferometer's internal dynamics are very close to each other. Hence, the interferometer does not strongly affect the closed-loop dynamics.
Eventually, the check on the singular values can be done. We can examine the singular value plot of the closed-loop system (fig. 3.74) to confirm that its largest singular value does not exceed γ. In this case, $\gamma = 5.75 \cdot 10^{-7} = -124.80\, dB$.

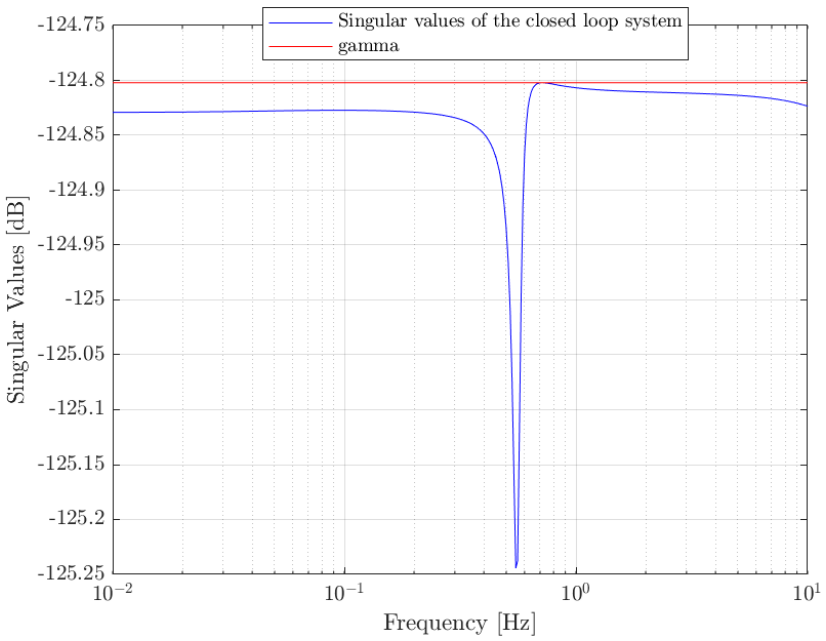

Figure 3.74: Singular values of the controlled condensed CB model

Finally, as a check, it is possible to reconstruct the open and closed loop FRFs from f_{IUT} to u_2 through the MATLAB® command $tfestimate$, starting from the time histories of the disturbance force and the control force. It can be proven that those curves overlap with the Bode diagrams obtained with the *bode* command, as we can see in fig. 3.75.

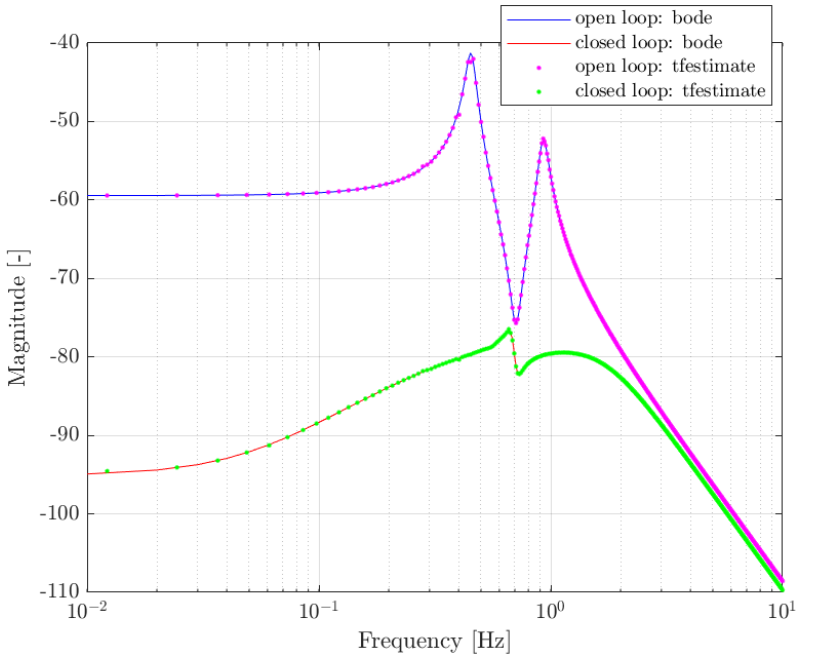

Figure 3.75: Recovery of the Bode diagram of the FRF from f_{IUT} to u_2 from time responses

4 | Conclusions and future developments

4.1. Conclusions

The work had the aim of designing effective control strategies to achieve the following two objectives:

- attenuate the micro vibrations transmitted from the ground to the IUT by the facility when working in **actuator mode**;
- measure the micro vibrations generated by the disturbance of the IUT by counteracting the motion with control forces, when the facility works in **sensor mode**.

To achieve both objectives, it has been necessary to work on some dynamic models which could accurately describe the behaviour of the full FEM model. The equivalent 2DoF model can accurately describe the longitudinal behaviour of the CB model, which is in turn a condensed representation of the full FEM system. Both in the 2DoF model and in the condensed CB one, only the longitudinal displacement has been considered, since the rotational DoFs and the translational displacements are not included in these models. Moreover, in order to impose an excitation from the ground (actuator mode), it has been necessary to apply the Large Mass method, both to the 2DoF model and to the CB one. All the mentioned models have been validated by showing that their FRFs precisely overlap.
The design of the control strategy of the **VIBISIO** had the objective of granting an attenuation of $-20\ dB$ of the resonance peaks. Firstly, a technique to control the equivalent 2DoF model has been investigated, and then this control strategy has been extended to the condensed CB model. Focusing on the 2DoF model, the FB control with skyhook damping has been first studied. Then, to improve the attenuation of the resonance peaks and hopefully reach the desired attenuation of $-20\ dB$, a FF control has been added. It results that the combined control guarantees the desired attenuation, but the required control force is larger than the saturation of the actuators. If the actuators can

be exploited at least 143.33% of their saturation limit, this control strategy is effective. Otherwise, if the saturation limit must necessarily be respected, the best performance is guaranteed by the FB control alone. Eventually, the FB and FF control has successfully been extended to the condensed CB model, leading to similar results and conclusions.
The design of the control strategy of the **MPLAT** has the aim of minimizing the displacement of the MPLAT itself: the control force counteracts the disturbance force generated by the IUT. This result has been obtained thanks to the H-infinity control, first designed on the 2DoF model and eventually extended to the condensed CB one. Such a control has been able to well attenuate the resonance peaks over the entire frequency range. In fact, the displacement of the MPLAT passes from the order of 10^{-5} to 10^{-7}, losing two orders of magnitude. Moreover, it is important to underline the fact that the control force remains far below the saturation limit.
In conclusion, the goals of the thesis have been achieved.

4.2. Future Developments

Some possible developments can be made in the study and, in addition, some modifications can be applied to the MVMS itself.

The largest developments which can be made in the research are:

1. Extending the control designs from the CB model with 14 DoFs to the one with 141 DoFs.
2. Design the FF TF in the VIBISIO control considering the Rayleigh damping and not the viscous one. In this way, the results would be more rigorous since the Rayleigh damping is the type of damping which compares all the models, while the viscous one cannot be implemented in the Nastran solution.
3. Understand the reasons why some FRFs do not well overlap at lower frequencies in the validation of the models.
4. Designing more refined control systems which could, for example, avoid the increase in the magnitude at lower frequencies when the FF control is implemented.
5. Analyzing different control strategies with respect to the sky-hook damper for the FB and the PI designed for the FF in the VIBISIO control, with the aim of respecting the saturation constraint and, at the same time, achieving the desired attenuation.
6. Enriching the H-infinity control scheme with more weighting functions (on the disturbance force and/or on the actuator control force) and adding sensor noise with

its weighting function.

7. Develop a robust controller with μ-synthesis to introduce model uncertainties in the control of the MPLAT.
8. Adjusting the sampling frequency of the control systems to the one of the devices present on the facility.

Some modifications that can be applied to the MVMS itself in order to obtain better results are:

1. Reducing the amplitude of the lateral dynamics coupled with the longitudinal one.
2. Allowing the actuators to work above their saturation given by the datasheet, which is of $\pm 3\ N$. To grant an attenuation of $-20\ dB$ it is necessary either to increase the saturation to $\pm 4.3\ N$ or to substitute the actuators with more performing ones.
3. Mounting a different type of actuators: piezoelectric actuators allow to implement a simple robust and very effective control strategy, and the closed-loop performances are easily predictable.
4. Providing a digital implementation of the control.
5. Redesigning the flexible joints between the truss and the support plates, in order to reduce their parasitic stiffness and keep the open-loop zeros close to the origin while keeping the axial stiffness and the overall strength needed during the excitation. The use of superelastic material in the joint seems to be an attractive option. [17]
6. Improving the lateral dynamics of the truss: the resonance peaks of the lateral modes can be moved to higher frequency by reducing and redistributing the inertia along the truss. Also, the membranes play a key role and their shape and distance should be optimized to combine low axial stiffness with high frequency lateral modes. On the other hand, the damping of the lateral modes should be improved without adding damping to the axial motion of the truss. Fitting a tuned-mass damper on the lateral modes of the trusses should be examined. [17]

Bibliography

[1] Feed forwards augment PID control. Control Engineering. URL https://www.controleng.com/articles/feed-forwards-augment-pid-control/.

[2] Guralp CMG-3T Broadband Sensor. Iris Passcal Instrument Center. URL https://www.passcal.nmt.edu/content/instrumentation/sensors/broadband-sensors/cmg-3t-bb-sensor.

[3] *MSC Nastran - 2012 Dynamic Analysis User's Guide*. MSC Software, 2012.

[4] *Report periodico afferente alla Variante del Piano di Monitoraggio Ambientale - Monitoraggio Ante e Corso d'Opera*, page 136. ANAS S.p.A., 2014-2015.

[5] BCcampus. The Michelson Interferometer. URL https://opentextbc.ca/universityphysicsv3openstax/chapter/the-michelson-interferometer/.

[6] R. Beaven, M. Wright, and D. Seaward. Weighting function selection in the H-infinity design process. *Elsevier - Pergamon*, pages 625–626, 1995.

[7] M. A. Beijen. *Disturbance Feedforward Control for Vibration Isolation Systems: Analysis, Design, and Implementation*. 2018.

[8] BME-MM. Enforced Motion in Structural Analysis. URL https://www.mm.bme.hu/~gyebro/files/ans_help_v182/ans_thry/str_EnMoinStAn.html.

[9] R. Breganon, M. A. F. Montezuma, M. M. de Souza, R. C. Lemes, and E. M. Belo. Optimal H-Infinity Controller Applied to a Stewart Platform. *International Journal of Advanced Engineering Research and Science (IJAERS)*, pages 56–57, 2018.

[10] Carter, Mancini, Bruce, and Ron. *Op Amps for Everyone*. Texas Instruments, 2009.

[11] B. Dasgupta and T. S. Mruthyunjaya. The stewart platform manipulator: a review. *Elsevier*, 1998.

[12] L. de Paula Pinto Mapa, F. de Assis das Neves, and G. Paulinelli Guimarães. Dynamic Substructuring by the Craig-Bampton Method Applied to Frames. *Springer*, pages 258–260, 2020.

[13] L. Dozio. *Control system design – introduction to state-space methods (part 1)*. Politecnico di Milano, 2019-2020.

[14] ESA. Statement of Work, ESA Express Procurement - EXPRO, SOW 6DOF MVMS Simulation Model. 2019.

[15] S. Gordon. The Craig-Bampton Method, FEMCI Book, 1999. URL `https://femci.gsfc.nasa.gov/craig_bampton/`.

[16] W. B. Haile and J. T. Young. *Primer on the Craig-Bampton Method - an Introduction to Boundary Node Functions, Base Shake Analyses, Load Transformation Matrices, Modal Synthesis and Much More.* 2000.

[17] A. A. Hanieh. *Active Isolation and Damping of Vibrations via Stewart Platform.* ULB, Active Structures Laboratory, 2003.

[18] T. Irvine. Effective Modal Mass and Modal Participation Factors. pages 1–2, 2015.

[19] S. Jung. The Control of Spring-Mass-Damper Convergence System using H-Infinity Controller and μ–Synthesis Controller. *ResearchGate*, 2017.

[20] Z. Liang and G. C. Lee. *Damping of Structures: Part 1 - Theory of Complex Damping*, page 26. Department of Civil Engineering, State University of New York at Buffalo, 1991.

[21] P. Léger, I. M. Idé, and P. Paultre. Multiple-support seismic analysis of large structures. *Elsevier*, 1990.

[22] J. Martino and K. Harri. Virtual shaker modeling and simulation, parameters estimation of a high damped electrodynamic shaker. *Elsevier*, 2018.

[23] MathWorks. Robust control of an active suspension, 2022. URL `https://it.mathworks.com/help/robust/gs/active-suspension-control-design.html`.

[24] MathWorks. H-infinity performance, 2022. URL `https://it.mathworks.com/help/robust/gs/h-infinity-performance.html`.

[25] A. Megretski. Multivariable Control Systems. *Massachusetts Institute of Technology - Department of Electrical Engineering and Computer Science*, pages 1–3, 2004.

[26] MIT. Material damping. URL `https://abaqus-docs.mit.edu/2017/English/SIMACAEMATRefMap/simamat-c-dampingopt.htm`.

[27] U. of Michigan, C. M. University, and U. of Detroit Mercy. Designing lead and

lag compensators. URL https://ctms.engin.umich.edu/CTMS/index.php?aux=Extras_Leadlag.

[28] A. Preumont, M. Horodinca, I. Romanescu, B. de Marneffe, M. Avraam, A. Deraemaeker, F. Bossens, and A. A. Hanieh. A six-axis single-stage active vibration isolator based on stewart platform. *Elsevier*, pages 644–649, 2007.

[29] C. Qingsong and L. Weijia. Development of an Active Vibration Isolation System Using a Z-Bracket Based on PZT. *Journal of low frequency noise, vibration and active control*, 2006.

[30] D. Roettgen, B. Seegar, W. C. Tai, S. Baek, T. Dossogne, M. Allen, R. Kuether, M. R. W. Brake, and R. Mayes. A comparison of reduced order modeling techniques used in dynamic substructuring. U.S. Department of Energy - Office of Scientific and Technical Information, 2015.

[31] SPIE. Laser interferometer. URL https://spie.org/publications/tt61_541_laser_interferometer.

[32] J. Tang, D. Cao, and T. Yu. Decentralized vibration control of a voice coil motor-based stewart parallel mechanism: Simulation and experiments. *Institution of Mechanical Engineers*, 2018.

[33] J. Wijker. *Mechanical Vibrations in Spacecraft Design - Modal Effective Mass*, pages 111–112. Springer-Verlag Berlin Heidelberg, 2004.

[34] M. Yasuda, T. Osaka, and M. Ikeda. Feedforward control of a vibration isolation system for disturbance suppression. 1996.

[35] Z. Zhou, X. Chen, and B. Zhou. Feedforward compensation in vibration isolation system subject to base disturbance. *Journal of Vibration and Control*, 2015.

A | Appendix A: Large Mass Method

In structural analysis, enforced motion is a common excitation. The equations of motion in terms of absolute displacements can be expressed by:

$$\mathbf{M}\ddot{\mathbf{u}} + \mathbf{C}\dot{\mathbf{u}} + \mathbf{K}\mathbf{u} = \mathbf{F} \tag{A.1}$$

Partition the DoFs into two sets:

$$\mathbf{u} = \begin{Bmatrix} \mathbf{u}_1 \\ \mathbf{u}_2 \end{Bmatrix} \tag{A.2}$$

where $\mathbf{u}_1$ are the displacements remaining free and $\mathbf{u}_2$ are the displacements with enforced motion.

Assuming that the only excitation source is the enforced motion, the load vector applied on DoF $\mathbf{u}_1$ is zero. Equation (A.1) can be expanded to:

$$\begin{bmatrix} \mathbf{M}_{11} & \mathbf{M}_{12} \\ \mathbf{M}_{21} & \mathbf{M}_{22} \end{bmatrix} \begin{Bmatrix} \ddot{\mathbf{u}}_1 \\ \ddot{\mathbf{u}}_2 \end{Bmatrix} + \begin{bmatrix} \mathbf{C}_{11} & \mathbf{C}_{12} \\ \mathbf{C}_{21} & \mathbf{C}_{22} \end{bmatrix} \begin{Bmatrix} \dot{\mathbf{u}}_1 \\ \dot{\mathbf{u}}_2 \end{Bmatrix} + \begin{bmatrix} \mathbf{K}_{11} & \mathbf{K}_{12} \\ \mathbf{K}_{21} & \mathbf{K}_{22} \end{bmatrix} \begin{Bmatrix} \mathbf{u}_1 \\ \mathbf{u}_2 \end{Bmatrix} = \begin{Bmatrix} \mathbf{0} \\ \mathbf{F}_2 \end{Bmatrix} \tag{A.3}$$

where $\mathbf{F}_2$ is the reaction force between the structure and its supports.

The Large Mass method is an approximate technique that treats the response to acceleration excitation as a response to external forces. Assuming that the masses associated with the $\mathbf{M}_{22}$ subsystem are augmented so that it becomes $\mathbf{M}_{22} + \mathbf{M}_{22}^{LM}$, it is obtained:

$$\begin{bmatrix} \mathbf{M}_{11} & \mathbf{M}_{12} \\ \mathbf{M}_{21} & \mathbf{M}_{22} + \mathbf{M}_{22}^{LM} \end{bmatrix} \begin{Bmatrix} \ddot{\mathbf{u}}_1 \\ \ddot{\mathbf{u}}_2 \end{Bmatrix} + \begin{bmatrix} \mathbf{C}_{11} & \mathbf{C}_{12} \\ \mathbf{C}_{21} & \mathbf{C}_{22} \end{bmatrix} \begin{Bmatrix} \dot{\mathbf{u}}_1 \\ \dot{\mathbf{u}}_2 \end{Bmatrix} + \begin{bmatrix} \mathbf{K}_{11} & \mathbf{K}_{12} \\ \mathbf{K}_{21} & \mathbf{K}_{22} \end{bmatrix} \begin{Bmatrix} \mathbf{u}_1 \\ \mathbf{u}_2 \end{Bmatrix} = \begin{Bmatrix} \mathbf{0} \\ \mathbf{F}_2 \end{Bmatrix} \tag{A.4}$$

Solve the equations of $\ddot{\mathbf{u}}_2$:

$$\ddot{\mathbf{u}}_2 = (\mathbf{M}_{22} + \mathbf{M}_{22}^{LM})^{-1}(\mathbf{F}_2 - \mathbf{K}_{22}\mathbf{u}_2 - \mathbf{K}_{21}\mathbf{u}_1 - \mathbf{C}_{22}\dot{\mathbf{u}}_2 - \mathbf{C}_{21}\dot{\mathbf{u}}_1 - \mathbf{M}_{21}\ddot{\mathbf{u}}_1) \tag{A.5}$$

Define $\overline{\mathbf{M}} = (\mathbf{M}_{22}^{LM})^{-1}$ and substitute eq. (A.5) into the upper part of eq. (A.4) to get:

$$(\mathbf{M}_{11} - \mathbf{M}_{12}\overline{\mathbf{M}}\mathbf{M}_{21})\ddot{\mathbf{u}}_1 + (\mathbf{C}_{11} - \mathbf{M}_{12}\overline{\mathbf{M}}\mathbf{C}_{21})\dot{\mathbf{u}}_1 + (\mathbf{K}_{11} - \mathbf{M}_{12}\overline{\mathbf{M}}\mathbf{K}_{21})\mathbf{u}_1 = \overline{\mathbf{F}} \tag{A.6}$$

where:

$$\overline{\mathbf{F}} = -\mathbf{K}_{12}\mathbf{u}_2 - \mathbf{C}_{12}\dot{\mathbf{u}}_2 - \mathbf{M}_{12}\overline{\mathbf{M}}(\mathbf{F}_2 - \mathbf{K}_{22}\mathbf{u}_2 - \mathbf{C}_{22}\dot{\mathbf{u}}_2) \tag{A.7}$$

If $\mathbf{M}_{22}^{LM}$ is large enough, $\overline{\mathbf{M}}$ tends to zero, and the following approximation is verified:

$$\mathbf{F}_2 = (\mathbf{M}_{22} + \mathbf{M}_{22}^{LM})\ddot{\mathbf{u}}_2 \sim \mathbf{M}_{22}^{LM}\ddot{\mathbf{u}}_2 \tag{A.8}$$

A ratio of the Large Mass to the mass of the entire structure in the range of 104 to 108 keeps the modeling error small (see [21]). The solution of eq. (A.6) is the absolute displacement vector $\mathbf{u}_1$. [8]

B | Appendix B: Effective Modal Masses

The effective modal masses of the physical system from mode 11 on are represented in table B.1. The largest values of the effective modal masses are highlighted in red.

Table B.1: Effective modal masses of the physical system

Mode	Frequency [Hz]	T_1 [kg]	T_2 [kg]	T_3 [kg]	R_1 $[kg \cdot m]$	R_2 $[kg \cdot m]$	R_3 $[kg \cdot m]$
11	1.845	7.85E-05	2.44E-06	3.34E-09	3.73E-06	1.14E-04	2.62E-11
12	1.946	1.75E-06	5.60E-05	3.58E-08	7.73E-05	2.29E-06	1.12E-08
13	42.376	1.79E-01	3.60E-05	1.82E-03	8.14E-06	1.16E-01	5.10E-07
14	42.439	3.57E-05	1.81E-01	2.43E-07	1.17E-01	8.02E-06	1.67E-04
15	46.544	1.04E-03	1.63E-09	3.30E-01	1.49E-08	4.37E-04	8.94E-05
16	129.599	1.18E-01	1.60E-04	5.02E-07	2.91E-08	5.98E-06	2.50E-08
17	129.761	1.62E-04	1.18E-01	3.51E-09	5.35E-06	3.71E-08	3.37E-05
18	142.553	6.24E-05	1.71E-06	4.94E-04	2.31E-09	1.22E-07	3.83E-04
19	142.835	1.38E-11	6.11E-14	1.90E-11	2.49E-14	2.61E-12	9.86E-12
20	143.249	1.88E-13	1.98E-13	1.12E-13	2.08E-12	1.89E-14	6.50E-12
21	158.080	8.35E-09	1.94E-10	8.01E-13	7.55E-13	3.29E-11	5.54E-11
22	158.761	3.97E-09	2.49E-08	1.31E-12	7.04E-11	3.91E-11	1.30E-09
23	159.219	4.50E-02	6.64E-05	2.13E-06	1.09E-05	1.34E-04	9.66E-05
24	159.631	7.18E-05	4.38E-02	1.17E-06	1.29E-04	1.12E-05	4.13E-03
25	161.745	5.27E-10	4.08E-09	4.58E-14	1.18E-11	4.25E-14	4.69E-12
26	163.810	1.12E-05	6.36E-04	3.98E-05	5.20E-06	2.18E-07	1.99E-01
27	168.335	2.84E-11	2.90E-09	5.53E-15	4.13E-12	1.27E-12	1.17E-10
28	170.448	3.49E-10	2.32E-11	1.79E-14	2.15E-13	4.20E-13	4.83E-11
29	172.588	9.81E-10	1.07E-11	1.04E-13	4.65E-13	8.96E-13	1.39E-13
30	186.665	1.53E-10	1.94E-11	5.97E-13	1.29E-12	1.04E-12	2.30E-12
31	188.231	6.09E-11	5.68E-12	7.33E-13	4.83E-12	6.05E-13	3.49E-12
32	188.732	5.20E-06	2.32E-04	2.73E-05	5.39E-05	4.18E-04	1.57E-04
33	188.919	2.43E-04	6.05E-06	2.84E-06	4.31E-04	5.32E-05	2.44E-05
34	190.266	3.82E-10	1.96E-06	1.50E-03	4.09E-10	1.02E-05	1.40E-02
35	192.641	1.24E-12	6.26E-14	1.46E-11	1.81E-14	6.67E-14	3.24E-10
36	197.853	2.34E-18	6.84E-16	2.44E-18	2.91E-18	2.16E-20	1.12E-16
37	198.071	1.74E-13	6.75E-11	2.58E-13	3.51E-13	8.36E-16	1.07E-11
38	205.886	5.78E-17	5.03E-11	1.40E-13	1.31E-13	5.65E-15	7.14E-12
39	207.420	3.05E-11	2.40E-13	8.10E-14	4.33E-15	8.26E-14	4.59E-12
40	217.098	2.04E-22	2.97E-18	1.13E-19	2.93E-19	7.00E-21	1.69E-19
41	230.510	1.37E-11	8.84E-12	1.13E-14	3.01E-15	9.30E-15	1.63E-13
42	231.000	3.70E-12	1.39E-11	1.61E-14	6.91E-15	2.88E-15	2.97E-13
43	240.035	1.39E-12	7.32E-13	7.80E-14	7.71E-15	1.16E-15	6.29E-13
44	241.247	2.96E-12	8.57E-13	3.98E-14	1.20E-14	1.06E-14	2.98E-13
45	244.130	6.72E-13	1.43E-12	3.54E-16	1.06E-14	1.52E-14	1.02E-15
46	247.108	1.26E-19	1.12E-23	5.18E-19	8.54E-21	5.60E-20	1.38E-19

B| Appendix B: Effective Modal Masses

The effective modal masses of the Craig-Bampton model from mode 11 on are represented in table B.2. The largest values of the effective modal masses are highlighted in red.

Table B.2: Effective modal masses of the Craig-Bampton model

Mode	**Frequency [Hz]**	T_1 **[kg]**	T_2 **[kg]**	T_3 **[kg]**	R_1 $[kg \cdot m]$	R_2 $[kg \cdot m]$	R_3 $[kg \cdot m]$
11	1.845	7.85E-05	2.43E-06	1.86E-09	3.73E-06	1.14E-04	1.88E-12
12	1.946	1.74E-06	5.59E-05	3.70E-08	7.74E-05	2.29E-06	1.12E-08
13	42.367	1.80E-01	5.18E-09	1.82E-03	3.52E-06	1.16E-01	4.69E-08
14	42.425	3.03E-08	1.81E-01	1.90E-08	1.17E-01	3.56E-06	1.71E-04
15	46.537	1.03E-03	4.38E-09	3.30E-01	9.34E-09	4.35E-04	9.06E-05
16	128.404	3.90E-03	1.21E-01	1.58E-07	1.35E-06	5.16E-07	1.77E-04
17	129.208	1.17E-01	3.91E-03	1.24E-06	4.14E-07	3.50E-06	3.31E-04
18	143.213	4.26E-05	2.40E-06	4.98E-04	5.57E-09	1.75E-07	6.01E-04
19	145.334	3.37E-09	4.91E-10	6.17E-11	6.33E-11	6.32E-11	2.57E-08
20	145.860	2.70E-08	1.39E-09	2.43E-10	1.05E-10	4.06E-10	4.47E-09
21	158.692	2.49E-02	2.84E-03	3.47E-05	1.40E-08	1.07E-04	5.96E-02
22	159.145	3.79E-03	3.43E-02	2.13E-07	1.51E-04	4.31E-07	7.72E-05
23	161.162	1.34E-02	8.16E-04	3.16E-05	1.66E-06	3.97E-05	1.48E-01
24	164.540	5.01E-05	2.22E-05	3.12E-11	1.88E-08	1.32E-07	1.44E-05
25	166.890	1.30E-05	1.82E-05	1.45E-10	4.10E-08	5.64E-09	9.82E-07
26	171.261	3.56E-06	1.35E-08	5.75E-11	2.91E-10	1.99E-09	2.23E-06
27	173.519	2.81E-09	7.72E-07	2.17E-11	4.07E-10	9.71E-11	9.92E-07
28	176.454	7.93E-07	2.67E-08	5.34E-15	4.31E-11	5.04E-11	7.67E-08
29	178.248	2.03E-07	2.25E-07	1.23E-10	1.58E-11	8.58E-12	1.38E-07
30	188.690	1.04E-05	1.56E-04	4.21E-05	5.47E-05	4.11E-04	1.98E-04
31	188.912	2.09E-04	4.35E-06	7.11E-08	4.27E-04	5.76E-05	2.75E-06
32	189.230	5.28E-07	7.23E-08	4.34E-07	1.12E-09	5.09E-08	1.90E-06
33	189.950	2.73E-05	6.71E-06	1.46E-03	2.03E-06	1.19E-05	1.05E-02
34	191.924	4.45E-08	6.85E-09	7.08E-08	1.61E-11	1.39E-09	1.25E-06
35	196.655	3.98E-08	3.31E-08	1.05E-07	5.96E-11	1.91E-10	4.74E-06
36	198.340	1.99E-08	5.48E-08	4.87E-09	2.91E-13	6.68E-11	4.62E-08
37	202.403	3.87E-08	8.27E-08	5.05E-10	1.02E-11	2.10E-11	4.60E-08
38	207.768	1.31E-07	1.06E-07	1.39E-08	1.69E-12	1.62E-10	1.03E-06
39	209.346	1.40E-07	1.95E-07	3.45E-09	1.80E-10	1.47E-12	2.37E-07
40	225.399	4.11E-07	1.62E-06	1.99E-08	2.48E-08	1.12E-08	6.34E-08
41	234.908	5.42E-10	1.12E-07	4.72E-09	2.42E-09	2.03E-10	8.89E-08
42	235.733	1.45E-07	1.88E-10	2.21E-09	2.39E-10	3.39E-09	4.67E-08
43	242.040	3.85E-10	8.70E-09	8.23E-08	5.50E-10	9.41E-13	6.95E-07

List of Figures

List of Tables

List of Symbols

Variable	Description	SI unit
$\mathbf{0}$	Matrix of zeros	-
α	Parameter of the feedforward	rad/s
γ	H-infinity norm of the closed-loop system	-
Γ_i	Modal participation factor for mode i	-
$\boldsymbol{\phi}$	Eigenvector matrix	-
$\boldsymbol{\phi}_{ik}$	Fixed base mode shapes	-
$\boldsymbol{\psi}_{ib}$	Rigid body vector	-
ω	Angular frequency	rad/s
ω_m	First eigenfrequency	rad/s
ω_n	Second eigenfrequency	rad/s
a	Acceleration	m/s^2
A	Amplitude of actuator's acceleration	m/s^2
$\mathbf{A}$	State matrix	*variable*
$\mathbf{B}_u$	Input matrix	*variable*
$\mathbf{B}_d$	Disturbance matrix	*variable*
$\mathbf{C}$	Damping matrix	$\frac{Ns}{m}$
$\mathbf{C}_y$	Output matrix	*variable*
$\mathbf{C}_z$	Performance matrix	*variable*
$\mathbf{d}$	Displacement vector in the Craig-Bampton model	m
$\mathbf{d}$	Disturbance inputs	*variable*
$\mathbf{Damp}$	Craig-Bampton damping matrix	$\frac{Ns}{m}$
$\mathbf{Damp}_{cond}$	Condensed Craig-Bampton damping matrix	$\frac{Ns}{m}$
$\mathbf{D}_{yd}$	Disturbance direct feedthrough matrix	*variable*
$\mathbf{D}_{yu}$	Direct feedthrough matrix	*variable*

Variable	Description	SI unit
f	Frequency	Hz
$\mathbf{f}_c$	Actuator's control force	N
$\mathbf{F}$	Forcing vector	N
$\mathbf{F}_{CB}$	Craig-Bampton forcing vector	N
$\mathbf{F}_{cond}$	Condensed Craig-Bampton forcing vector	N
F_ℓ	Lower linear fractional transformation	-
g	Gain	-
H	Internal dynamics of the seismometer	-
$\tilde{H}$	Pseudo-integrator	-
H_{int}	Interferometer's transfer function	-
$\mathbf{I}$	Identity matrix	-
j	Imaginary unit	-
$\mathbf{K}$	Controller	-
$\mathbf{K}$	Stiffness matrix	$\frac{N}{m}$
$\mathbf{K}_{CB}$	Craig-Bampton stiffness matrix	$\frac{N}{m}$
$\mathbf{K}_{cond}$	Condensed Craig-Bampton stiffness matrix	$\frac{N}{m}$
$\mathbf{L}$	Coefficient vector for modal effective mass computation	kg
$\mathbf{L}_c$	Load coefficients vector	-
$\mathbf{m}$	Vector of masses	kg
$m_{eff,i}$	Effective modal mass for mode i	kg
$\mathbf{M}$	Mass matrix	kg
$\hat{M}$	Generalized mass matrix	kg
$\mathbf{M}_{CB}$	Craig-Bampton mass matrix	kg
$\mathbf{M}_{cond}$	Condensed Craig-Bampton mass matrix	kg
P	Primary path	-
$\mathbf{P_d}$	Vector associated to the disturbance	-
$\mathbf{P_u}$	Vector associated to the control input	-
$\mathbf{q}_k$	Modal DoFs	m
$\mathbf{r}$	Influence vector	-
s	Laplace variable	rad/s
S	Secondary path	-

Variable	Description	SI unit
S	Sensitivity function	-
t	Time	s
T	Complementary sensitivity function	-
T_1	Transfer function from a_0 to a_1	-
T_2	Transfer function from a_0 to a_2	-
$Target$	Target transfer function	-
u	Manipulated variables	*variable*
$\mathbf{u}$	Control inputs	*variable*
$\mathbf{u}$	Displacement vector in the 3DoF model	m
$\mathbf{u}_b$	Boundary DoFs	m
$\mathbf{u}_{CB}$	Craig-Bampton displacement vector	m
$\mathbf{u}_{cond}$	Condensed Craig-Bampton displacement vector	m
$\mathbf{u}_i$	Internal (leftover) DoFs	m
U_n	Normal modes eigenvectors	-
v	Measured variables	*variable*
w	Exogenous input	*variable*
W_1	Robustness weighting function	-
W_2	Performance weighting function	-
W_{u2}	Weighting function	-
x	Actuator's displacement	m
$\mathbf{x}$	State vector	*variable*
X	Maximum actuator's half-stroke	m
$\mathbf{y}$	Output measurements	*variable*
z	Error signals	*variable*
$\mathbf{z}$	Performance metrics	*variable*

Acronym	Description
b	Boundary set
CAD	Computer Aided Design
CB	Craig-Bampton
CoG	Centre of Gravity
DoF	Degree of Freedom
ESA	European Space Agency
FB	Feedback
FE	Finite Element
FEM	Finite Element Method
FF	Feedforward
FRF	Frequency Response Function
i	Interior set
I/F	Interface
IUT	Item Under Test
LM	Large Mass
MPLAT	Vibration Measurement Platform
MVMS	Micro Vibrations Measurement System
NPL	National Physical Laboratory
PI	Proportional-Integral
SS	State-Space
TAS	Thales Alenia Space
VIBISIO	Vibration Isolation Platform

Acknowledgements

To my family and best friends...
To every dawn and sunset which I have witnessed and to all the unconscious teachers encountered in my life.

In the beginning, I would like to express my sincere gratitude to my supervisor Professor Lorenzo Dozio, the Coordinator of the Study Programmes in Aerospace Engineering, for having given me the opportunity to make experience under the basis of a challenging project of ESA, in collaboration with Thales Alenia Space.

A special thanks goes to my co-supervisor, Dr. Pietro Nali, for his wise advice, brilliant ideas, kind attitude in stimulating to achieve better work, and for having transmitted to me his strong expertise.

I am also grateful to Grzegorz Izworski, the ESA Electromechanical Instrumentation Engineer responsible for this project, for providing me with precise and detailed information on the MVMS facility.

Finally, I would like to thank my colleagues and the stimulating environment of Politecnico di Milano.